UNIVERSITY OF BERGEN

GEOPHYSICAL INSTITUTE

MASTERS THESIS

ELECTRICAL POWER ENGINEERING

Bidirectional DC-DC Converter For Charging Batteries of Electric Vehicles

---

Author: Fredrik Storebø

Supervisor: Vegard Steinsland

May 31, 2021

Abstract

The popularity of electric vehicles has seen significant growth in the latest years. More electric vehicles are connected to the grid, and the load is increased consequently. The electric vehicle battery can be employed as a storage device for the grid by utilizing a bidirectional dc-dc converter. This process, referred to as vehicle-to-grid, requires an implemented control system for controlling the power flow between the battery and grid. By delivering power back in the grid when required, the peak load on the grid can be reduced.

In this thesis the functionality and operation of an isolated bidirectional dc-dc converter for use with battery applications are reviewed, and a simulation model of a dc-dc converter with dual active bridge topology is implemented. Next, a control system with single phase shift modulation is implemented in the simulation model to regulate the power flow between the battery and grid. Finally, the transient response of the battery model utilized in the simulation is compared to a physical battery prototype system, which is constructed and implemented. The adaptable battery design allows for various voltage levels by connecting individual packs in series or parallel, depending on the requirement. The battery system is intended as a proof of concept, which can be developed further.

A conference paper presenting the transient response comparison between the battery prototype designed in this thesis and a supercapacitor is submitted for review for the IEEE ICEC-CME 2021 conference.

Acknowledgment

First, I wish to thank my thesis advisor Vegard Steinsland for his help and guidance with my thesis and for providing helpful feedback and support over this unique period. Secondly, I wish to thank my fellow student Marius Reigstad for close collaboration, helpful motivation, and constructive discussions around the thesis. The collaboration made it possible to achieve an paper for the IEEE ICECCME 2021 conference. This process has been very informative and educational and will benefit me with other projects in the future. Finally, I wish to thank my family for supporting me and allowing me to focus entirely on the project.

F.S.

Contents

List of Figures

List of Tables

Acronyms

Generell

BMS battery management system 26, 38, 39, 41, 43
CCCV constant current - constant voltage 23
DAB dual active bridge 8–10, 12–14, 16, 18, 19, 28–30, 32, 38, 53, 56, 64
DHB dual half bridge 8, 9
DPS dual phase shift 12, 13, 64
EPS extended phase shift 12, 13
EV electric vehicle 6, 10, 22, 29
HEV hybrid electric vehicle 22, 29
HFB half full bridge 8, 9
HV high voltage 10
IBDC isolated bidirectional DC-DC converter 8, 10
Li-ion lithium-ion 22, 23, 26
NaS sodium sulphur 22
NiMH nickel-metal-hydride 22
OCV open circuit voltage 24, 25
PCB printed circuit board 27, 38, 39
PPU power processing units 8
PWM pulse width modulation 12, 43
SiC silicon carbide 30, 31
SOC state of charge 23–26, 33, 34, 36, 47, 49, 51
SOH state of health 26
SPS single phase shift 12, 17, 32, 64
TPS triple phase shift 12, 13, 64
UPS uninterruptible power supply 6, 9
VRF vanadium redox flow 22
ZVS zero voltage switching 10, 16, 17, 56, 65

Symbols

Components

A_e (cm^3) Transformer core volume 21
C_{bat} (F) Charge capacity of the battery 25
C_s (F) Output capacitance of the MOSFET 16
L (H) Inductor 13, 16, 18, 20, 29, 30
L_K (H) Leakage inductor 14, 15
P_v (W/cm^3) Transformer core loss per unit of volume 21
Q_G (F) Total gate charge of the MOSFET 31
$R_{AC,ind}$ (Ω) AC winding resistance in the inductor 21
R_{AC_1} (Ω) AC winding resistance in the primary coil 21
R_{AC_2} (Ω) AC winding resistance in the secondary coil 21
$R_{DC,ind}$ (Ω) DC winding resistance in the inductor 21
R_{DC_1} (Ω) DC winding resistance in the primary coil 21
R_{DC_2} (Ω) DC winding resistance in the secondary coil 21
R_{max} (Ω) Maximum DC resistance in individual strands 21
R_{on} (Ω) On resistance of the MOSFET 20, 31

Electrical

E_C (J) Energy stored in capacitor 16
E_L (J) Energy stored in inductor 16
i_2 (A) DC current out of the converter 25, 30
I_{ac1} (A) Primary AC current 21
I_{ac2} (A) Secondary AC current 21, 30
i_{C2} (A) Capacitor current 30
I_ϕ (A) Instantaneous value of il 20
I_{dio} (A) Diode rms current 20
I_D (A) Drain current in MOSFET 31
I_1 (A) Instantaneous value of il 20
i_L (A) Inductor current 13–18, 53
I_{mos} (A) MOSFET rms current 20

I_0 (A) Instantaneous value of i_L 20
I_{sw} (A) Current at switching time 19, 56
P_{ac} (W) Skin effect loss 21
P_{cond} (W) Conduction loss 20
P_{copper} (W) Copper loss 21
P_{core} (W) Core loss in a transformer 21
P_{ind} (W) Inductor loss 21
P_{out} (W) Power out from converter 13, 30
P_{sw} (W) Switching loss 19
V_1 (V) DC voltage in to the connnverter 13, 15, 20, 30
V_2 (V) DC voltage out of the converter 13, 15, 20, 30
V_{ac_1} (V) AC voltage on the primary side 13–15, 17, 18, 53
V_{ac_2} (V) AC voltage on the secondary side 13–15, 17, 18, 53
V_{DS} (V) Voltage over MOSFET 16, 31, 56
V_{fd} (V) Forward voltage drop over diode 20
V_L (V) Inductor voltage 13–15, 17, 18, 53
V_{sw} (V) Voltage at switching time 19

General

f_{sw} (Hz) Switching frequency 13, 15, 19, 21, 30
ω ($\frac{\text{rad}}{\text{s}}$) Angular frequency 18, 20
n (−) Ratio between secondary and primary 13–15, 30
G_S (−) Gate signal to the MOSFET 56
H (−) Ratio of individual strands 21
N (−) Number of strands 21
N_s (−) Number of parallel conductors 21
D_i (mm) Diameter of individual strands 21
D_o (mm) Diameter of cable 21
N (−) Voltage ratio between primary and secondary 17, 18
ϕ (rad) Phase Shift 12, 13, 15, 20, 30
t_{off} (s) Time interval during OFF switching 19
t_{on} (s) Time interval during ON switching 19

1 Introduction

1.1 Background

In 2020 the market share of new battery electric vehicles in Norway surpassed 50 percent for the first time[1]. This market share is a substantial increase from 42 percent in 2019[1]. While more electric cars rapidly come available, the load on the power grid consequently increases as more cars connect to the grid. Most electric car chargers sold today are unidirectional, as they only deliver power from the grid to the car. With the introduction of a bidirectional charger, the power can flow both between the car and the grid. By using the car as a storage element, the maximum load on the system can be reduced.

Other typical applications for bidirectional dc-dc converter include regenerative power systems and uninterruptible power supplies. Renewable power generation such as wind and solar, are dependent on a fast and stable dc link. A battery and supercapacitor are often combined to achieve this characteristic.

Figure 1.1 shows a simple concept and power flow of the bidirectional dc-to-dc converter. The secondary side dc voltage can be increased/decreased depending on both the configuration and control method of the converter. The main benefit of a bidirectional converter is the ability to transfer power in both directions between the primary and secondary sides. As will be discussed later in this thesis, there are many different topologies and strategies to achieve this power transfer.

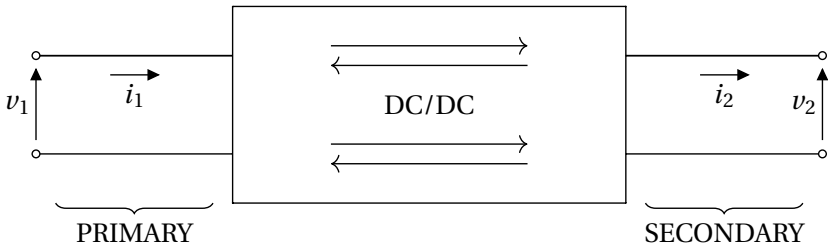

Figure 1.1: Simplified concept model of a bidirectional dc-dc converter

1.2 Literature Review

For many power-related systems, the bidirectional dc-dc converter has become a compelling option, as improvements to the system in addition to improved performance are often possible. Energy storage devices such as batteries rely on a converter for transmitting the power flow efficiently. A study examining a bidirectional dc-dc converter for an energy storage system with galvanic isolation is presented in [2]. A 200 V 2.6 kJ laboratory model is applied to verify the design and reveal limitations on the dc voltage range. Similarly in [3], a new zero voltage switching bidirectional dc-dc converter for fuel cell and battery application is proposed. By improving the zero voltage switching strategy, the losses will be lower, thus increasing the efficiency. A purely simulated model is presented in [4], where a simulation of dual active bridge converter for energy storage system is designed.

The power conversion aspect of the bidirectional dc-dc converter is an essential element. In [5], an overview of a dual active bridge isolated bidirectional dc-dc converter for high frequency link power conversion system, is presented. This study utilizes a high-frequency transformer for achieving a compact and low-cost alternative. Included in the overview is a comparison between different control strategies and soft switching possibilities. These strategies will influence the power conversion, depending on the complexity and efficiency of the strategy. A bidirectional isolated dc-dc converter as a core circuit of the next generation medium voltage power conversion system is presented in [6]. This paper introduces silicon carbide for power switching devices. These devices are a developing technology with high potential. Adopting the microgrid is the focus in [7], where extended phase shift control of isolated bidirectional dc-dc converter for power distribution in microgrid is presented. Likewise in [8], modeling and control of a dual active bridge for energy storage in dc microgrid applications are presented. This paper presents design for filters for both the input and output to contain the current ripple to the energy storage.

The bidirectional dc-dc converter performances will vary depending on the control and switching strategy. The short-time-scale transient response in a bidirectional dc-dc converter utilizing single phase shift modulation is presented in [9]. This study shows the relation between phase shift and power and the mitigation of phase shift error through control. A phase shift control of mitigating the circulating current and achieving zero voltage switching is presented in [10]. The paper introduces dual phase shift modulation to improve the performance of the single phase shift. Similarly, triple phase shift modulation is presented in [11]. The study achieves full zero voltage switching for a broad range with a description of the control strategy applied. A comparison between the different phase shift modulations is presented in [5]. The theoretical overview showcases the difference in control strategy, characterization, and optimizations for the various modulations.

Loss calculations are an essential factor in the design process of a bidirectional dc-dc converter. An analysis of the power flow between the input and output is presented in [12]. The proposed calculations are beneficial for the preliminary evaluation of power losses. The calculations are based on average currents and will thereby be approximate. Estimated losses are also provided in [13]. This estimation is achieved by simplifying the model. A similar process is performed in [14], where an estimation of the switching and core losses is presented. Most of the papers studying the power flow and losses in the bidirectional converters only study a specific part of the converter. When a transformer is introduced to the topology, the reactive power may become a problem. This dilemma is studied in [15], where a design is proposed to eliminate reactive power and increase the converter's efficiency.

The battery characterization is an fundamental factor to consider when designing a control system. Different battery types and chemistries display various charging and discharging requirements and characteristics. The handbook of batteries, third edition[16] presents principle of operation in addition to showcasing information and characterization about numerous battery varieties. In addition, the handbook presents battery performance requirements for electric vehicle applications. The technological developments in batteries are constantly improving, which is the focus of the study in [17]. The paper presents battery developments with real-world applications and compares the performance of the different battery types. Lithium-ion batteries are commonly utilized for electric vehicle applications. A novel adaptive technique for estimation the li-ion model parameters are presented in [18]. The study utilizes the calculated parameters for state-of-charge estimation and presents the equivalent circuit elements.

1.3 Objective

This thesis aims to design a simulation model of a isolated bidirectional dc-dc converter, implement a control system for regulating the power flow, and compare the transient response of the simulated battery model with a physical battery system.

- Implement an isolated bidirectional dc-dc converter simulation model in Matlab® /Simulink®for use with electric vehicle applications.
- Implement a control system for regulating the bidirectional power flow between the input and output of the bidirectional converter simulation.
- Design a battery prototype system, implement an external balancing system as a proof of concept, and compare the battery prototype's transient current and voltage responses with the simulated battery model.

1.4 Thesis Structure

This thesis is structured into six chapters, introduction, theory, method, results, discussion and conclusion. Chapter 2, **Theory**, is built to provide information and explain the relevant theory of the thesis. First different bidirectional dc-dc converter topologies are present and analyzed, and the dual active bridge topology is presented as the primary converter topology. The operation of the converter is presented with modulation and significant characteristics of the topology. Next, the typical battery types are presented, with a focus on the lithium-ion battery. The characteristic and charging method is presented with an explanation of the state-of-charge and battery management system. Lastly, the software tools applied in this thesis are displayed. Chapter 3, **Method**, is written to explain the simulation model implementation and the design process of the physical models. Firstly the parameter selection is presented with justification for each selection. Then the simulation models of both the dc-dc converter and simplified battery are presented and explained. Next, the battery prototype pack is introduced, and the protection systems to prevent damage to the pack. Finally, the test setup for testing the prototype battery pack is presented. Chapter 4, **Results**, showcases the results from the operation of the converter simulation and battery pack. The bidirectional dc-dc converter simulation results include charging and discharging responses, power flow between the bridges, and the soft switching capabilities of the converter. The physical battery test compares the transient response of the prototype with the simulated battery in Simulink. Chapter 5, **Discussion**, discusses the simulation models and the test results. Chapter 6, **Conclusion**, contains the main aspect of the paper, and summarizes findings. **Appendix**, includes supporting documentation of relevant records. appendix A showcases the submitted conference paper for the IEEE ICECCME 2021 conference.appendix B display the approved abstract for the IEEE SEST 2021 conference. appendix C presents the simulated converter model and source code. appendix D displays the simulated battery model. appendix E show the full design of the laboratory prototype with PCB schematic and copper layouts. appendix F presents the test setup components.

2 Theory

This chapter is divided in four sections; Topology, Operation, Battery and Software tools. In 2.1 Topology, different bidirectional topologies are presented and compared. In 2.2 Operation, the function and operational characteristic of the dual active bridge is explained. In 2.3 Battery, different battery types are presented and the lithium-ion characteristic is presented. In 2.4 Software tools, the version and types of software used in this thesis is presented.

2.1 Topology

Today most electric vehicle battery chargers are designed with unidirectional powerflow [19]. While unidirectional chargers has simpler topologies, bidirectional chargers offer greater benefits with power flow in both directions. This opens up possibilities of vehicle-to-grid, where the battery can deliver energy to the grid. Bidirectional converters can be separated into two different groups, non-isolated and isolated topologies. These groups are described below and examples of common topologies are provided.

2.1.1 Non-Isolated Bidirectional DC-DC Converters

Converters without galvanic protection are presented as non isolated converters. Without the need of magnetic isolation, they have a simple topology and small physical size. In addition they don't have to take magnetic interference into consideration. These bidirectional topologies differ from the unidirectional topologies by an additional controllable switch to their diode. Often a antiparallel diode is attached to the main switch [20].

Some of the more common non isolated bidirectional converters are "buck and boost", "buck-boost" and "cuk". Other topologies are focused on boosting the voltage, such as "cascaded", "interleaved" and "switched capacitor" topologies. The "buck and boost" topology presented in fig. 2.1a performs as an buck converter from input to output and as an buck in the opposite direction. It has a low number of components, with only two controllable switches and a single inductor. However a disadvantage with this topology is its lack of input current continuity. This type of converter has previously been used for photovoltaic systems[21] and

for uninterruptible power supply (UPS) [22]. The ratio between the input and output voltage is given as $1/(1-D)$ where D is the duty cycle. The "buck-boost" topology illustrated in fig. 2.1b have a higher degree of flexibility than the buck and boost with its power transfer. This is due to its ability to boost or buck the voltage in both directions. The output voltage of this topology will be reversed, with a negative output for a positive input. The voltage ratio will then be $-D/(1-D)$. Photovoltaic System[23].

The "cuk" topology shown in fig. 2.1c has the advantage in continuity of both the input current and output current. This is due to its increased component count, with a dual inductor setup. The series capacitor between the inductors acts as a energy storage, by storing the energy from the input before it is transferred to the output. The voltage can then be increased or decreased depending on the duty cycle. In addition the inductors decreases the current ripple of the converter [20]. Similarly to the buck-boost topology, the output voltage polarity is reversed, and the voltage ration can be set as $-D/(1-D)$. A bidirectional "cuk" converter is designed in [24] for the use in a electric vehicle (EV). Other common applications are with energy storage as demonstrated in [25]. The "cascaded", "switched" and "interleaved" topologies are based on the concept of voltage boosting. The cascaded topology presented in fig. 2.1e consists of two bidirectional buck-boost converters connected in a cascaded formation. By cascading two converters, the voltage can be further increased to a higher level. In addition the current stress and ripples are reduced, this enables the converter to operate with a higher power rating. However with the increased number of controllable switches, the switching losses of the converter will subsequent increased. The voltage ration of this topology is similar to the basic buck and boost topology with $1/(1-D)$.

A "interleaved" formation is shown in fig. 2.1f. Here two inductors located between the controllable switches are connected together. This type of topology is often used to increase efficiency and filter reduction. As the frequency current ripple are reduced due to the interleaving, the filter can be decreased to a smaller size. There are several uses for this type of converters including automotive and high power applications. [26]. The "switched capacitor" topology illustrated in fig. 2.1d does not require a inductor to operate. This provides the advantage of a lower component count and reduced weight. This technique is often used to increase the converters voltage boosting ability [20]. Of all the non isolated bidirectional converters listed, there are two different topologies that are equipped for EV. Buck-boost and the cascaded topologies both have qualities that fits this purpose [27].

Table 2.1: Comparison between non-isolated bidirectional converter topologies

Topology	**Notes**	**Ratio**
Buck and Boost	+ Low component count – Current discontinuity	$1/(1-D)$
Buck-Boost	+ Flexibility – Reversed voltage	$-D/(1-D)$
Cuk	+ Current continuity + Low ripple	$-D/(1-D)$
Switched	+ No inductor – Boosting ability	2
Cascaded	+ High power rating – Higher losses	$1/(1-D)$
interleaved	+ High efficiency – Small filter	$1/(1-D)$

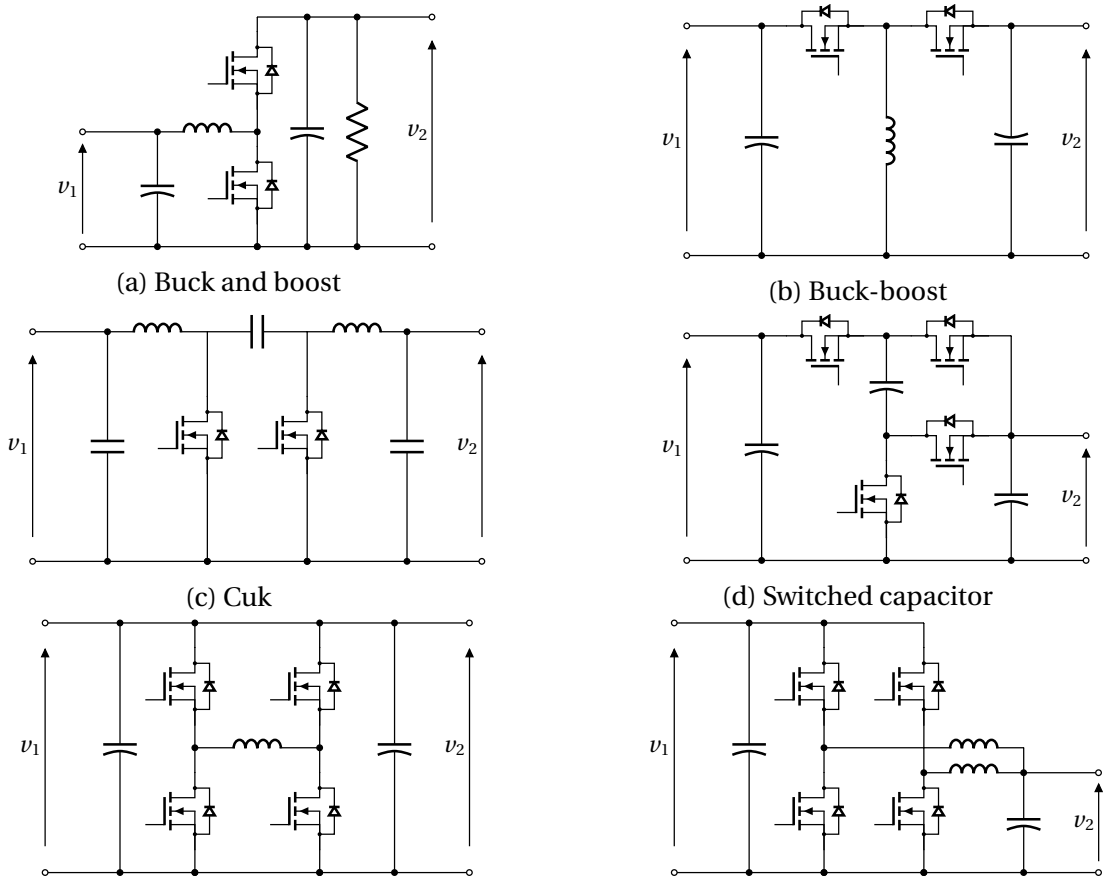

(a) Buck and boost

(b) Buck-boost

(c) Cuk

(d) Switched capacitor

(e) Cascaded

(f) Interleaved

Figure 2.1: Non-isolated bidirectional dc-dc converter topologies

2.1.2 Isolated Bidirectional DC-DC Converters

Isolated bidirectional converters adds a level of security in the system, with a physical separation of the primary and secondary side. The gap between input and output is created through magnetic isolation in the transformer. This creates additionally complexity to the system and an increased component count. The main principle of an isolated bidirectional DC-DC converter (IBDC) is the transformation from dc to ac then back to dc. The isolated topologies can be split into two subcategories, basic and full/half bridge converters. Common basic isolated systems include flyback, cuk and push-pull. While for the full/half bridge some of the main topologies are the dual active bridge (DAB), dual half bridge (DHB) and half full bridge (HFB). The flyback topology shown in fig. 2.2a, is often adopted due to its simplicity. It is based on a non-isolated buck-boost topology, where the inductor is substituted for a transformer. However one of the main challenges with this topology is the discontinuity of the input current. The voltage ratio will is comparable with the non-isolated topologies, but with a added N-component due to the voltage transformation. For this flyback topology, the ratio will be $ND/(1-D)$. It is primarily used in low power applications, such as cell phones, TVs and personal computers [28].

The isolated cuk topology in fig. 2.2b has the advantages of continuous input and output current. In addition the coupling of the different inductors, reduces the current ripples in the converter. The topology is similar to the non-isolated cuk, where a transformer is inserted between the controllable switches. Compared to the flyback, the topology has an increased component count, but will be able to achieve higher efficiency. The voltage ratio will however be the same, $ND/(1-D)$. One of the main application for this topology is high efficiency power processing units (PPU) [29]. A push-pull topology is displayed in fig. 2.2c, this also has the ability of continuous output current. Contrary to the other isolated bidirectional converters mentioned, this topology utilizes a multi-winding transformer. In addition the number of switches is increased from two to four, to achieve the desired functionality. The voltage ration can therefore be simplified to ND. A converter based on this design is presented in [30], for automotive applications.

When higher level of power is required, half/full bridge topologies are often desired. The voltage ration of the these converters are heavily dependent on the selected control scheme, and can therefore not be generalized. One of the more popular isolated bidirectional converters is the DAB topology in fig. 2.2d [20]. This popularity is partly due to its high efficiency and power density coupled with its buck/boost capability. Its therefore often used in bidirectional chargers for electrical vehicles [31]. The DHB displayed in fig. 2.2e is similar to the DAB, but with less controllability. In each bridge two of the switches are replaced with capacitors, this reduces the switches from eight to four. This makes it more ideal for the use

with lower power applications, as the switching losses will be reduced [32]. The HFB topology shown in fig. 2.2f, is a combination of the DAB and the DHB converters. Two of the controllable switches are replaced by capacitors only on the primary bridge. This allows for simpler control requirements while still having the ability for buck-boost conversion. It is therefore often used with UPS systems [20].

Table 2.2: Comparison between isolated bidirectional converter topologies

Topology	**Notes**	**Ratio**
Flyback	+ Basic – Current discontinuity	$ND/(1-D)$
Cuk	+ current continuity + Low ripple	$ND/(1-D)$
Push-pull	+ Current continuity – High component count	ND
DAB	+ High power rating – Current discontinuity	Depending on control
DHB	+ High power rating – Higher losses	Depending on control
HFB	+ High efficiency – Current discontinuity	Depending on control

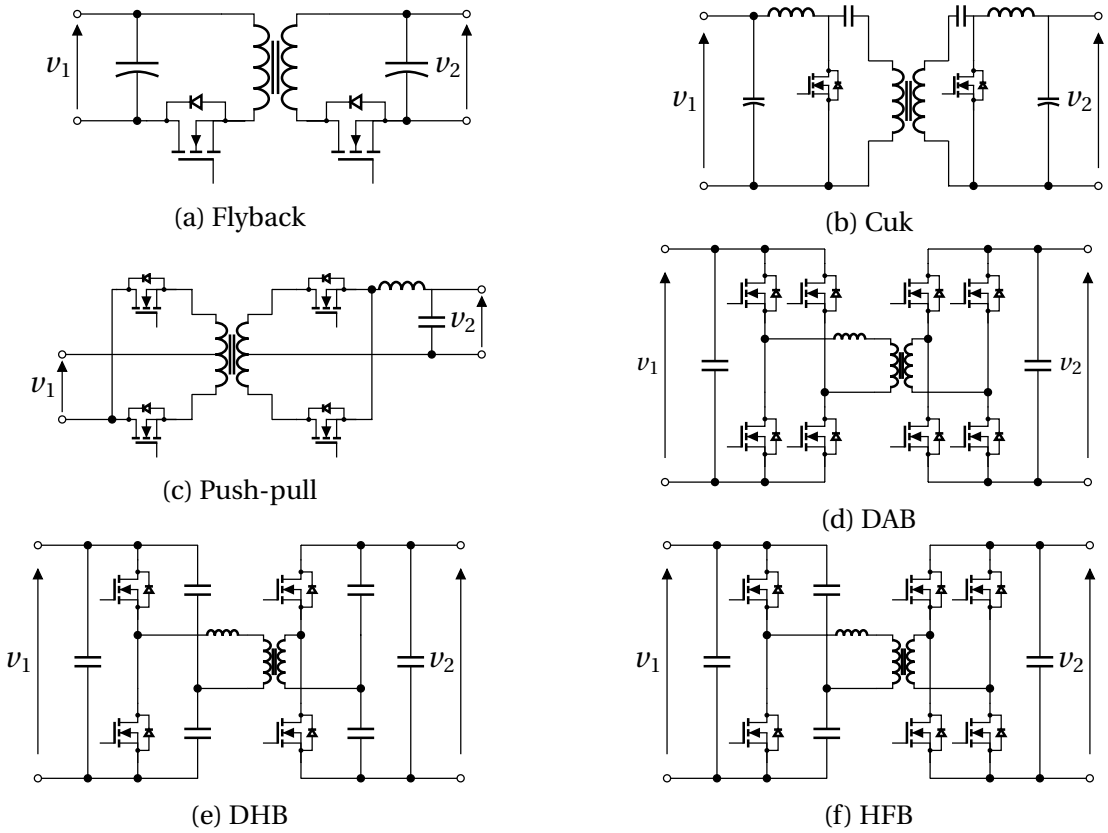

Figure 2.2: Isolated bidirectional dc-dc converter topologies

2.1.3 Dual Active Bridge

First proposed by Doncker et al. in 1988 [33], the DAB is today one of the most popular IBDC topologies [20]. It has a seamless bidirectional flow, coupled with a wide voltage range. In addition the DAB has the ability to achieve zero voltage switching (ZVS), significantly decreasing the switching loss. This makes it an excellent choice for controlling both charging and discharging of a battery in an EV.

Figure 2.3 showcase the topology of the DAB converter. The symmetrical layout of the converter, makes it uncomplicated to achieve bidirectional power flow. The DAB is as the name suggest separated into two active bridges, the high voltage bridge and the low voltage bridge. Each bridge is constructed by four controllable semiconductor switches. Separating the two bridges are a high frequency transformer with galvanic isolation. An energy transfer inductor can be placed on either side of the transformer, but are often placed on the high voltage (HV) side due to the lower current value. Capacitors are placed at both the input and output to decrease the current and voltage ripples.

The high frequency transformer allows for an reduction in both the size and weight of the converter. Due to the high frequency, the magnetizing inductance can be neglected [34]. Therefore a simplified model is often used, for power calculations. This is explained in more

detail later in section 2.2.5 (loss analysis). MOSFET devices are often used for the controllable switches, this is because of their drain-to-source output capacitance and intrinsic body diode [34]. IGBT may also be used, but with the need of extra components as capacitors. In bidirectional converters he number of controllable switches is proportional with the power transmission [35]. Since the DAB is utilizing eight switches it is capable of transmitting large amounts of power, and is therefore able to be used in high power applications.

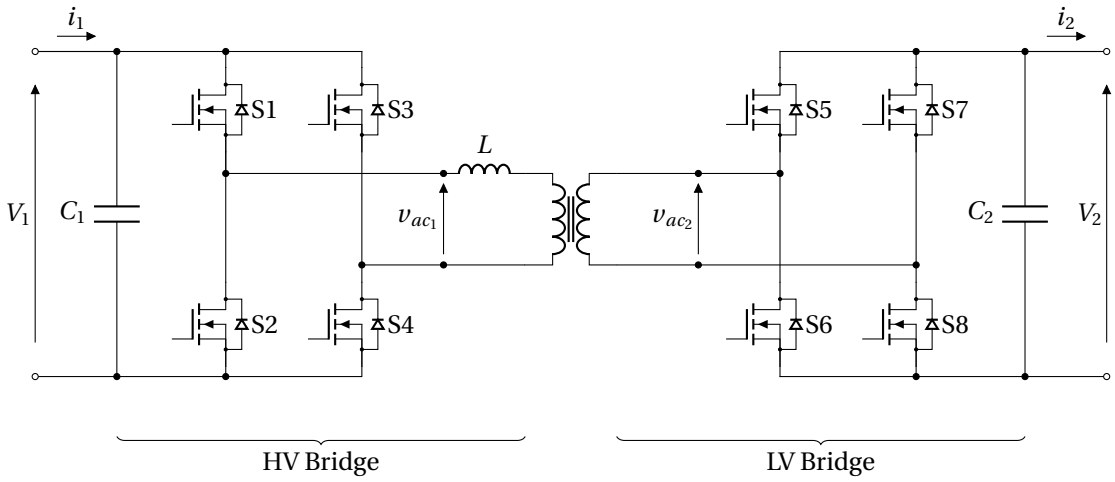

Figure 2.3: Isolated bidirectional dc-dc converter with a dual active bridge topology.

2.2 Operation

Each bridge in the DAB produces a specific wave voltage, with their semiconductor switches. These waves can be modulated to achieve the desired power flow between the bridges. During operation of the DAB there are two modes available, boost and buck. Boost mode is defined as power flow from the low voltage side to the high voltage side. Accordingly buck mode occurs during power flow in the opposite direction, where there is power flow from high to the low voltage side.

2.2.1 Phase Shift Modulation

Both pulse width modulation (PWM) and phase shift modulation are frequently used as switching strategies for the DAB converter. Each bridge produces a specific wave, which is modulated differently based on the selected switching strategy. One of the simplest and most common phase shift strategies is the single phase shift (SPS) modulation [2], [9], [36], [37].With this technique each bridge produces a square voltage wave which are half a period out of phase with each other. These waves are set with a constant duty cycle of 50 %.

The power flow is controlled by phase-shifting the square wave voltages of either bridge in front or behind the other bridge. This SPS modulation is implemented by delaying the gate signals for the controllable switches of the desire bridge. By phase-shifting the pulses, the power flow from one bridge to the other can be controlled. The power will therefore flow from the lagging to the leading bridge. The only variable that needs to be controlled to change the power flow is consequently the phase shift (ϕ). The phase shift is ordinarily displayed as radians while calculating but may be presented as seconds or percent for more natural visualization. It is valid between -π and π rad. The maximum amount of power will however be transferred while the phase shift is $\pi/2$, or 50% of the max allowable value in the positive perspective. As only the delay between the bridges are controlled, soft switching of the controllable switches experience reduced range of motion. Another issue with SPS is the circulating current generated in the circuit, this is more closely explained in section 2.2.4 (soft switching).

Other phase shift modulation have been researched to improve the range of soft switching, in addition to minimizing the circulating current. Dual phase shift (DPS), extended phase shift (EPS) and triple phase shift (TPS) modulation all have a benefit towards SPS, but have increased levels of complexity. EPS [7], [38]–[40] introduces a inner phase shift in the primary bridge in addition to the outer phase shift. The duty cycle of the primary voltage wave can then be controlled. This creates a three level output ac wave on the primary bridge, instead of the square voltage wave of SPS. With this methodology soft switching range is increased.

In DPS [15], [41]–[43] the inner phase shift is added to both bridges, but the values are kept identical to each other. The duty cycle of the square waves can then be controlled on both bridges. In addition, DPS can be implement simpler then EPS, due to the symmetry of the model and voltage waves. Furthermore the dynamic performance can be substantially higher. TPS [11], [44]–[46] increases the controllability with three degrees of freedom. Both bridges inner phase can then be controlled individually. This methodology has the highest advantages relevant to efficiency soft switching operating range. However, due to its complexity it is rarely used and there exist no unified standard for implementation [5].

2.2.2 Power Flow

As stated earlier, the DAB converter has bidirectional properties. It can therefore transfer power in and out of the converter. Depending on the power flow direction, the converter has two states, buck and boost [47]. When transferring power from the primary bridge to the secondary bridge, the converter is in buck mode. Where it is supplying power from a high voltage level to a lower voltage level. This mode of operation has positive power flow, where the primary leads the secondary voltage wave. This operation is shown in fig 2.4a, where V_{ac_1} and V_{ac_2} are the primary and secondary square voltage waves. In addition the voltage and current over the inductor V_L, i_L is displayed. Where the voltage over the inductor experiences voltage spikes where a wave has a different polarity to the other.

contrary to the buck mode, the converter will be in boost mode when transferring power from the secondary to the primary. Here the current goes from a low to a high potential, and the power flow will be negative with respect to the primary. The secondary square wave voltage will then be leading the primary wave, as shown in fig. 2.4b. This operation inverts the voltage and current signals for the inductor, which is visualized by comparing the figures.

In the nominal area of the battery characteristic, the battery voltage is kept close to constant with a slight deviation. The output power equation can then be simplified and calculated from eq.(2.1), P_{out} is the output power, n is the primary to secondary ratio, L is the inductor, f_{sw} is the switching frequency, and ϕ is the phase shift. The primary and secondary voltage is represented as V_1 and V_2 respectively. The calculated output power will be a product of the battery voltage and output current from the converter.

$$P_{out} = \frac{nV_1V_2}{2Lf_{sw}}\phi(1-\phi) \tag{2.1}$$

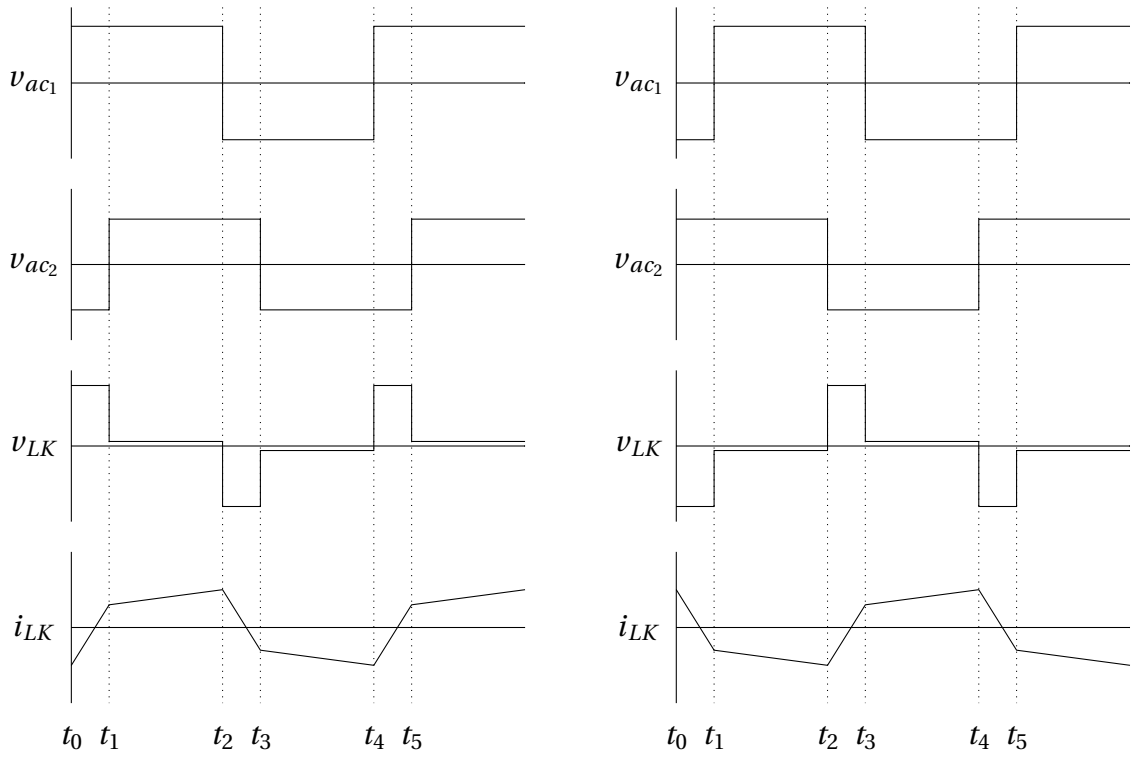

(a) Buck mode (b) Boost mode

Figure 2.4: Operating waveform of the primary(v_{ac_1}) and secondary(v_{ac_2}) ac voltages aligned with the leakage inductor voltage(v_{LK}) and current(i_{LK}) waveform.

2.2.3 Inductor Characteristic

One of the more important elements of the DAB is the leakage inductance, as it directly connects to the power transfer capabilities previously shown in eq. (2.1). The voltage and current value characteristics are consequently crucial aspects of the projects. When calculating the inductor current, the equivalent circuit in fig. 2.5 is commonly used [34], [48], [49].

The circuit consists of two square voltage sources on either side of an inductor. The primary voltage is set as V_{ac_1}, while the secondary voltage is set as n times V_{ac_2}. The current through the leakage inductor is calculated by integrating the voltage over the inductor, as shown in eq. (2.2). Where $i_L(t_0)$ is the initial current, L_K is the inductor and V_L is the voltage over the inductor.

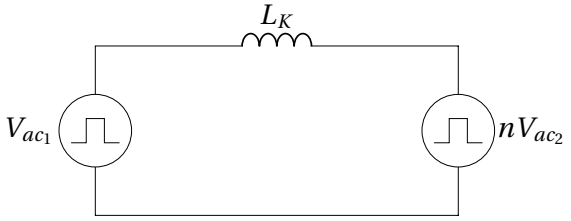

Figure 2.5: Simplified equivalent circuit diagram of the dual active bridge.

$$i_L(t) = i_L(t_0) + \frac{1}{L_K}\int_{t_0}^{t1} V_L dt \tag{2.2}$$

The current can be split up in different time intervals, as illustrated above in fig. 2.4. As the voltage level surge, the current increases in the same direction as the voltage spike. The voltage and current values of the inductor will be mirrored depending on the power flow direction. The different currents are then derived as eq.(2.3), (2.4), (2.5), and (2.6). These equations represent the current in each time interval [48].

$$i_L(t_{0-1}) = i_L(t_0) + \frac{V_{ac_1} + n \cdot V_{ac_2}}{L_K}(t - t_0) \tag{2.3}$$

$$i_L(t_{1-2}) = i_L(t_1) + \frac{V_{ac_1} - n \cdot V_{ac_2}}{L_K}(t - t_1) \tag{2.4}$$

$$i_L(t_{2-3}) = i_L(t_2) - \frac{V_{ac_1} + n \cdot V_{ac_2}}{L_K}(t - t_2) \tag{2.5}$$

$$i_L(t_{3-4}) = i_L(t_3) - \frac{V_{ac_1} - n \cdot V_{ac_2}}{L_K}(t - t_3) \tag{2.6}$$

Due to the characteristic's symmetry, the current at t_0 will be equal to the negative value at time t_2, $i_L(t_0)$ and -$i_L(t_2)$. Similarly, the current at t_1, and the negative current value at t_2 will be the same, $i_L(t_1)$ and -$i_L(t_3)$. This is consistent for every period, the values at t_4 can then be replaced by the same values at t_0. Time t_1 is determined by the amount of phase shift applied. Therefore, t_1 can be represented by eq. (2.7), where the time is a product of the phase shift and the switching frequency. Time t_2 occurs exactly when the first square voltage wave ends. Since every pulse is set at 50%, the time will be half a period and can thereby be calculated by eq. (2.8). By combining eq. (2.7), (2.8) with the above equations, they can be simplified down to eq. (2.9). Where the current is an element of the phase shift and the switching frequency.

$$t_1 = \frac{\phi}{2\pi f_{sw}} \tag{2.7}$$

$$t_2 = \frac{1}{2f_{sw}} \tag{2.8}$$

$$i_L(t_0) = \frac{(nV_2 - V_1)\pi - nV_2 \cdot 2\phi}{4\pi L_K f_{sw}} \tag{2.9}$$

2.2.4 Soft Switching

One of the DAB converter's main advantages is its capability to achieve ZVS, which is defined as switching from one state to another while the voltage potential over the switch is zero. In the DAB, this is possible due to the intrinsic diode and the output capacitance of the MOSFET. While switching from on- to off-state, the current will flow through the switch keeping the voltage to zero. Since the switch off is not instant, there will be a slight overlap with current and voltage. While not achieving ZVS, it can be classified as pseudo-ZVS due to it almost achieving complete soft switching. During the opposite operation from off- to on-state, complete ZVS can be achieved.

Figure 2.6 displays the different steps to achieve soft switching during the dead time between t_1 and t_2. From step 1, switches S6/S7 experience pseudo-ZVS while turning off. In step 2, all the switches enter the off-state and the output capacitance of S6/S7 charges up from 0. Simultaneously the capacitance of S5/S8 discharges. When all the capacitors are charged/discharged in step 3, the currents pass through the intrinsic diodes of S5/S8. While the current runs through the diodes, the voltage over the switches is zero, and the switches turn on. The DAB's soft-switching ability depends on the energy stored in the primary side inductor, displayed in eq. (2.10), the output capacitance of the MOSFETs shown in eq. (2.11). The amount of energy in the inductor must be able to fully charge/discharge both output capacitors. The minimum inductor current required to achieve soft switching can therefore be calculated in eq. (2.12) by combining eq. (2.10) and eq. (2.11).

$$E_L = \frac{1}{2} L {i_L}^2 \tag{2.10}$$

$$E_C = \frac{1}{2} C_s {V_{DS}}^2 \tag{2.11}$$

$$i_{L,min} = \sqrt{\frac{2C_s {V_{DS}}^2}{L}} \tag{2.12}$$

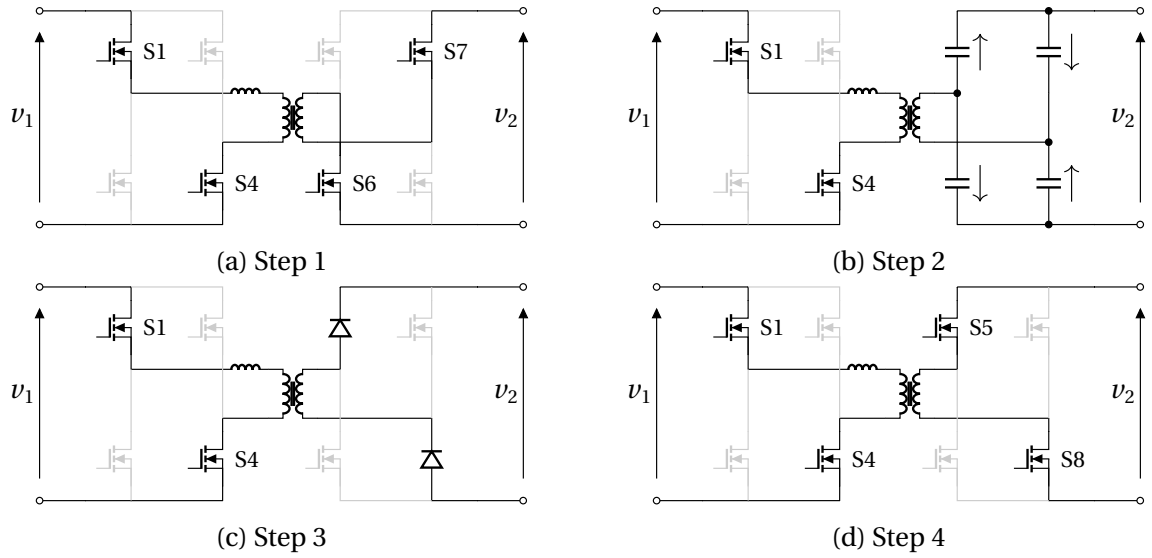

Figure 2.6: Dual active bridge equivalent topologies between time period t_1 and t_2.

Maintaining soft-switching might not possible during light loads, as there is not enough load current to charge the capacitors. For increasing the ZVS-range of the converter, several methods have been suggested [10],[50],[51]. The majority of these methods are modifying the switching strategy, allowing for a broader range of soft switching.

As mentioned earlier, circulating current is a known issue with SPS modulation. When the inductor current i_L leads in either direction, it also transmits some power in the opposite direction. This backward current counteracts some of the positive currents, which in total equals zero. This aspect is called the circulating current and does not transfer any energy. For power to be transmitted, the positive current has to be greater than the reverse current. Figure 2.4 displays this phenomenon earlier in the thesis.

Circulating current can be compared to the reactive current in an ac grid, as it is a pure energy loss [50]. The transformer and conduction losses will therefore increase with a higher quantity of circulating current. The voltage gain between the primary side and the secondary side N, is correlated to the amount of circulating current. The phasor diagram in fig. 2.7 indicated this characteristic. $\overrightarrow{V_{ac_1}}, \overrightarrow{V_{ac_2}}, \overrightarrow{V_L}$ and $\overrightarrow{i_L}$ are the phasors for the relevant voltages and currents in the model. For calculating the fundamental components and their angles, eq. (2.13) and eq. (2.14) are used respectively [50].

$$Components \begin{cases} \overrightarrow{V_L} = \overrightarrow{V_{ac_1}} - \overrightarrow{V_{ac_2}} \\ \overrightarrow{i_L} = \dfrac{\overrightarrow{V_L}}{j\omega L} \end{cases} \tag{2.13}$$

$$Angles \begin{cases} \gamma + \beta = \pi - \alpha \\ \dfrac{sin(\gamma)}{sin(\beta)} = \dfrac{|\overrightarrow{V_{ac_2}}|}{|\overrightarrow{V_{ac_1}}|} = N \\ \theta = \dfrac{\pi}{2} - \gamma \end{cases} \tag{2.14}$$

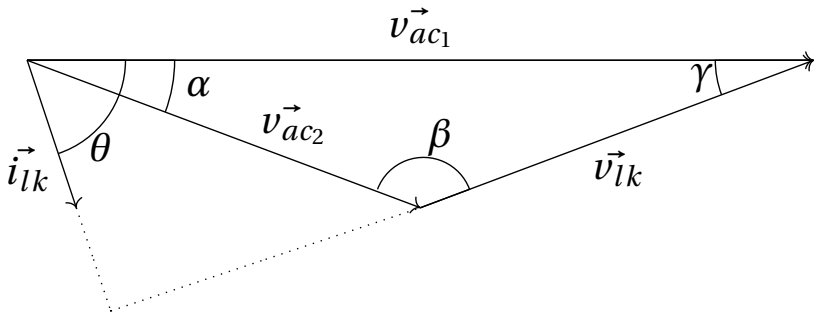

Figure 2.7: Phasor diagram for the ac voltages and the leakage inductor voltage and current.

The phasor diagram exhibits the relationship between the voltage gain N and the portion of reactive power. As N decreases below 0 with a given α, γ will decline while θ increases. As θ is the angle between $\overrightarrow{v_{ac_1}}$ and $\overrightarrow{l_{lk}}$, it, therefore, leads to an increase in reactive power. There have been proposed numerous methods to lower the circulating current, thereby improving the DAB efficiency. Papers [52] and [53] proposes hardware methods where diodes replace some of the secondary bridge power switches. However, these methods do limit the bidirectional capabilities of the converter. Methods of improving the converter's switching strategy are more conventional [54]–[57].

2.2.5 Loss analysis

When considering losses in the dab, three categories are applied: switching, conduction, and magnetic losses. The switching losses occur while the controllable semiconductor switches are turning from one state to another. The conduction losses are the continuous losses while conducting during nominal operation. Finally, the magnetic losses include the transformer as well as the losses in the inductor. Each of the loss calculations is show below, divided into different groups.

Switching loss

As explained above, the switching loss occurs in each semiconductor while it changes state. The magnitude of the DAB's switching losses is heavily dependent on whether soft switching can be achieved or not. The switching loss in eq. (2.15), displays the loss per controllable semiconductor switch, this equation includes the losses from both the on- and off-switching. The total switching loss will thereby be a product of the eight controllable semiconductor switches. The switching loss in eq. (2.16), presents the total loss over both the primary and secondary bridge. The switching times can be assumed to be equal for both the primary and secondary bridge, eq. (2.16) can then simplify to eq. (2.17). The values are instantaneous at the time of switching for each equation. These calculations are furthermore thoroughly described in [13], [14], [35].

$$P_{sw} = \frac{1}{2} V_{sw} I_{sw} (t_{on} + t_{off}) f_{sw} \tag{2.15}$$

$$P_{sw} = 2(V_{sw,p} I_{sw,p})(t_{on,p} + t_{off,p}) f_{sw} + 2(V_{sw,s} I_{sw,s})(t_{on,s} + t_{off,s}) f_{sw} \tag{2.16}$$

$$P_{sw} = 2(V_{sw,p} I_{sw,p} + V_{sw,s} I_{sw,s})(t_{on} + t_{off}) f_{sw} \tag{2.17}$$

P_{sw} represents the switching loss in the equations above, first as the loss per semiconductor in eq. (2.15) then as the total loss in eq. (2.16) and eq. (2.17). V_{sw} and I_{sw} are the instantaneous voltage and current values at the time of the switching operation. Similarly, t_{on} and t_{off} are the periods during which the current and voltage switch from one state to another. The lowercase p and s in the equations are applied to distinguish the primary and secondary bridge values.

Conduction loss

The conduction losses apply to the continuous losses during regular operation. The losses, therefore, include both losses in the resistance of the semiconductor R_{on} and the voltage drop over the antiparallel diode V_{fd}. These calculations are derived in [13]. Equation (2.18) calculates the instantaneous value of the inductor current (I_0) when the primary voltage wave switches polarity from negative to positive. Similarily eq. (2.19) calculates the instantaneous value of the inductor current (I_ϕ) when the secondary voltage wave turns from negative to positive. These currents are applied to find the rms value, as shown in eq. (2.21) and eq. (2.20). The diode will be conducting during the t_1 period, while the semiconductor will conduct at between t_2, t_3, and t_4. The duration of these periods is dependent on the phase shift.

$$I_0 = -\frac{(V_1 + V_2)\phi + (V_1 - V_2)(\pi - \phi)}{2\omega L} \tag{2.18}$$

$$I_\phi = \frac{(V_1 + V_2)\phi - (V_1 - V_2)(\pi - \phi)}{2\omega L} \tag{2.19}$$

$$I_{mos} = \sqrt{\frac{t_2}{3}{I_1}^2 + \frac{t_3}{3}{I_\phi}^2 + \frac{t_4}{3}({I_0}^2 + I_0 I_\phi + {I_\phi}^2)} \tag{2.20}$$

$$I_{dio} = \sqrt{\frac{t_1}{3}({I_0}^2 + I_0 I_1 + {I_1}^2)} \tag{2.21}$$

As shown in the equations above, I_{mos} is the rms value of the semiconductor current. I_{dio} is correspondingly the rms value of the current through the antiparallel diode. I_1 represents the instantaneous current when the deadtime period ends. This current will vary depending on the selected deadtime and semiconductor. Equation (2.22) can then calculate the conduction loss by adding together the semiconductor and diode loss. This calculation is per bridge and has must be equated for both bridges to find the total conduction loss.

$$P_{cond} = 4({I_{mos}}^2 R_{on} + I_{dio} V_{fd}) \tag{2.22}$$

Magnetic loss

For the magnetic losses, two subcategories are applied, transformer and inductor losses. The texas instruments (TI), dual active bridge design guide [47], derives and describes these equations in detail. Transformer losses include the core, copper, and skin effect. The equation for the core loss is shown below in eq. (2.23).

$$P_{core} = P_v A_e \tag{2.23}$$

The core loss is here a product of the core loss per unit of volume (P_v) and the transformer volume (A_e). For the windings in the transformer, two parameters are of interest, the dc and ac resistance. The windings' dc components cause copper loss, which is calculated in eq. (2.24). Similarly, the ac component causes losses caused by skin effect at high frequencies, calculated in eq. (2.25).

$$P_{copper} = {I_{ac1}}^2 R_{DC_1} + {I_{ac2}}^2 R_{DC_2} \tag{2.24}$$

$$P_{ac} = {I_{ac1}}^2 R_{AC_1} + {I_{ac2}}^2 R_{AC_2} \tag{2.25}$$

The primary side (I_{ac1}) and secondary side (I_{ac2}) currents represented their respective rms values. R_{AC_1} and R_{DC_1} are the primary coil ac and dc resistance, respectively. Comparably R_{AC_2} and R_{DC_2} are the secondary coil resistances. Similarly, with the transformer, the inductors ac and dc resistance is used to calculate the power loss. These resistances can often be found in the transformer's datasheet, but may need to be calculated as in the inductor case. Equations (2.26) and (2.27) can thereby be applied for the calculations of the ac and dc resistance.

$$R_{DC,ind} = \frac{R_{max} 1.015^b 1.025^c}{N_s} \tag{2.26}$$

$$R_{AC,ind} = R_{DC,ind}\left(H + 2(\frac{N^2 {D_i}^2}{{D_o}^2})(\frac{D_i\sqrt{f_{sw}}}{10.44})^4\right) \tag{2.27}$$

R_{max} is the maximum DC resistance of each strand, while N_s is the number of parallel conductors. The notation of b is the number of bunching operations, furthermore c is the number of cabling operations. H is the ratio of individual strands, while N is the total number of strands. D_i is the diameter of the individual strands, D_o is the diameter of the inductor. As the inductor is located at the transformer's primary side, the primary current is used in calculating the power loss in eq. (2.28).

$$P_{ind} = {I_{ac1}}^2 (R_{AC,ind} + R_{DC,ind}) \tag{2.28}$$

2.3 Battery

On a commercial scale, there are several types of batteries represented. These batteries include but are not limited to lead-acid, nickel-metal-hydride (NiMH), sodium sulphur (NaS). vanadium redox flow (VRF) and lithium-ion (Li-ion) [17]. Each of the battery types has different characteristics and power capabilities. Batteries with lead-acid chemistry are one of the older battery types which still are utilized and in production. They have high energy efficiency and a low cost; however, they suffer from low energy density and a slow discharging rate. Applications where lead-acid often are used involve automotive applications and UPS systems [58]. NiMH batteries have increased values of both energy and power density compared to the batteries with lead-acid chemistry. The primary downside of this battery type is a high self-discharge rate and a low coulombic efficiency. The NiMH battery's primary use has been portable electronics and has previously been used in hybrid electric vehicle (HEV) [58].

For the NaS battery, the energy density is high compared to the previous battery types mentioned [59]. Another highly beneficial aspect of this battery type is its ability to operate under high temperatures. NaS has been an essential feature in renewable generation, like wind farms and solar plants [60]. Contrary to the other battery types, the energy and power capacities in the VRF are independent of each other. It has an excellent transient characteristic, which allows it to switch fast between charge and discharge. These qualities make it desirable for applications with variable loads, as renewables[61]. Li-ion is the leading battery in consumer electronics due to its high energy density and compact form. Additionally, Li-ion is currently the most common battery in EV and HEV. The battery used in cars will nevertheless have a slightly different chemistry than the consumer batteries. The price of the Li-ion has historically been its main disadvantage. However, the price has decreased as the electric car development and industry have increased [62]. Due to Li-ion batteries' popularity within HEV and EV, its characteristic and charging principle is reviewed further.

2.3.1 Characteristic

Figure 2.8 displays the discharge characteristic curve of a standard Li-ion battery. This characteristic has three different sections; the exponential, the nominal, and the depleted area. Located between voltages V_{full} and V_{exp} is the exponential area. In this section, the voltage decreases exponentially with the battery capacity. The nominal area located between V_{exp} and V_{nom}, is close to linear. This section is the curve's ideal area and where the battery should be operating during the nominal operation. The gray section in the figure showcases this nominal area. The depleted area located between V_{nom} and V_{co}, should ideally be avoided

to prevent battery damage. Here the battery voltage drops before it cuts off at the V_{co}, the lower voltage limit. This limit is to prevent the battery from entering deep depletion [63]. By avoiding the higher and lower state of charge (SOC) values, the battery will have a greater lifetime and state of health.

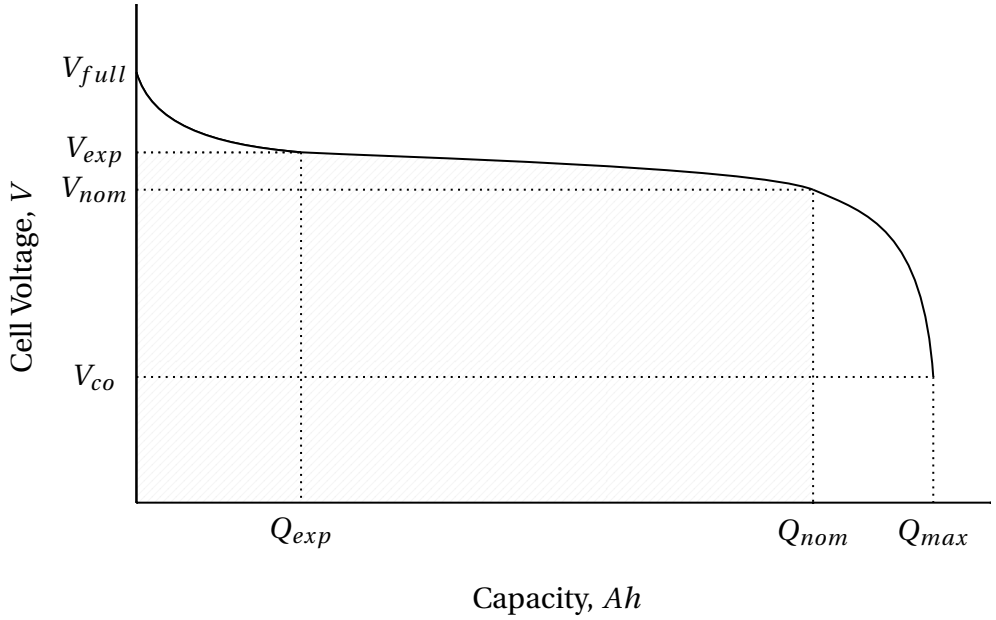

Figure 2.8: Discharge characteristic of a Li-ion battery

2.3.2 Charging Method

Due to Li-ion's unique characteristics, a charging method that can provide full charge without damaging the battery is required. Li-ion batteries' most common charging strategy is the constant current - constant voltage (CCCV)[64]. This method is divided into periods of constant current and constant voltage, as noted in fig. 2.9. After some time t_0, charging is initiated by the controller. During period t_1, the battery is supplied with a constant current while the battery voltage increases. Initially, the voltage increases rapidly until the capacity catches up, then the voltage is gradually increased.

At the end of period t_1, the voltage has reached its peak level. Here the voltage is kept constant, while the current decreases until the SOC reach 100%. This process's primary goal is to achieve a complete charge while still protecting the battery and preventing overcharging. The constant voltage regime will prolong the charging time, this step may be minimized for a faster charge time [64]. Another aspect of charging control is the C-rate. This parameter is the rate at which a battery is discharged compared to its total capacity [65]. A typical example used for explaining c-rate is; a 1 Ah battery that will deliver 1 A for 1 hour, as presented in table. 2.3. Not all C-rates are practical or possible to achieve. As the battery charges and discharges, the c-rate should not exceed the recommended level for extended periods [65].

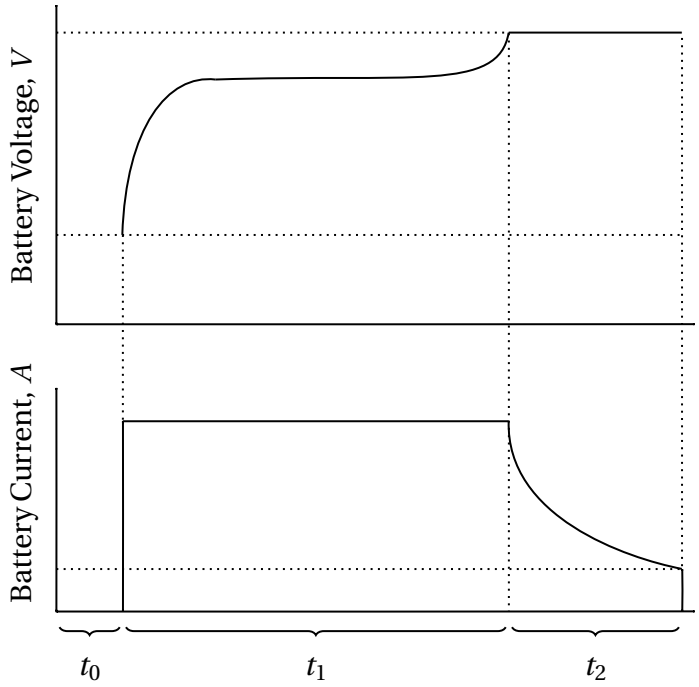

Figure 2.9: Battery current and voltage characteristic during cc/cv charging mode.

C-rate	Time	
5C	12	m
2C	30	m
1C	1	h
0.5C	2	h
0.2C	5	h

Table 2.3: C-rate for charging/discharging a 1Ah battery

2.3.3 State-Of-Charge

The SOC level represents the amount of charge currently available in the battery. A precise estimation is essential to prevent damage and reduced lifetime caused by either over or undercharging. A review of the different methods of calculating SOC has been made in [66]. In this paper, the calculating methods are divided into two primary groups direct and indirect methods.

The most straightforward approach is the direct method. With this procedure, the physical properties are measured and then used to calculate the SOC. Coulomb counting and open circuit voltage (OCV) are examples of this method. The most widely used method for estimating the SOC level is coulomb counting due to its simplicity. This approach calculates the current time integral, as shown in eq. 2.29 and eq. 2.30. The initial SOC level is required to be known as only the change in SOC is calculated.

$$SOC(t) = SOC(t_0) + \Delta SOC(t) \tag{2.29}$$

$$SOC(t) = SOC(t_0) + \frac{1}{C_{bat}} \int_{t_0}^{t+t_0} i_2 \cdot 100\% dt \tag{2.30}$$

$SOC(t_0)$ is the initial SOC value, while the $\Delta SOC(t)$ is the amount of change. C_{bat} is the rated capacity of the battery, and i_2 is the instant value of the current. However, this estimation method has a significant drawback as the error will be accumulative. These errors may transpire from an incorrect initial state or unexpected changes in the charging/discharging procedure. Additionally, the accuracy will decrease as the lifespan of the battery deteriorates [67].

OCV is another direct method, which has benefits from being an uncomplicated approach. The voltage potential over the poles is measured, the voltage characteristic is then is applied to estimate the charge. This approach does require the battery to be resting for a significant amount of time. It is therefore not applicable for active estimation.

The indirect methods combine the measured parameters with a simulated battery model. With these methods, the SOC level is predicted with a high degree of accuracy. However, these methods do introduce a greater level of complexity to the system. Model-based, adaptive filter-based and adaptive artificial intelligence-based are all alternatives within the indirect methods. The model-based estimation approach works by connecting a battery model and complex algorithms. The estimation is thereby a product of the actual current and voltage values. For the adaptive filter-based methods, a combination of both the indirect method and the model-based method is deployed. These techniques are adaptive and can correct any inevitable errors. For the correction, the technique applies a feedback signal from the output value. The artificial intelligence method is far too complex and demanding to be a practical method. The choice of SOC estimation is a balance of accuracy and complexity.

2.3.4 Battery Management System

An essential part of a functional battery operation is the battery management system (BMS). A BMS's role is to control a battery's operation through charging/discharging and standby monitoring. By controlling and monitoring the battery, the safety for both the battery and operator is significantly increased. The primary features of a BMS are cell monitoring, cell balancing, charge protection, charge control, thermal management, SOC, and state of health (SOH) calculations. Not all of these features are included in every system, but these are common characteristics[68], [69].

A battery pack incorporates several cells connected in series and parallel to obtain the required voltage and capacity. As no cell is fabricated perfectly alike, there will be imperfections and variations within the cell's structure. These variations will drive the cell to charge/discharge at slightly different rates. If a single cell is charging faster than the others and reaches its peak voltage, the charging process must stop to prevent damage to the cell. Therefore, cell monitoring and cell balancing are essential aspects of the BMS to prevent damage to the cells and surroundings.

As mentioned earlier, a reasonable charging control of the battery is crucial to increasing the lifespan and preventing damage. The battery SOC level should neither be driven too-low or too-high, where it either enters deep charging or overcharging. Deep charging is where the SOC is below a recommended percentage, and overcharging is where the battery is charged over its maximum voltage level. Both of these states can cause irreversible damage to the battery cells. For Li-ion batteries, temperature control is a critical aspect due to the chemistry of the battery. The operating temperature is affected by both the external ambient temperature and the battery's internal temperature caused by chemical reactions.

2.4 Software Tools

The software applications used in this thesis is presented in this subsection. The software is applied on a laptop with a 64-bit windows 10 operating system.

2.4.1 MathWorks Matlab®and Simulink®v9.8

Matlab®is a extensive math based programming application for calculation, programming and visualization. Simulink®is a Matlab®based graphical environment for designing and modulation of dynamical systems.

- Simulink v10.2
- Simulink Control Design v5.6
- Simscape v5.0
- Simscape Electrical v7.4
- System Identification Toolbox v9.13
- Stateflow v10.3

2.4.2 KiCad v5.1.7 and KiCad Libraries V1.4

KiCad is an open-source application for designing electronic systems and develop printed circuit board (PCB)s. KiCad contains a project manager, a schematic editor, a schematic layout viewer and a gerber viewer.

2.4.3 Visual Studio Code v.1.55 and PlatformIO v5.1.1

Visual Studio Code is a source code editor for programming, it supports most programming languages but C++ is used in this thesis. The platformIO os a free integrated developer environment for managing workflow, and is utilized for simpler software upload.

3 Method

Matlab®/Simulink®is used to design a simulation model of the dual active bridge isolated bidirectional dc-dc converter. A 30 V prototype battery system is created and tested with a laboratory test setup. To protect the battery a external battery management system and measurement card is designed and produced. This chapter is divided into five sections; Parameter Selection, Simulation, Battery Design, Battery Protection and Test Setup. In section 3.1 Parameter Selection, the selected values and justification for each selection is presented. In section 3.2 Simulation, the simulation model function and layout is described in detail. In section 3.3 Battery Design, the physical battery prototype is showcased. In section 3.4 Battery Protection, the measurement and battery management card is presented and explained. The source code, simulation model, and PCB layouts designed and presented in this chapter is found in Appendix C to E, and are published to separate public repositories on GitHub[77], [80].

3.1 Parameter Selection

In the design process of the DAB, various parameters have to be selected. The key parameters, switching frequency, leakage inductance, capacitance, are listed below in table 3.1 and discussed in the following subsections with justification for each parameter.

Table 3.1: Parameters for the dual active bridge simulation model.

Parameter	Value
Input Voltage	340 V
Output Voltage	200 V
Charging Current	4 A
Discharging Current	10 A
Switching Frequency	25 kHz
Leakage Inductor	0.289 µH
Input Capacitor	500 µF
Output Capacitor	500 µF

For the dc bus, an input dc voltage of 340 V is picked. This voltage level is available for a future physical project of the model. The nominal battery voltage of EV and HEV varies typically between 200-800 V. The lower value of 200 V input voltage is elected for this thesis. As the battery module is designed with 18650 lithium-ion cells, the current is limited to 5.2 A charging and 10.4 A discharging. These values are decreased to 4 A charging and 10 A discharging to decrease any potential damage to the batteries. The selections are described in detail in the following sections.

3.1.1 Switching Frequency

The functionality of the converter is dependent on the selection of switching frequency. It directly affects several components as the transformer, leakage inductor, controllable switches, including the efficiency and power density. With an increased switching frequency, the magnetic components' physical size can be reduced [70]. However, this increase in frequency leads to an increase in switching losses as the semiconductors switching speed is raised. Furthermore, the frequency is limited by the skin and proximity effect on the ac side [47], [49]. The skin effect is a phenomenon where the current flows through the surface of the conductor. As the frequency increases, the current will therefore flow more towards the surface layer. With the current flowing more in the outer skin, the effective cross-section will be lower, increasing resistance. Similarly, the proximity effect causes the current to only flow towards the areas furthest away from nearby conductors. This increase in resistance leads to an increase in losses and a drop in efficiency. The ability of the converter to both charge and discharge the battery with a high response are achieved more easily with a higher frequency.

The choice of switching frequency will therefore be a trade-off between efficiency and physical size. The effect of the frequency on the power flow is shown in eq. (2.1) presented in section 2.2.2 Power Flow. With a higher switching frequency, the output power from the converter reduces. A compromise between the mentioned parameters has been made, and a switching frequency of 25 kHz is selected as the primary switching frequency.

3.1.2 Leakage inductor

L denotes the leakage inductance and is one of the critical components of the DAB. Together with the transformer, the inductance determines the amount of power that can transfer between the primary and secondary bridge. The inductance size is heavily dependent on the switching frequency as it is a magnetic component. With a higher switching frequency, the physical size of the inductance can be decreased considerably. The inductance should be designed to handle the required power transfer at each specific phase shift. Therefore the phase shift must be selected where inductance experiences its maximum power. The trans-

ferred power will be at its peak at 90 degrees or 0.5π radian phase shift. The phase shift angle is presented as π radian in formula eq. (3.1), where the total inductance is calculated. With a maximal phase shift of 90 degrees or 0.5π, the total leakage inductance is calculated as 289 µH. As there will be a small amount of transformer leakage inductance, the inductor must therefore be below the calculated value. This formula are derived from eq. (2.1), in section 2.2.2.

$$L = \frac{\phi(1-\phi)V_1V_2}{2f_{sw}nP_{out}} \tag{3.1}$$

3.1.3 Capacitors

The capacitors located at the input and output ports of the DAB model are utilized to lower the voltage ripple of the converter to an acceptable level. The capacitor current(i_{C2}) will be a function of the battery current(i_2) and the output from the semiconductor switches(I_{ac2}), as seen in eq. (3.2). The output ripple requirement varies from design and application. For this design, a low voltage ripple and current ripple of below 2% is desired. From this basis, a capacitor of value 500 µF is selected through trial and error in the simulation.

$$i_{C2} = I_{ac2} - i_2 \tag{3.2}$$

3.1.4 Switching devices

Silicon MOSFETs and IGBTs have traditionally been the primary choice for the controllable switches in DAB converters. Recently progress has been made with silicon carbide (SiC) MOSFETs, which is a maturing technology. The bandgap in the newer SiC MOSFETs is designed with a substantially wider bandgap than the typical SI MOSFET. In addition, the drift layer for a specific blocking voltage is up to 200 times less resistive [71]. Advantages with SiC are a higher breakdown voltage and excellent thermal properties [72] [73]. These advantages increase the theoretical frequency limit by lowering the losses. The physical size of the converter may also be reduced as the smaller cooling components can be used due to the efficient thermal conductivity.

A performance comparison between si MOSFETs, IGBTs, and SiC MOSFETs has been made in [74]. The paper presents a shorter turn-on and turn-off time for the SiC MOSFET. Nevertheless, the conduction losses of the SiC MOSFET were higher than the silicon counterpart. The SiC still shows the most theoretical promise under higher switching frequencies. The IGBT performs significantly worse and should not be considered. With SiC, it is possible to achieve lower switching and conduction losses while operating at high temperatures [75].

Due to the combined advantages, SiC is preferred as the primary semiconductor switch for this project. The performance parameters of the IMZA65R027 SiC MOSFET from infineon is selected for the semiconductor on both bridges. Table 3.2 presents the critical performance parameters of the device. The rated nominal voltage (V_{DS}) is 650 V with a continuous drain current (I_D) 59 A at 25 °C. The drain-source on-state resistance (R_{on}) is 27 mΩ, and the total gate charge (Q_G) is 63 nC. The I_D, pulse of 184 A is the pulsed drain current, the maximum current it can endure over a short period.

Table 3.2: Performance parameters for SiC MOSFET IMZA65R027M1H

Parameter	Value	Unit
V_{DS}	650	[V]
R_{ON}	27	[mΩ]
Q_G	63	[nC]
I_D	59	[A]
$I_{D,pulse}$	184	[A]

3.1.5 Transformer

Similar to the leakage inductor, the transformer has a dependency on the switching frequency. With higher values of frequency, a more compact and efficient system can be designed. Planar transformers are, consequently, optimal transformers due to their compact size and ability for higher frequencies. These transformers are constructed with winding turns of thin copper sheets riveted together instead of the standard wire-wound transformers, which increases the power density. The consistent spacing between the layers makes the inductance more predictable [47], [76].

Realistic values from a 2 kW planar transformer from HiMAG are selected. This transformer is not in production, but it can be special ordered if required. The rated voltages are 340 to 200 V with a turn ratio of 28:17. The estimated power core loss is 13 W, while the estimated winding loss is 4 W.

3.2 Simulation in Matlab®/Simulink®

The simulation models are designed and simulated with Simulink®, a Matlab®-based graphical programming tool for modeling and simulation. Two simulation models are produced, the primary bidirectional dc-dc converter model and a simplified simulation model for testing the battery response. The primary model utilizes the DAB topology with a single inductor in the primary bridge presented in section 2.1.3. The secondary simulation model, is a simplified version of the laboratory test setup. This model showcases the transient response of the simulated battery model by connecting the battery to a load through a lossless switch. For the electrical circuit components, the simscape electrical library is utilized for both simulation models.

3.2.1 DAB Converter Model

Figure fig. 3.1 show, the main simulation model of the isolated bidirectional dc-dc converter with an DAB topology, and the entire simulation model is found in appendix C and published in repository [77]. The dc bus is modeled by a constant dc voltage source connected in series with a resistance. For the low voltage side, the battery is represented by a generic battery model. This battery is modeled after a lithium-ion battery, with its specific characteristics. SPS modulation controls the power flow between the bridges. As the converter is operating in buck-mode, delivering power from the dc-bus to the battery, the phase shift is shifted positively with regards to the primary bridge. Similarly, when operating in boost-mode, the phase shift is shifted negatively. PI controllers set the desired phase shift based on the required state. Out from the PI controllers, the signal is scaled down and fed into a "moving average" block to smooth the signal by computing the moving average of the input value.

Both bridges require two gate signals each to operate. Four pulse generators create these square wave signals. Discrete variable time delay blocks are implemented to achieve a phase shift between the square wave signals. The computed phase shift delay signal sets the amount of phase shift. A single PI controller signal can control both directions of power by changing the polarity of the delay signal between the bridges. As the time delay blocks cant delay negative values, the delay will be set to zero. Only one of the bridges will therefore be delayed, depending on the polarity. As the converter turns on, the capacitor current increases to a too high level as the capacitor charges. A pre-charging circuit is therefore required to decrease the initial current of the converter. The input capacitor is charged to 340 V dc before the bus is connected to the converter. Similarly, the output capacitor is charged to 184.4 V dc before the battery is connected. When both the DC-bus and battery are connected to the model, the operation of the converter can be started.

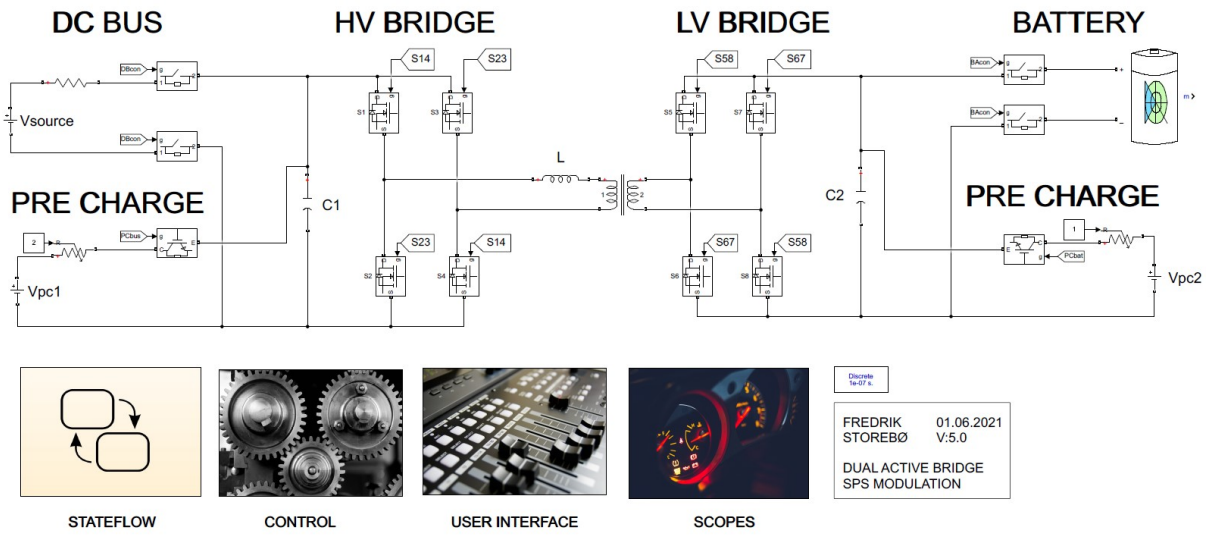

Figure 3.1: Simulation model of the isolated bidirectional dc-dc DAB converter.

Stateflow

Several states for operating the converter are defined, OFF, PRECHARGE, ON, CHARGE, and DISCHARGE. Stateflow is implemented to switch between the different states. The stateflow blocks can be found in appendix C.2, and appendix C.2.1. During the initializing phase of the model, it will be in the OFF state. In this state, the converter is switched off, and both the bus and battery are disconnected. The next possible state is the PRECHARGE state, where both the input and output capacitor is charged. After reaching the required charged voltage, the bus and battery will connect to the converter. When both the bus and battery have connected, the state switched to ON. In this state, the current and voltage reference is zero, and the converter can be set to either CHARGE or DISCHARGE mode. In CHARGE mode, the battery will either deliver a constant current of 4 A or a constant voltage of 200 V depending on the SOC. While in DISCHARGE mode a discharge current of -10 A is set.

The model can be turned off at any stage of the stateflow if a stop signal is sent. In addition, an override control can be activated for testing purposes. This control can be activated while the converter is switched on and will override all the other control signals. The phase shift can then be set to any level that is required.

Control

The control tab contains three blocks, PI, SIGNAL GENERATOR, and CALCULATION. This tab is shown in appendix C.3. The PI block shown in appendix C.3.1 controls the phase shift to be applied. The phase shift value is regulated by three PI controllers, depending on the state of the model. A Matlab script switches between the PI controllers, as the model is either charging with constant current, charging with constant voltage or, discharging. By having several controllers, each controller can be tuned specifically for a required response. The implemented Simulink Control Design software calculates the PI gains. This software computes a linear model of the plant from the input and outputs. The plant represents every block in the control loop, apart from the controller. The I/O data are then accumulated by simulating the model over a short period. From these data, initial gain values are presented with a target phase margin of 60° and a crossover frequency based on the plant. The response can then be refined to achieve a faster/slower, or aggressive/robust system. Table. 3.3 presents the gain values for each PI controller. The two controllers with constant current show apparent similarities, while the constant voltage controller shows considerably greater values.

Table 3.3: PI regulator values from the control section of the DAB simulation model

Controller	Object	Proportional	Integral
Discharge	Current	0.128446793065259	1091.25323028373
Charge CC	Current	0.405243677304324	1694.18611330183
Charge CV	Voltage	14.1158220351783	266471.123289708

The signal generator block shown in appendix C.3.2 produces two square wave signals for each bridge. These signals are half a period out of phase of another, as described in section 2.2. The time delay blocks then delay either bridge depending on the polarity of the phase shift signal. The calculation tab calculates the different values presented and used in the model. This simulation tab can be found in appendix C.3.3. The input and output power are calculated from the current and voltages; these are then used to calculate efficiency. The phase shift is recalculated to represent the percent of the total period, as this is more easily read. The SOC is determined with coulomb counting by calculating the current time integrative. This method is described in more detail in section 2.3.3. The precharge values are only displayed while precharging to prevent misleading values in the user interface. The model and measured signal are gathered from a multimeter block to be presented in other parts of the simulation model.

User Interface

The simulation includes a user interface window to control and survey the status of the converter model, see fig. 3.2 and appendix C.4. The battery and bus can be connected and disconnected from the converter. The status of this is shown by indicator lamps and a figure of the model that updates accordingly. The figure also presents the power flow direction while running. The precharge circuitry is shown by the voltage difference between the capacitors and bus/battery. The capacitors' charge current is presented similarly; this value is adjustable by changing the resistor values. After connecting the battery and dc-bus, the model can be charged or discharged. Lamps indicate the current state of the converter and available modes. When running, the input and output voltages is presented as instantaneous values. In addition, the battery voltage and current are plotted in two scopes. The actual phase shift is presented with both percent and time delay.

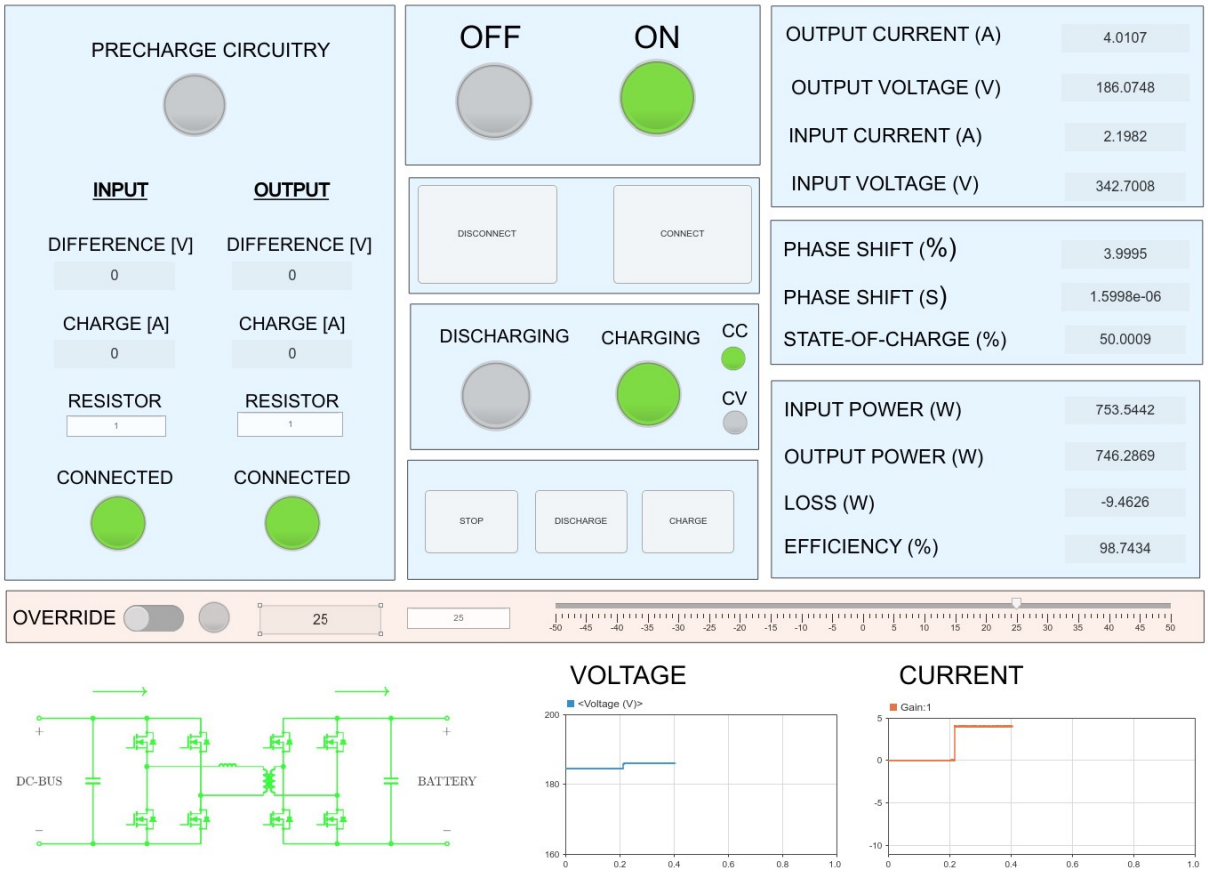

Figure 3.2: User interface for controlling and supervising the simulation isolated bidirectional DAB converter model.

The SOC, input power, output power, loss, and efficiency are calculated in the calculation tab and displayed in the user interface as instantaneous values. The respective voltages and currents calculate the power values, which are again combined to calculate the loss between the bridges. Depending on the direction of the power flow, these values will update to show losses from the delivering bridge to the receiving bridge. For testing purposes, the phase shift can be overridden and manually adjusted to the required level. This mode can be initiated after connecting the battery and dc bus. This functionality is powerful to get knowledge of the model and test different scenarios. The value is limited between -50 and 50%. During regular operation, the phase shift should not exceed -25 to 25%.

Scopes

The scope tab located in appendix C.5, has all the relevant measured signals readily available. The signals are divided into four sections depending on the type of signal. Extra scopes and mux are presented, and the measured signals can easily be copied in and used. This system makes it simple to easy access to every signal without cluttering the model.

3.2.2 Battery Model

A simplified simulation model is designed to test and compared the transient response of the simulated battery model with the physical battery prototype created. This secondary model only focuses on the battery response and not the isolated bidirectional dc-dc converter. The design shown in appendix D, is constructed by 16 battery cells connected to a load through an ideal switch. A step signal is sent to the ideal switch, and the following voltage and current are recorded. The battery cells are modeled after the physical cells used in the battery prototype.

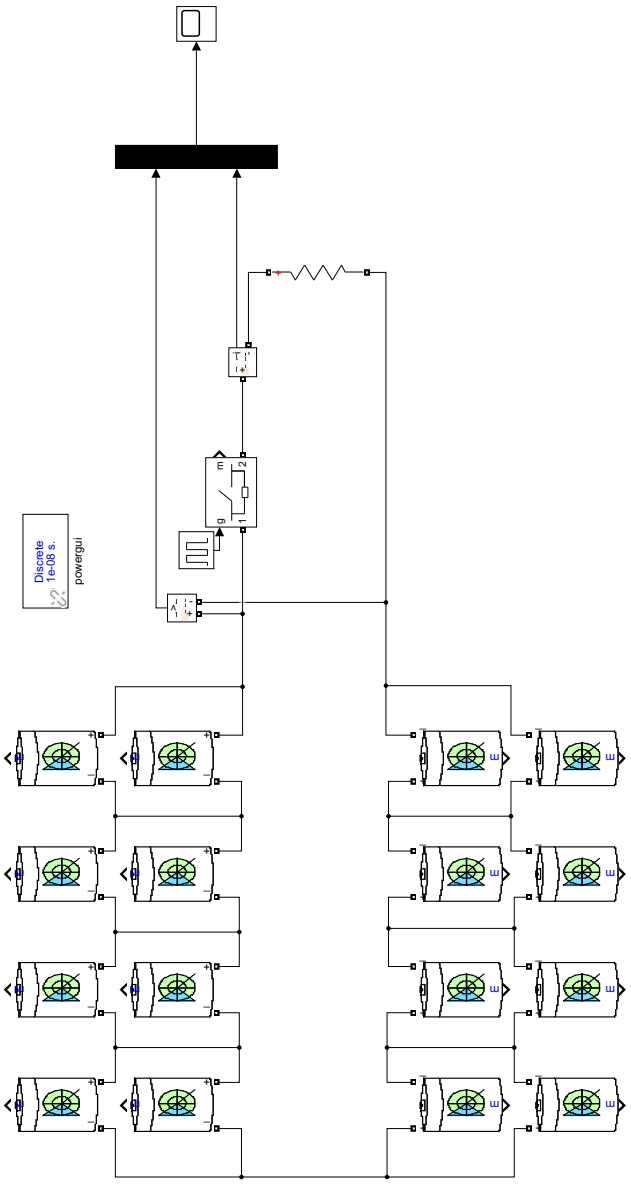

Figure 3.3: Simplified battery simulation model for testing the battery response.

3.3 Prototype Battery System

For the DAB converter, a 200 V battery pack was initially discussed. Since the converter will not be constructed, a smaller battery pack prototype for demonstrating the principle is designed. This pack can easily be increased at a later stage by adding more packs in series. The battery pack is constructed with lithium-ion cells where each cell has a nominal voltage of 3.7 V and a capacity of 2.6 Ah. The battery is designed as two packs of 4S2P, four cells in series and two in parallel. A total of 16 cells are divided into two packs, which provide a total nominal voltage of 29.6 V with a capacity of 5.2 Ah. The nominal specification of the total battery pack and a single cell is shown in section 3.3 respectively.

The lithium-ion cells are distributed evenly in a grid restricted by spacers. The cells are welded together in the series and parallel formation with nickel by a spot welder. The two separate packs are then serially connected at the terminals. Several packs can be connected later in this formation to increase the voltage to the desired level.The battery packs are shown in fig. 3.4a, and the welding structure is shown in fig. 3.4b.

Chemically no battery cell is entirely identical. Therefore they will charge at slightly different rates, which may cause irreversible damage to a cell if it becomes overcharged. A battery balancing system is required to prevent this level of overcharging to the cells. Stuart Pittaway [78] has designed an open-source BMS, openly available on github [79]. This open-source BMS project includes a battery protection system and passive cell balancing. In addition, the open-source BMS system has inbuilt software that connects to the local network to read the battery values. A separate PCB measurement card is designed to measure the voltage and current of the pack directly to a microcontroller.

Table 3.4: Nominal specification of the total battery prototype pack

Parameter	Value
Cell(s)	16
Nominal Voltage [V]	29.6
Charging Voltage [V]	33.6
Capacity [Ah]	5.2
Charging Current [A]	5.2
Discharging Current [A]	10.4

Table 3.5: Nominal specification of a single lithium-ion cell

Parameter	Value
Cell(s)	1
Nominal Voltage [V]	3.7
Charging Voltage [V]	4.2
Capacity [Ah]	2.6
Charging Current [A]	2.6
Discharging Current [A]	5.2

(a) Battery pack

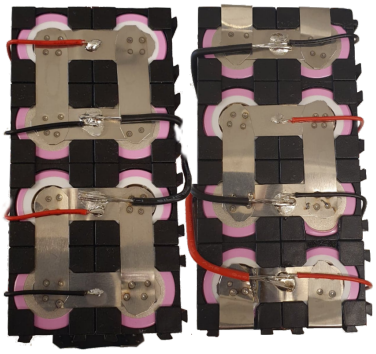

(b) Welding structure

Figure 3.4: Physical battery prototype system

3.4 Battery Protection

For the measurement, battery control, and battery protection, PCBs has been implemented with the battery prototype pack. A single voltage and current measurement PCB is designed and built. The BMS PCBs have been implemented accordingly with the instructions provided on the open-source project page. These include one controller for the entire system and a single sensor card for each cell pair.

3.4.1 Measurement PCB

For measuring the voltage and currents in the system, a measurement PCB is designed; see fig. 3.5. The card is designed with the PCB design software KiCad EDA. The schematic is drawn with the built-in schematic editor in KiCad. Similar to the schematic, the board layout is designed with the PCB designer in KiCad. The entire PCB schematic is found in appendices E.1.1 and E.1.2 likewise, the front and back copper layout is found in appendix E.1.3 and appendix E.1.4 respectively. The entire PCB design created in this thesis is published to repository [80]. The designed measurement card allows for voltages up to 60 V and currents up to $\pm$ 50 A.

The circuitry is devised to be powered by a 15 V DC power supply. A dual-element bi-directional ESD is utilized to protect the supply. In an instant of increased voltage over the nominal level, the ESD protector's internal resistance will decrease rapidly to prevent damage to the circuitry. Out from the main power supply, a 3.3 V signal is produced with the "MIC5225" dropout regulator. This 3.3 V powers both the voltage amplifier and current sensor. In addition a 5 V is generated from the 15 V main power supply. The 5 V is produced with a "TPS82130" step-down converter and is further isolated by transforming up to +6 V through

a galvanic isolated transformer. The isolated signal is then transformed back down to 5 V from 6 V by a "TLV704" low-dropout regulator. This signal is thereby galvanic isolated from the rest of the circuit. The design allows for up to 60 V to be measured. A voltage divider at the input lowers the voltage to the required level of 0-250 mV. The signal is then filtered through a small RC filter before it connects to the "AMC1100DUBR" fully-differential isolation amplifier. This amplifier has an output that is completely separated from the input by a silicon dioxide barrier. On the isolation side, it is supplied +5 V isolated, while on the non-isolated side its supplied +3 V.

For the current measurement, a simple and effective design is implemented with the "ACS758PFF" current sensor. The sensor is a hall-effect-based linear current sensor that creates a magnetic field converted to a proportional output voltage. The primary high current side is then isolated from the small control signal. The PFF leadform of the current sensor selected can measure ±50 A.

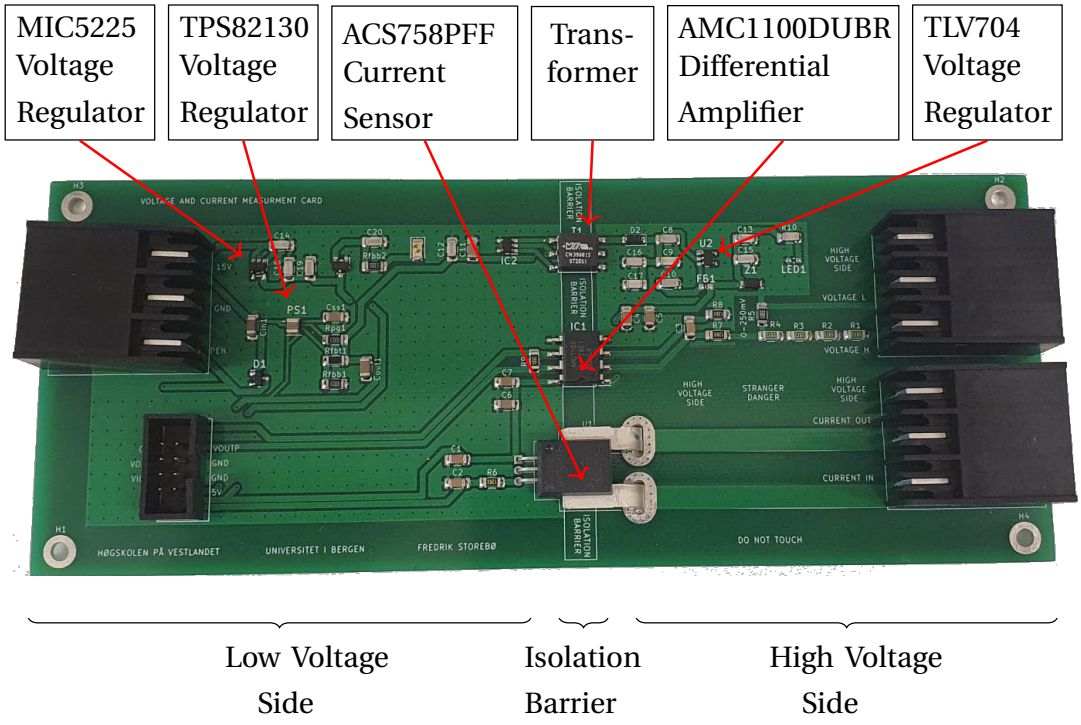

Figure 3.5: PCB for current and voltage measurement

3.4.2 BMS PCB

The design of the BMS, is based on a open-source project on Github [79]. This project is primarily designed by Stuart Pittaway [78], and have been in development since 2015, with several iterations released. The latest stable release is version 4.40, however version 4.0 is picked for this project due to its bigger component sizes. The components are in this previous version possible to hand solder and easier to modify. The code for programming the sensor and control cards are supplied in a separate repository [81]. Each board is ordered from JLCPCB, while the majority of the components are supplied from Mouser. The component size used for the resistors and capacitors is size 0508. These sizes provide a compact size while still being placeable by hand.

The system consists of a single control card connected with a sensor per cell. As the connected battery pack is designed as an 8S2P(8 series and 2 parallel), eight sensor cards are necessary. This layout is displayed in fig. 3.6, where the control and sensor card block diagram is shown. The cards communicate by standard UART serial communication. Each card has a transmitter port TX and a receiver port RX. The transmitter port of a specific card is connected to the receiver port of the next card. With this setup, each card can be explicitly controlled or be control together as a unit. In addition, each sensor card can respond to the controller with information about the connected battery cell.

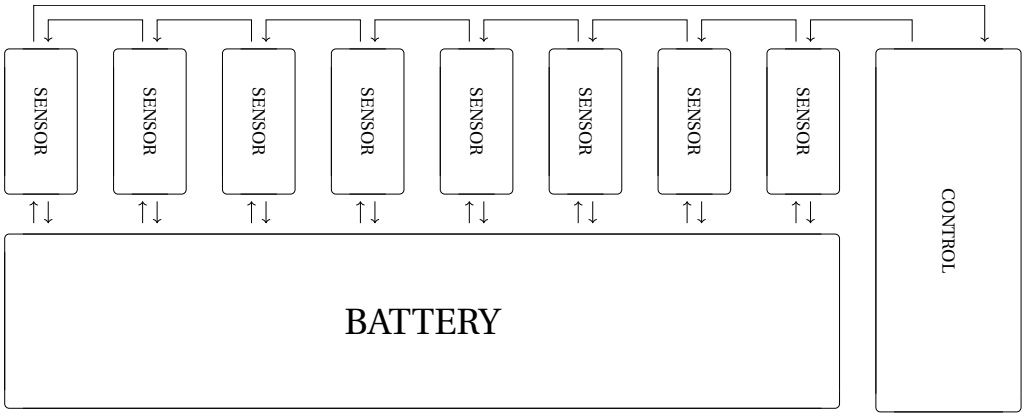

Figure 3.6: Battery management system block diagram

Control card

A single control card is necessary for each cell pair. The controller is presented in fig. 3.7, all the schematic and copper layouts are found in appendices E.2.1 to E.2.3. The role of the control card is to read and control the signals from the entire circuit. The control card reads the serial signal from the sensor cards. With the help of the IO expander "PCF8574T," a WeMos d1 mini wifi board reads these signals and converts them to understandable data. To display these values from the system, the board connects to the local network and sets up a webpage. All the measured values can be read from this page, and instructions to a specific sensor card or every card can then controlled.

For programming, the WeMos mini connects to a computer through a micro USB. The code is supplied in a separate repository on Github[81]. The code editor Visual Studio Code is used as the interface between the code and the controller. The platformIO integrated development environment extension is applied to simplify the programming experience.

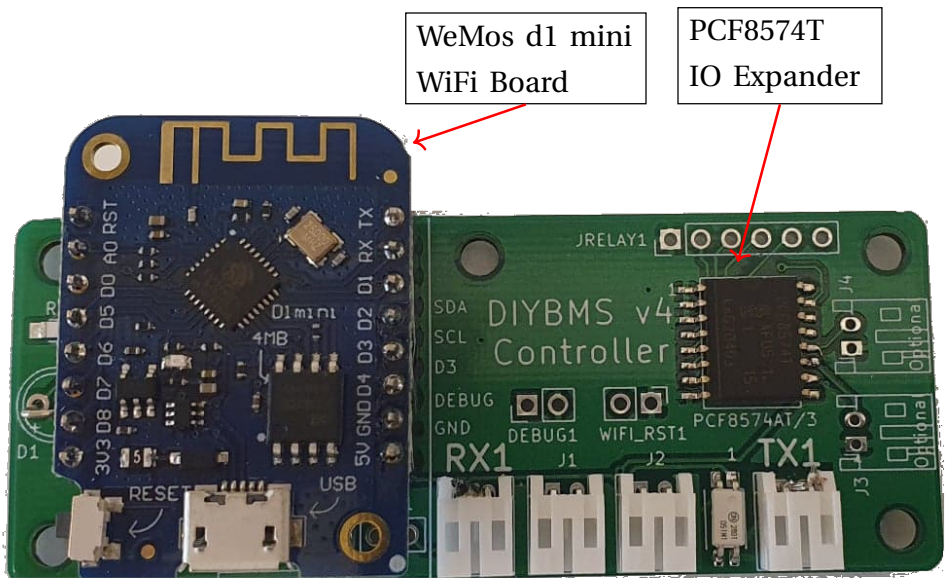

Figure 3.7: BMS controller for controlling the battery management system

Sensor card

Figure 3.8 shows a single sensor card. Eight of these cards are required to achieve the complete BMS. The electric schematic is found in appendix E.3.1, similarily the front and back copper layout is found in appendices E.3.2 and E.3.3. The "ATTINY841" microcontroller controls each sensor card with 8K bytes in-system programmable flash. The TX signal is isolated from the circuit by a phototransistor optocoupler. The passive cell balancing system is included in each card separately. Two rows of 4 2.2Ω 1W resistors are used to dissipated the surplus energy. Each row will then have a resistance of 8.8 Ω and dissipate a maximum of 4 W, with a current through the circuit of around 470 mA.

As the cell voltage increases past a variable limit, the microcontroller transmits a gate signal to an "IRLML6244TRPBF" N-channel MOSFET, which bypasses the current through the resistors. The circuit will operate with either a constant ON signal or a PWM signal. This signal mode is depending on the voltage difference between the cells. The balancing circuitry is displayed with a red led light, which will turn on while the MOSFET is conducting and the cell is discharging. As the battery cell discharges to a lower voltage level, the pack will be balanced. This cell balancing feature can operate in standby mode without being connected to a primary controller. In addition to cell balancing, the sensor card measures both the cell voltage and current level. An option for an external temperature sensor is available, but this is not required for regular operation.

For programming the microcontroller in the sensor card, a programming device is required. The USBasp programmer is selected as the bridge between the computer and chip. Like programming, the controller card, the platformIO extension with visual studio code is utilized to upload the code. The code is located in the same code repository on github[81].

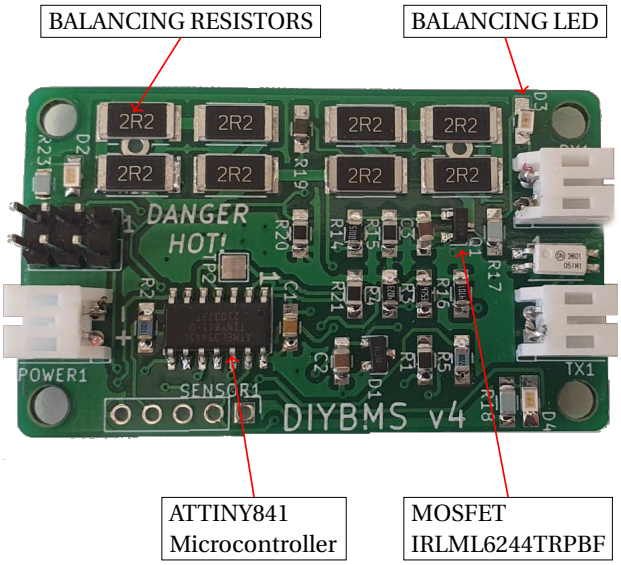

Figure 3.8: BMS sensor for balancing and sensing a battery cell

3.5 Test setup

The experimental setup for testing the battery depicted in fig. F.1 consists of a programmable load, charger, battery, BMS, multimeter, and oscilloscope. These components are listed in table 3.6. For charging the battery up to the required voltage level, an E680 battery charger from SkyRc is used. The BMS project described in section 3.4.2 is utilized with the battery during charging to achieve cell balancing. After reaching the required voltage level, the EL 9500-08 T electronic DC load is used to examine the battery response. The load has a maximum input voltage of 500 V with an equivalent maximum current of 8 A. These values are adjustable with intuitive touchscreen controls and settings. The dc load contains a function generator, which can generate various signal characteristics and apply these to the current.

The function generator is set to the rectangular wave. The adjustable parameters are the amplitude, offset, and pulse width of both the upper and lower level. These values are shown in table. 4. With a pulse width of 1ms and a duty cycle of 50%, a frequency of 500 Hz is achieved. An MSOX3014A oscilloscope measures the current with a CP2100A current probe. For the voltage measurement, the DP10013 differential probe is used. The current probe has a bandwidth of 800 kHz and an accuracy of 3% or ± 50 mA while measuring 10 A. Similar the voltage differential probe has a bandwidth of 100 MHz and an accuracy of ± 2%

Table 3.6: Laboratory test equipment

Type	**Manufacturer**	**Type**
Programmable Load	Elektro-Automatik	9500-08 T
Oscilloscope	Keysight	MSOX3014A
Multimeter	Keysight	U1242
Diff. Probe	Micsig	DP10013
Current Probe	Micsig	CP2100A
Battery Charger	SkyRc	E680

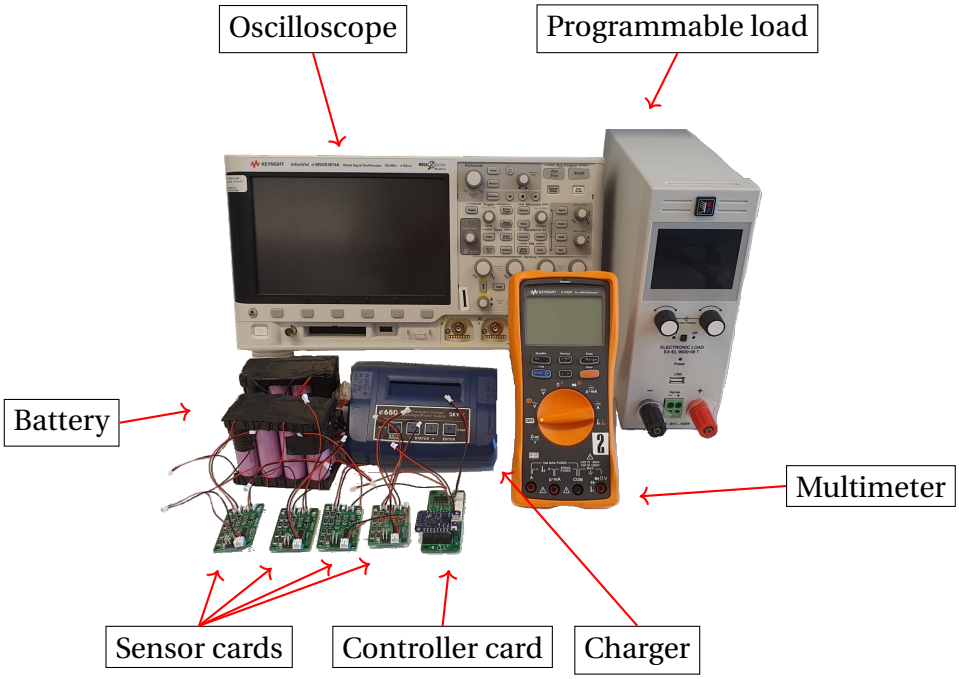

Figure 3.9: Complete prototype battery system and laboratory test equipment

Table 3.7: 9500-08 T programmable load function setting

Parameter	**Value**	**Description**
Amplitude	2,4,6,8 A	Amplitude of generated wave
Offset	0 A	Offset of the generated wave
t_1	0.01 s	Pulse width of upper level
t_2	0.01 s	Pulse width of lower level

4 Results

The isolated bidirectional dc-dc converter simulation model, the simplified battery simulation model, and the physical battery prototype system are tested in this chapter. The relevant results from both simulations and the experimental lab setup are inspected and analyzed. This chapter is divided into two primary sections. Results from the isolated bidirectional dc-dc converter simulation are presented in section 4.1. Three aspects of the model are displayed, the battery response in section 4.1.1, the powerflow in section 4.1.2 and the soft switching ability in section 4.1.3. The simulation model is simulated in both buck and boost mode, as shown in table 4.1. While charging in buck mode, the current reference is set to 4 A with a constant current. Similarly, the voltage reference is set to 200 V with constant voltage. While discharging in boost mode, only the current reference of -10 A is applied. The simplified battery simulation and the experimental battery prototype results are presented in section 4.2, where the transient response of the models is analyzed.

Table 4.1: Simulated modes from the converter simulation

Reference	Reference	Value	PI Output
Buck	Current	4 A	1.6 µs
Buck	Voltage	200 V	Decreasing
Boost	Current	10 A	-4.4 µs

4.1 Isolated bidirectional dc-dc converter simulation

4.1.1 Battery Response

Charging With Constant Current

Figure 4.1 presents the simulated values for both the battery current and PI output of the secondary bridge during battery charging with a constant current. The battery SOC is at 50%, with a no-load voltage of 184.4 V. At time zero, the reference current is set to 4 A. Some key parameters from the current and PI output characteristics are exhibited in table 4.2. The transient response curve of the battery current shown in fig. 4.1a, has a settling time of approximately 2 ms, with a rise time of 455 µs. The rise time(T_R) is defined as the time difference between 10 and 90% of the final steady-state value. After 2 ms, the steady-state value of the current ripple is recorded and presented in fig. 4.1b. The current value varies between 4.05 A and 3.97 A, thereby staying within 2% of the total battery current.

The phase shift response from the PI regulator exhibited in fig. 4.1c is presented as µs. The period of the square voltage wave is 40 µs, and the maximum allowable PI output will therefore be ±10 µs which equals ±25% or $\frac{\pi}{2}$ rad. The PI output rises quickly from -0.3 µs, with a rise time of 29.6 µs. The phase shift overshoots to 1.8 µs before declining, obtaining 12.5 %OS of the 1.6 µs steady-state value. The steady-state value in fig. 4.1d shows a slight variation of 12 ns between 1.604 µs and 1.592 µs. This variation results in a 0.75% ripple of the steady state value of 1.6 uS. With a period of 40 µs, 1.6 µs equals 4% of the total period. The secondary ac voltage wave is thereby phase shifted 4% behind the primary ac wave.

Table 4.2: Battery response parameters while charging with constant current

Parameter	Current	PI
SS	4 A	1.6 µs
T_R	455 µs	29.6 µs
T_S	2 ms	1 ms
$\%OS$	0 %	12.5 %
Ripple	2 %	0.68 %

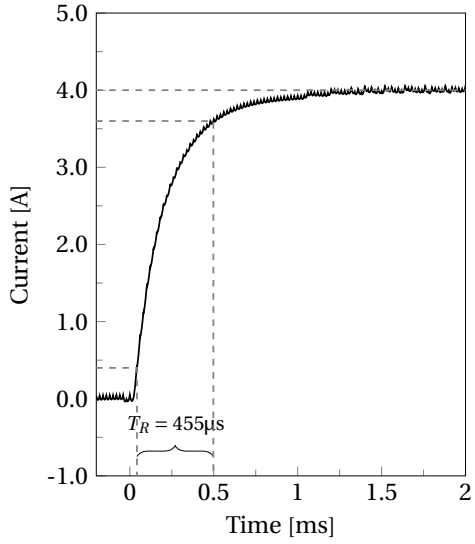

(a) Current transient response

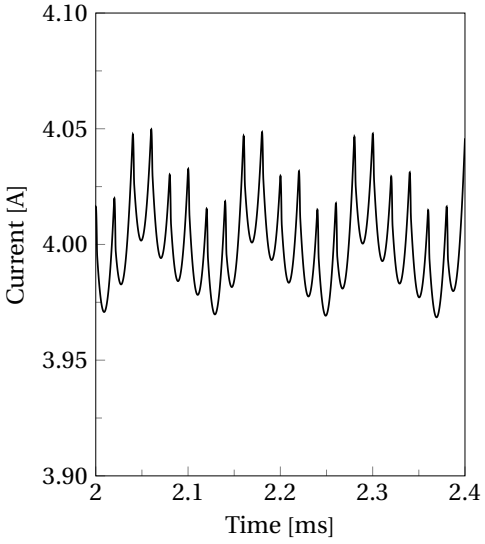

(b) Steady state current ripple

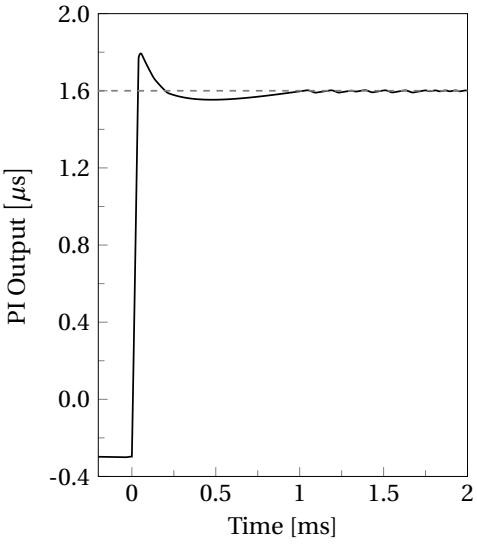

(c) PI output transient response

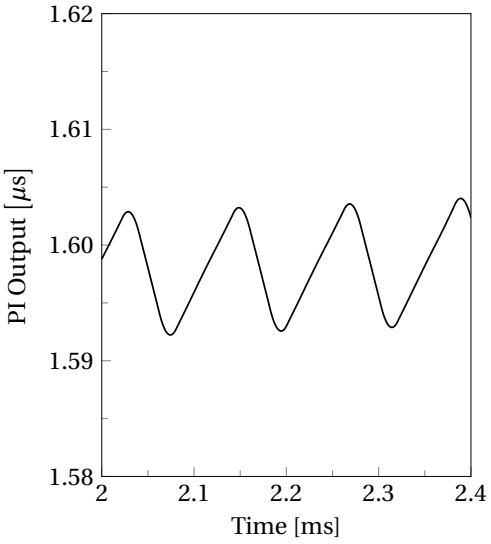

(d) Steady state PI output

Figure 4.1: Battery current and PI output presented with their transient response and their following steady state ripple with a battery charging current of 4 A

Charging With Constant Voltage

At the end of the battery charging cycle, the lithium-ion cells are top charged to fill the capacity. A constant voltage is provided to prevent damage to the cells. Figure 4.2 displays the battery current and voltage response alongside the phase shift output from the PI controller. Since the constant voltage mode is only applicable for top charging at the end of the charging cycle, it is not relevant for discharging scenarios. The SOC level is set to 99%, and the converter model is in charging mode.

The current and voltage response as the model switches from applying a current reference to a voltage reference is shown in fig. 4.2a. This transition occurs after the voltage has reached the 200 V limit of the battery. A Matlab script in the control section switches the functioning PI controller, and the reference is set to 200 V. The voltage goes from an increasing trend to a stable 200 V. Conversely, the current goes from a steady 4 A to a decreasing trend, as the PI output is decreasing. The steady-state voltage ripple is shown in fig. 4.2b while delivering a constant voltage of 200 V. The voltage stays between 200.03 and 199.96 V, which is a ripple value of 0.035% of the entire 200 V. The PI output presented in fig. 4.2c, shows an increased instability as the mode switches reference from current to voltage. The average value of the PI output is decreasing after the transition. The ripple value of the signal is showcased in fig. 4.2d. Since the signal is constantly decreasing, no stable ripple value is shown. However, an average ripple of 18.75% can be seen.

Table 4.3: Battery response parameters while charging with constant voltage

Parameter	Voltage	Current	PI output
SS	200 V	Decreasing	Decreasing
Ripple	0.035%	3%	18.75%

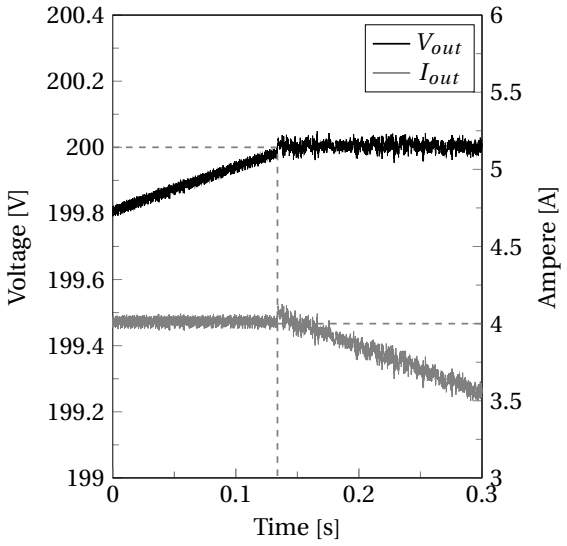

(a) Battery voltage and current transition to CV

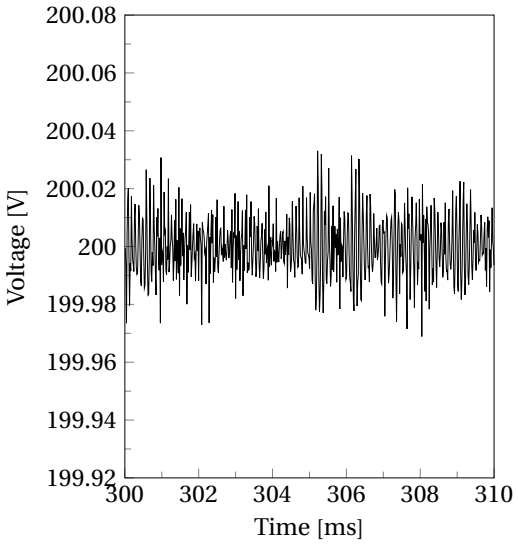

(b) Battery steady state voltage ripple in CV

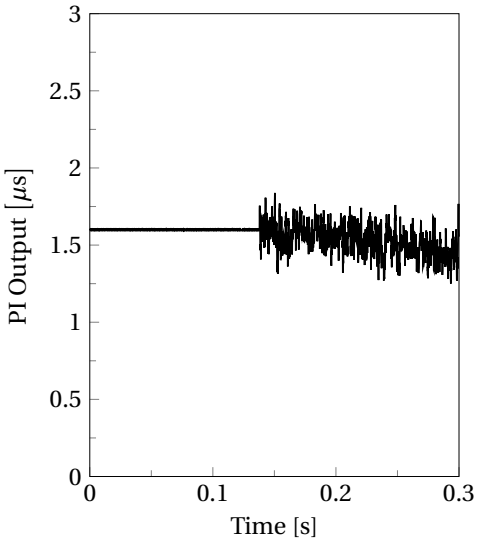

(c) PI output transition to CV

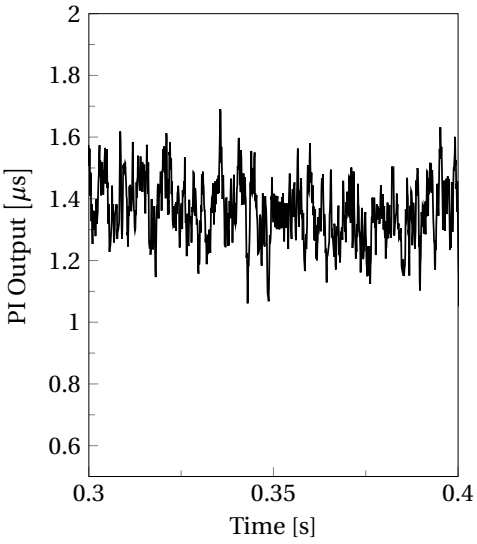

(d) PI output ripple in CV

Figure 4.2: Battery voltage and current characteristic while transitioning from CC to CV mode, including the associated steady state voltage ripple while in constant voltage. The battery voltage level is kept at 200 V while in CV mode.

Discharging With Constant Current

The results in fig. 4.3 show the current and PI output of the secondary bridge, as the model is discharging. The power flows from the battery to the dc bus, as the negative values indicate. The battery is at 50% SOC, and the reference current is set at a constant value of -10 A at time zero. Figure 4.3a shows the transient response of the battery current. The current decreases with a steady curve until it settles at the required -10 A. The response time from 10 to 90% of the final value is 757.6 µs. The current reaches a steady state after approximately 1.75 ms. No distinct overshoot of the current is present, as the curve is overstable. A ripple current between -9.88 and -10.092 A is displayed in fig. 4.3b. This ripple is 2.12% of the -10 A reference value. The ripple is staying constant within sections, and the majority of the ripple is thereby lower than the 2.12% would suggest.

For the PI output of the primary bridge, the values in fig. 4.3c show a negative time delay. This delay is converted to a positive value before it is sent to the phase shift block, as it is impossible to delay with a negative time. The transient response of the signal drops down immediately before it curves to a final value of -4.44 µs. This time delay of the generated wave corresponds with a phase shift of 11.1%. The ripple in fig. 4.3d is low and with a constant recurring pattern between -3.998 and -4.402 µs. The signal increases with a slow growth before it drops down and restarts the pattern.

Table 4.4: Battery response parameters while discharging with constant current

Parameter	Current	PI output
SS	-10 A	-4.4 µs
T_R	757.6 µs	425 µs
T_S	1.75 µs	1.25 µs
$\%OS$	0 %	12.5 %
Ripple	2.12 %	0.68 %

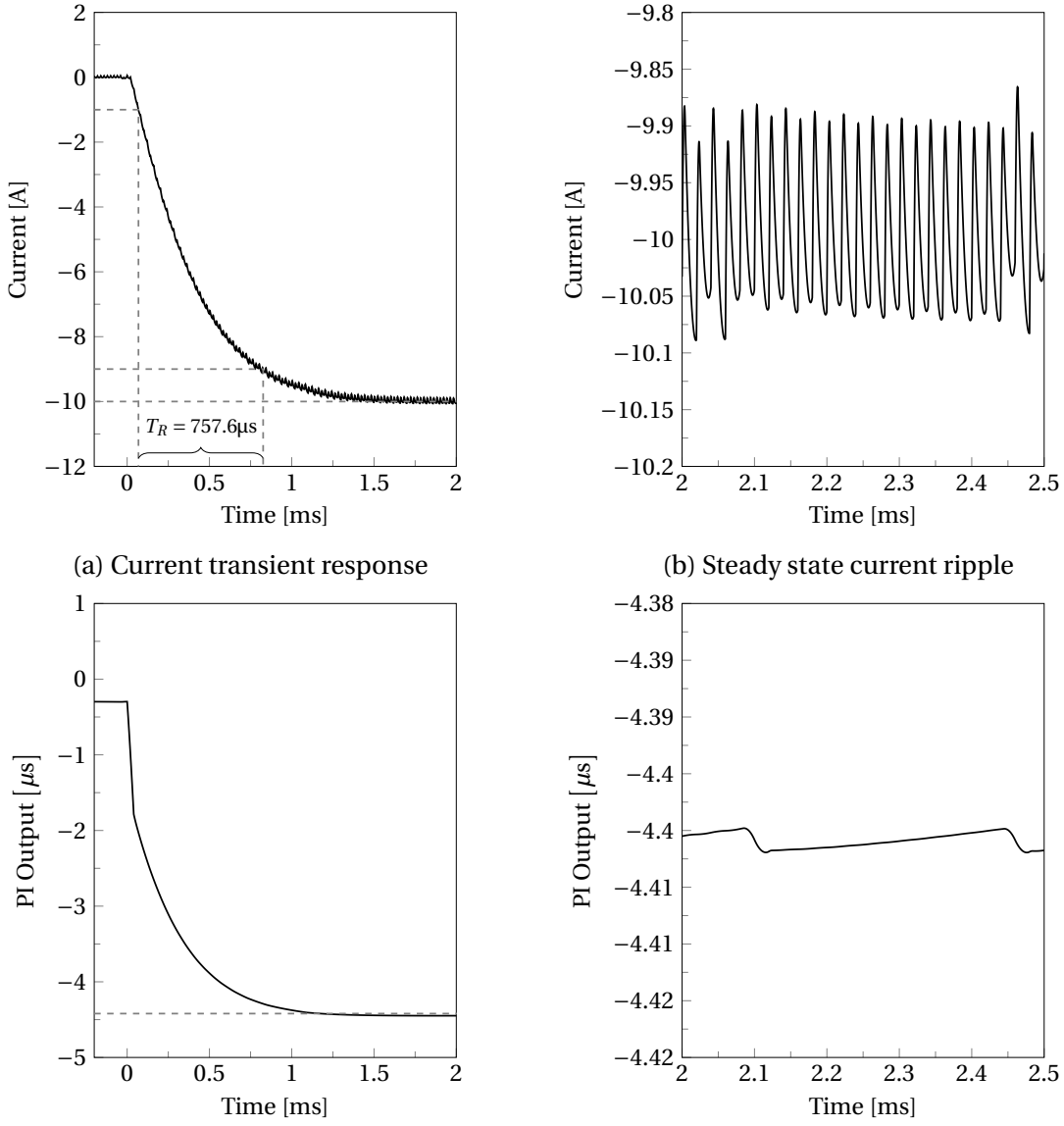

(a) Current transient response

(b) Steady state current ripple

(c) PI output transient response

(d) Steady state PI output

Figure 4.3: Battery current and PI output presented with their transient response and their following steady state ripple with a battery discharging current of 10 A

4.1.2 Powerflow

Figure 4.4 displays the ac square wave voltages and the notable characteristics of the inductor while charging and discharging the battery. The connected battery is at 50% SOC, with a no-load voltage of 184.4 V. In fig. 4.4a, the battery charges with 4 A constant current, and the power flows from the dc bus to the battery. This power flow is achieved by lagging the secondary voltage wave 1.6 µs or 4% in relation to the primary wave. The primary voltage wave V_{ac_1} varies between +342.7 and -342.6 V. The transformer decreases the secondary voltage wave V_{ac_2} to +186.2 and -186.3 V.

Figure 4.4b presents the current and voltage over the leakage inductor. Both the voltage and current indicates to be in four possible states. As both the ac waves are negative, the voltage over the inductor is at -20.5 V. The current decreases at a moderate rate until it reaches -3.68 A. As the primary wave turns positive at 0 µs, the inductor voltage spikes to 651.2 V, and the current increases at a steep rate up to 1.4 A. The length of the voltage spike is dependent on the amount of phase shift applied. After both ac waves become positive, V_L reduces to 20.8 V, while i_L increases with a moderate speed to a peak value of 3.39 A. Next, as the primary wave becomes negative, the inductor voltage rapidly decreases to -651.2 V, similarily the current decreases to -1.3 A. This cycle repeats for every period, with slight variations in voltages and currents.

For the ac waves in fig. 4.4c, the DAB is discharging the battery with -10 A. Since the power flow is from the battery, the secondary wave is leading the primary. This phase shift between the waves has a magnitude of 4.44 µs or 11.1%. The secondary side ac voltage changes between +179.4 and -179.8 V, while the primary side switches between +350.5 and -350.4 V. The voltage and leakage current of the corresponding values are shown in fig. 4.4d. Similarily to fig. 4.4b, the current and voltage are separated in four sections, however as the primary side is lagging, the characteristics are flipped. The relevant currents are -7,-5,8, and 5 A from 0 µs to 40 µs; similarly, the voltage over the inductor varies between -39.4, -635.7, 39.5, and 635,4 V, respectively.

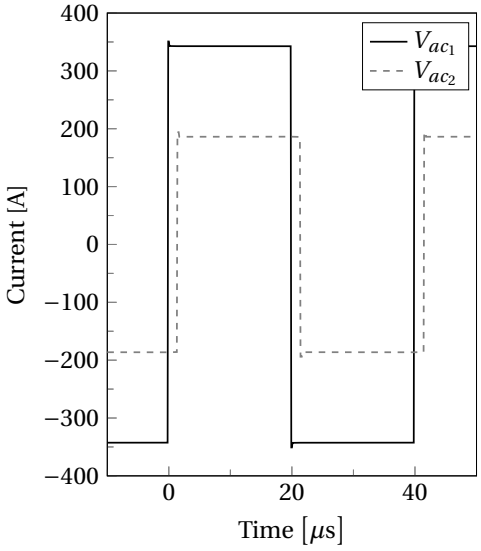

(a) AC voltages, charging

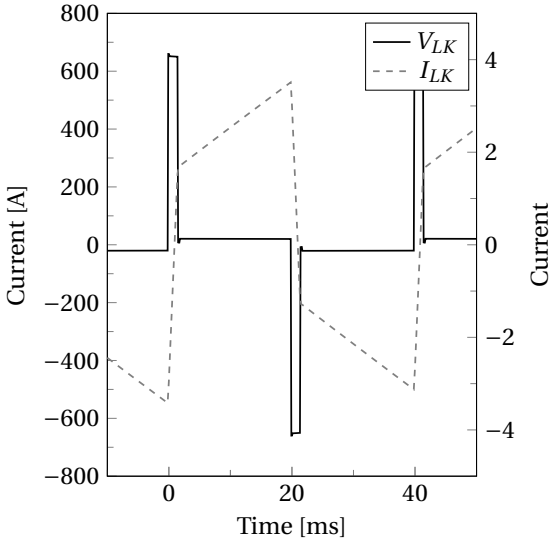

(b) Inductor voltage and current, charging

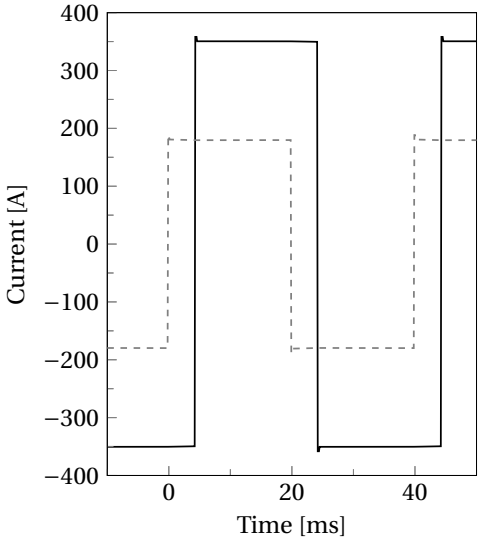

(c) AC voltage, discharging

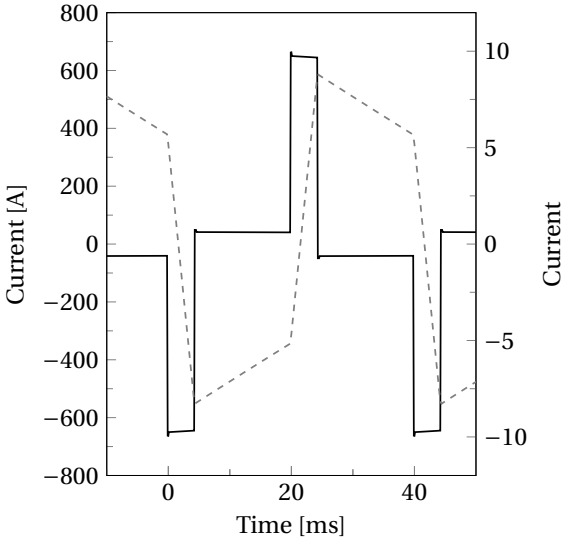

(d) Inductor voltage and current, discharging

Figure 4.4: Primary and secondary ac voltages, presented with the current and voltage over the leakage inductor, while the converter is charging and discharging

The maximum allowable PI output in either direction is limited to 2 µs, which is 25% of the total period. Any increase in phase after this limit will only decrease the output power. Figure 4.5 visualizes this phenomenon by plotting the power output as a function of the phase shift. The simulated output power is plotted in fig. 4.5a with the phase shift represented as % of the total period. The output power is shown as a sine wave by increasing the phase shift from -50 to +50% at a steady rate. From the figure, the maximum and minimum output power is delivered at 25 and -25%, respectively. The charging and discharging phase shift of 4% and -11.1% are also shown with the dashed lines. The calculated output power is plotted from eq. (2.1) with the phase shift represented in radians.

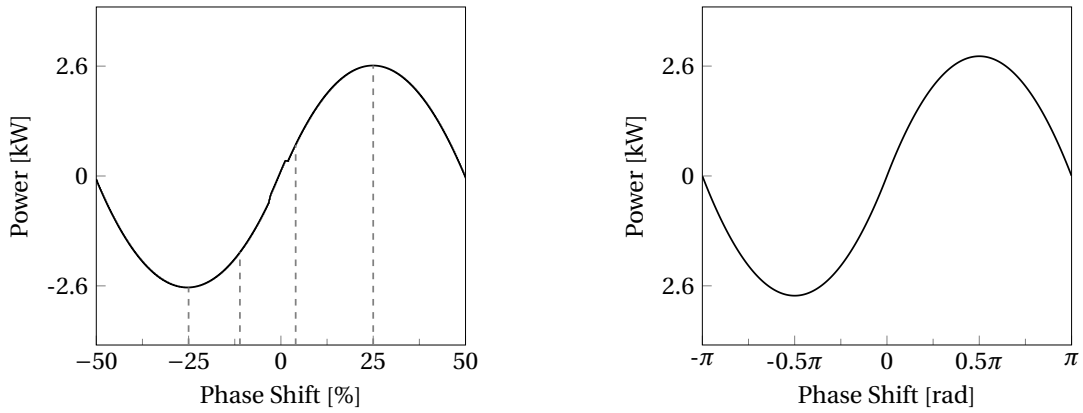

(a) Simulated with %

(b) Calculated with rad

Figure 4.5: Simulated and calculated output power between maximum and minimum phase shift

The current, power, efficiency, and phase shift of critical values are listed in table. 4.5. With a high phase shift between the bridges, the efficiency of the model decreases. The same statement holds for low values. The highest value of efficiency occurs at approximately 7 to 8% phase shift. With a 4% phase shift, the DAB delivers 773 W to the battery with an efficiency of 98.82%; the total loss is therefore 11 W. Current drawn from the dc bus is here 2.28 A. A phase shift of -11.1%, delivers 1800 W to the battery with an efficiency of 98.63% and a loss of 18 W. The current from the dc bus is -5.09 A.

Table 4.5: Power flow parameters from the converter simulation model

Input Current [A]	Input Power [W]	Output Current [A]	Output Power [W]	Efficiency [%]	Phase Shift [%]
-7.21	-2539	-14.67	-2628	97.00	-25
-5.09	-1782	-10	-1800	98.63	-11.1
2.28	784	4.15	773	98.82	4
8.05	2712	13.67	2600	97.09	25

4.1.3 Soft switching

Decreasing the switching losses is an essential part when applying high switching frequency. Soft switching in the DAB is achieved with ZVS due to the dead time between the gate signals, set to 200 ns. For determining the possibility of soft switching, actual voltage and current characteristics are analyzed. Figure 4.6 presents the drain-source voltage(V_{DS}), gate signal(G_S), and switching current(I_{sw}) over the S_1 MOSFET while charging and discharging at the switching time.

In fig. 4.6a, MOSFET S_1 is turned on while charging, as the power flow from the primary bridge to the secondary bridge. The voltage and current drop instantly before the gate signal goes high, as the output capacitance of the MOSFET discharges. After switching, the current increases at a quick rate. In fig. 4.6b the MOSFET is turned off with zero drain-source voltage. Immediately after switching, the voltage rises, and the current flow is cut. In fig. 4.6c, MOSFET S_1 is turned on while power flow is reverter, thereby discharging. The drain-source voltage drops to zero, and the current decreases as the converter discharges immediately before the MOSFET is switched on. In fig. 4.6d the current starts to increase as the capacitance charges, at the height of the current, the drain-source voltage increases. The gate signal drops shortly before the voltage increases, and ZVS is achieved.

From fig. 4.7 the drain-source voltage, gate-source voltage, and switching current are recorded over the S_5 MOSFET on the secondary bridge. In fig. 4.7a the S_5 MOSFET is switched on while the converter is charging. The drain-source voltage decreases to zero, while the current decreases from zero immediately before the gate signal is initialized. In fig. 4.7b the current increases as the capacitance charge and the drain-source voltage increases. The gate signal increases while the voltage is zero. In fig. 4.7c the converter is discharging, and power is flowing from the battery to the dc-bus. The drain-source voltage and current drop instantly before the MOSFET are turned on. The current then increases at a fast rate. In fig. 4.7d the MOSFET is turned off before the drain-source voltage increases and the switching current is cut off. For every semiconductor switch, soft switching is achieved through ZVS while either charging or discharging.

Primary bridge

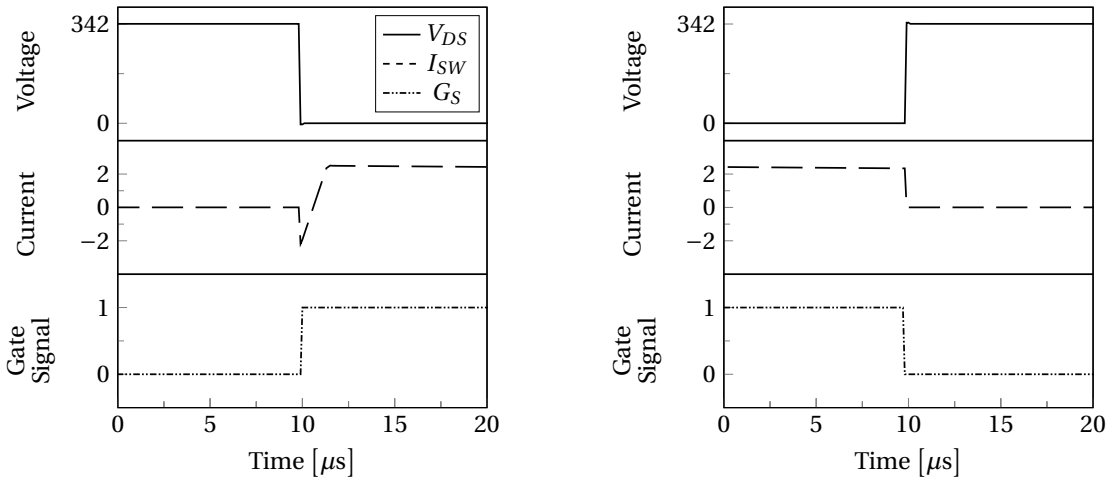

(a) ON switching while charging

(b) OFF switching while charging

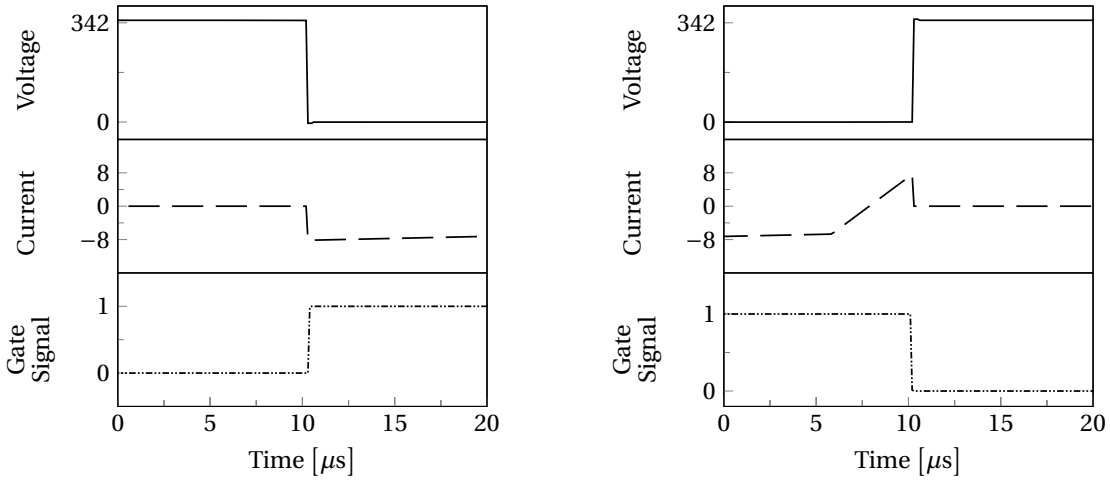

(c) ON switching while discharging

(d) OFF switching while discharging

Figure 4.6: Characteristic of the drain-source and gate-source voltage presented with the switching current over the S1 MOSFET, transitioning between the ON- and OFF-state while charging and discharging.

Secondary bridge

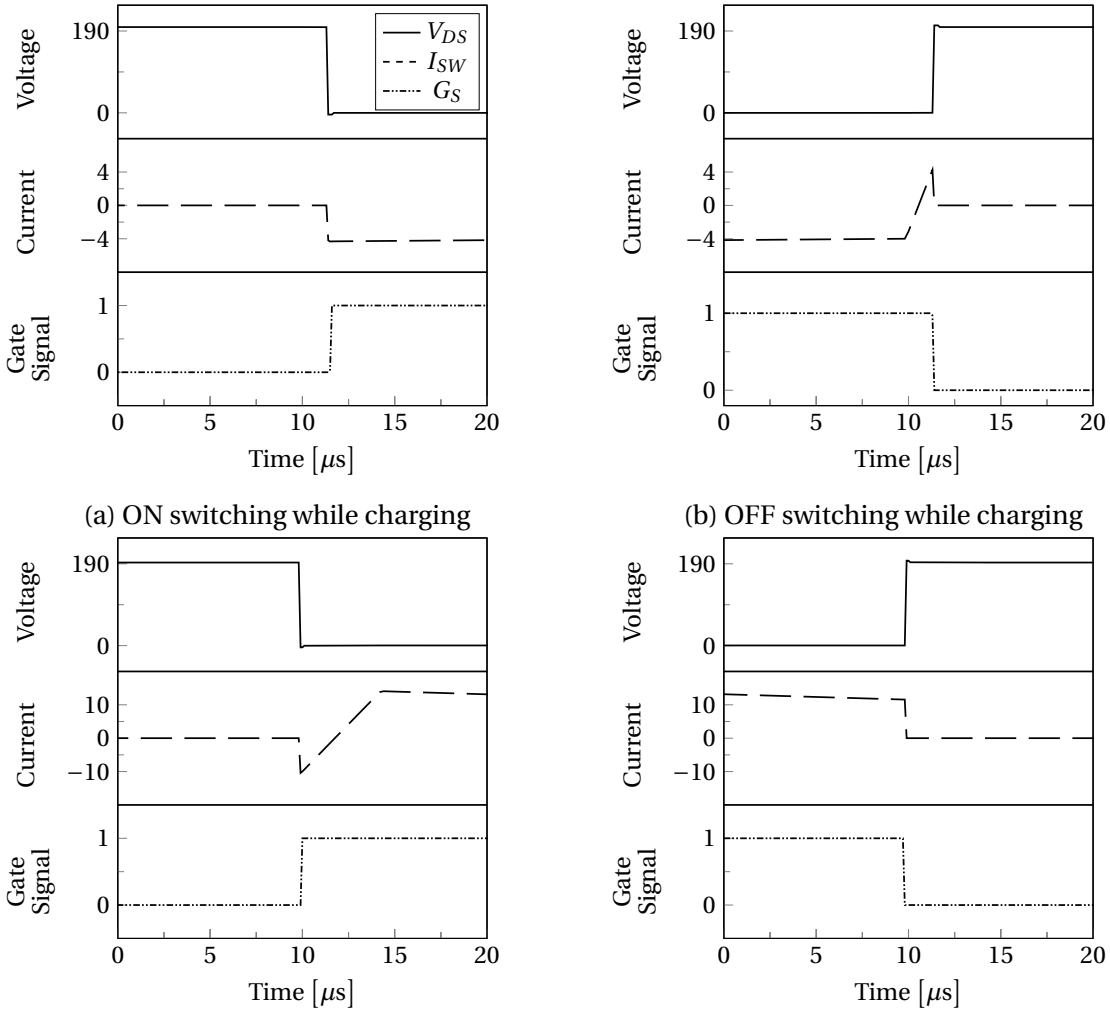

(a) ON switching while charging

(b) OFF switching while charging

(c) ON switching while discharging

(d) OFF switching while discharging

Figure 4.7: Characteristic of the drain-source and gate-source voltage presented with the switching current over the S5 MOSFET, transitioning between the ON- and OFF-state while charging and discharging.

4.2 Physical battery

Measurements from the lab test setup described in section 3.5 are presented and compared with the simplified battery simulation from section 3.2.2. The objective is to display the transient response under different loads, and is shown in fig. 4.8. The current step is initiated at time zero, and current levels of 2,4, 6, and 8 A are chosen for each step. Figure 4.8a, show the current response of the physical battery. The rise time, settling time, overshoot, and undershoot of the responses are shown in table 4.6. The battery voltage decreases as the load is connected; this is shown in fig. 4.8b. The same test is performed on a simplified simulated model. The current response in fig. 4.8c shows an instant increase in current, with a slight overshoot. Similarly the voltage response in fig. 4.8d displays a rapid decrease.

Table 4.6: Battery current response from lab test setup

Type	**2 A**	**4 A**	**6 A**	**8 A**
RiseTime (µs)	11.313	9.5400	8.8175	8.4550
SettlingTime (µs)	21.345	17.980	17.820	24.640
Overshoot (%)	4.0330	4.0164	3.3649	1.7572

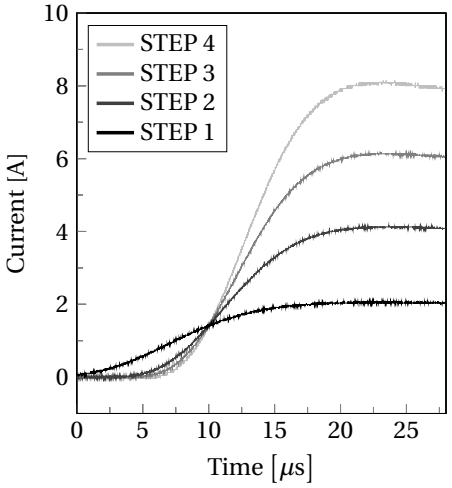

(a) Physical transient current response

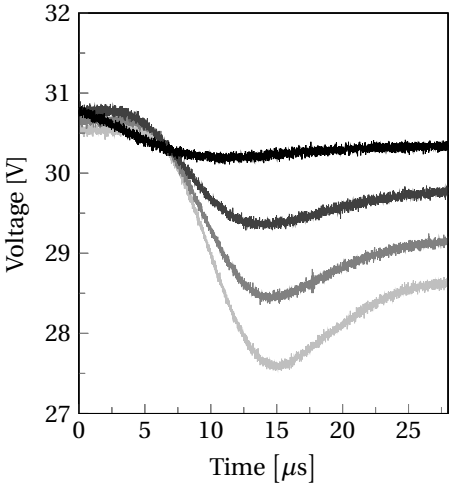

(b) Physical transient voltage response

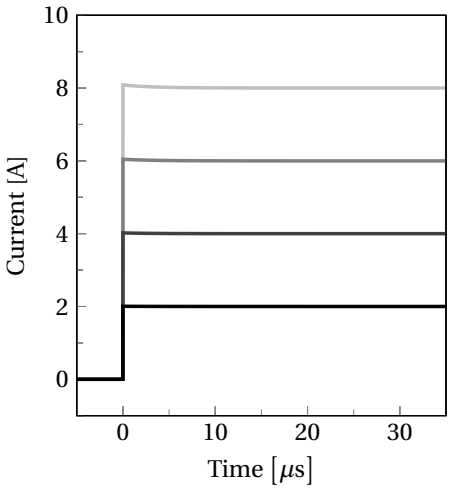

(c) Simulated transient current response

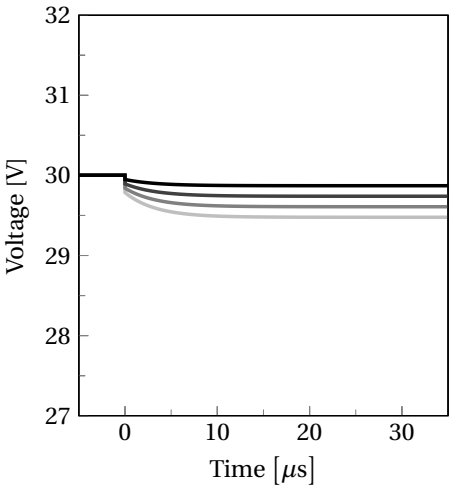

(d) Simulated transient voltage response

Figure 4.8: Voltage and current response from battery prototype pack and battery simulation with current steps of 2, 4, 6, an 8 A

5 Discussion

The discussion is divided into two primary parts. Section 5.1 discusses the primary bidirectional dc-dc converter model and is divided into operation in section 5.1.1, power transfer capabilities in section 5.1.2 and soft switching ability in section 5.1.3. The second main discussion is about the battery prototype in section 5.2.

5.1 Converter Simulation Model

The simulation results from chapter 4 have been simulated exclusively in Matlab® /Simulink®. The electrical components used are from within the specialized power system in the Simscape electrical library. For every component library, there will be a compromise between complexity and functionality.

5.1.1 Operation

The isolated bidirectional dc-dc converter simulation model is operated in three modes, excluding the override function. When charging in the constant current and constant voltage mode, the converter operates as a buck converter. Conversely, when running in the discharging mode, the converter operates as a boost converter. For each of these modes, a separate PI controller regulates the phase shift. These controllers are tuned for the specific value and desired characteristic such that an optimal curve is achieved.

From the results in section 4.1, the transient response and steady-state value of the controlled reference value and the PI output are presented individually. The charging with the constant current mode is first presented in fig. 4.1, where a reference current of 4 A is applied at time zero. The PI output is presented in microseconds as it controls the delay of the signal generator. This PI output increases nearly instantaneously compared to the current, and reaches an overshoot of 12.5% before it stabilizes after approximately 2 µs. The characteristic from the PI output is shown in the current curve, as the initial slope is steep and then diminishes, acquiring a rise time of 455 µs and a settling time of approximately 2 µs. The same repeated ripple style in the PI output captured after reaching a steady-state value

is distinctly shown in the current ripple. The peak to peak ripple shows a variation of about 2% of the total reference current of 4 A. An output filter may be applied when a more stable signal with a lower current ripple is required. Similar to the results while charging, the discharging with constant current presented in fig. 4.3 displays the transient response of the current and the PI output. A current reference is set to -10 A, at time zero. The current and PI output response follow each other more closely than when charging. This feature is due to the tuning of the PI regulator, as the current reference is further from zero. Even as the curves' characteristics current and PI output are similar, the current curve lags behind. This time difference is most measurable by comparing the rise time of both curves. The PI output rises about 330 µs faster than the current. There will always be a delay between the output of the PI regulator and the actual change in reference.

The ripple current and PI output show a pattern as the controlled value is held constant. This connection between the PI output ripple and current ripple is shown for the constant current modes as the PI output is stabilized. In these simulations the battery is held at 50% SOC and is either increased or decreased depending on the power flow. The simulated converter model calculates the SOC with coulomb counting. This is the same method applied in the external SOC calculation of the simulated battery model. As every parameter is known, and the environment can be controlled, this calculation method has a high degree of accuracy. However, it is not adaptive and can not self-regulate. The model-based method described in section 2.3.3 would therefore be preferred in a physical system.

The constant voltage mode presented in fig. 4.2 differs from the two constant current modes. This mode will only activate at the end of the charging cycle when the voltage has reached its highest value to achieve top charging. The voltage, current, and time delay are presented in this figure. As the battery voltage reaches 200 V, the mode switches from constant current to constant voltage, and the reference value is set to 200 V. The transition point is shown as a distinct change in form for every signal. The voltage increases at a moderate rate before it stabilizes at the upper voltage limit. Conversely, the current changes from a stable level to a mild decrease. The ripple value increases as the converter changes to constant voltage mode; this change is also noticeable in the PI output. As the phase shift is constantly decreasing, the PI controller struggles to decrease the signal without increasing the ripple. Instead of controlling the phase shift directly with a voltage reference, the ripple may be decreased by controlling the current reference based on the voltage reference by another PI controller. This method, however is not applied in the control section due to early design choices. Both the constant current modes showed a repetitive ripple pattern in both the current and PI output. Due to the decreasing PI output value, no repetition in the ripple is shown in the voltage, current, or PI output.

The simulated converter model shows satisfactory response while charging and discharging, but for faster transient response and a more stable steady-state output, modular predictive control(MPC) may be used. With MPC, the model response is predicted in advance, and control actions are adjusted to achieve the desired characteristic. However, this control method is more advanced than the implemented PI controller and requires more processing power. The control method is thereby a compromise between functionality, simplicity, and efficiency.

5.1.2 Power Transfer Capabilities

The power flow from the simulated converter with relevant ac components is presented in section 4.1.2. The simulated and calculated output power is plotted as a function of phase shift in fig. 4.5. The simulated output power is plotted in fig. 4.5a, the phase shift is represented as a percentage of the total period. The figure shows a sine curve with a minor imperfection around 0% phase shift. This irregularity is due to limitations of the simulation as the phase shift changes polarity, the applied PI controllers change. In addition, as the phase shift is constantly increased from -50, more stress is introduced to the system. The power capability while charging and discharging are presented in the table. Higher power output values are achieved with higher values of phase shift, but the efficiency will be low. The highest efficiency level will be between 4% and 11% at approximately 7%. Therefore, a high phase shift will increase the overall losses in the model. Likewise, a too low value will increase the overall losses.

The calculated output power from eq. (2.1) is plotted in fig. 4.5b, the phase shift is represented as π radian, where 2π is a complete period. The results are compared for the simulated and calculated power outputs, in fig. 5.1. The curves show similar values for low phase shift values, but with larger amounts, the difference increases. The theoretically calculated power curve depends on an ideal converter and shows a slightly higher power output than the simulated. This difference is then exaggerated at the peak value of the phase shift. The figure also highlights the difference between presenting the phase shift as a percentage and radians. When calculating equations, the phase shift in this thesis is used as π rad, while a percentage or seconds are primarily used while visually presenting the results.

Figure 4.4 presents the simulated ac voltages and inductor characteristics while charging and discharging. The simulated values follow the theoretical characteristic presented in section 2.2. The difference in these currents and voltages is due to the model's phase shift and power flow. With higher values of phase shift, the gap between the primary and secondary square voltage waves is increased. The primary bridge will be leading or lagging depending on the power flow direction of the converter. Similarly, as the phase shift is increased,

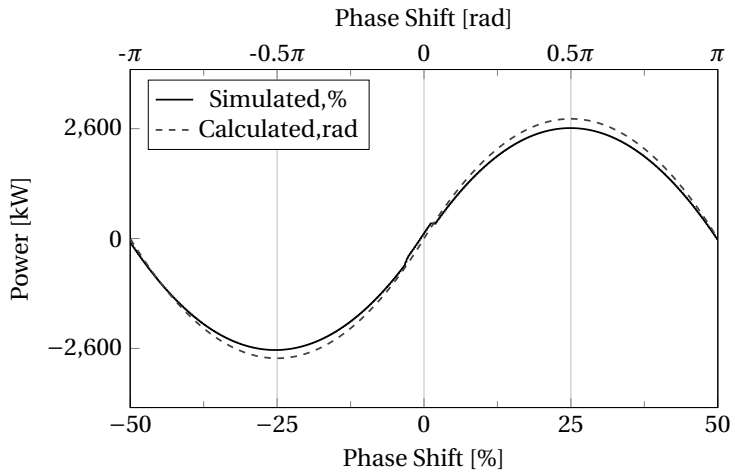

Figure 5.1: Comparison between the simulated and calculated output power as a function of the phase shift presented as percent from fig. 4.5a and as radian from fig. 4.5b

the current peak is increased, but the rate is decreased as the current rises more slowly. The power transition between the bridges is possible due to the galvanic isolated transformer between the two bridges. The simulated transformer is limited as its inductance is close to negligible and has little effect on the simulation. In a practical system, the transformer inductance must be subtracted from the total leakage inductor when selecting the external inductor. The realistic values from the planar transformer described in section 3.1.5 are limited to the winding losses and do not describe the magnetic inductance. In addition, the turn ratio is designed to keep the voltage ratio close to unity during nominal operation. This decreases the losses as soft switching is more easily achieved.

The SPS switching strategy would struggle to perform with the high-efficiency levels, 98.63 and 98.82% as presented in table 4.5 in a physical DAB converter. More efficient and robust switching strategies as described in section 2.2.1 can be used to increase efficiency and the controllability of the converter. TPS will have the most advantageous features compared to SPS, but it may be hard to achieve due to the high level of complexity of this switching strategy. The DPS modulation features improved efficiency and lower losses without increasing the complexity too significantly. This switching strategy allows for a higher degree of controllability as the duty cycle is added as a controllable parameter compared to the SPS, which only controls the phase shift. The circulating current issue with SPS, which directly leads to increased losses, would decrease while simultaneously increasing the soft-switching range.

5.1.3 Soft Switching

The zero-voltage switching ability of the dual active bridge converter is a crucial ability to decrease the switching losses. Without this feature, the switching losses would be too high due to the high frequency and short period. The voltage and current over the semiconductor switch S_1 on the primary bridge and S_5 on the secondary bridge with power flow in both directions are presented in section 4.1.3. As explained in section 2.2.4 the MOSFET should theoretically achieve full ZVS while switching on and pseudo-ZVS while switching off when the power flow is positive towards the semiconductor. However, from the simulation results, ZVS is achieved for every switch during both charging and discharging. This property is due to the unrealistic battery response of the simulation model. As the capacitors discharge, the battery voltage drops instantaneously, and the voltage is zero as the semiconductor switches.

The voltage would drop more gradually in a practical system, and soft switching would be harder to achieve. This ideal switching is one of the leading causes of the high efficiency and low losses in the model. The current characteristic depends on the power flow direction, as shown in fig. 4.6 and fig. 4.7. These figures demonstrate how the characteristic of the switching current is subject to the charge and discharge state of the converter as the power flow changes. Compared to the theoretical characteristic attribute, the current flow is operating as expected, apart from the instant drops.

5.2 Battery Prototype

A prototype of the physical battery system is designed, which can be increased later to the desired voltage level, similar to the simulated converter. The prototype is designed as a 2x4S2P pack with a peak voltage of 33.6 V. To reach 200 V, six of these battery packs must be connected in series. Due to the uniformity of the system, this process is simple to achieve. A simulated model of the battery pack is simulated in Simulink/Matlab. The results from the physical laboratory and simulations are presented in fig. 4.8. The battery prototype is tested with a 9500-08 T programmable load described in section 3.5. The load is stepped at time zero to achieve 2, 4, 6 and 8 A discharge current from the battery. The 2 A step shown in fig. 4.8a displays a distinct response compared to the 4, 6 and 8 A step, as it increases earlier with a flatter slope. This characteristic is also visible with the voltage curves in fig. 4.8b, as the voltage decreases ahead of the other. This irregularity may be due to changes within the programmable load for high current values, as the 4 A step shows signs of a similar curve to the 2 A step. If a larger load had been available, the discharge current responses could be more comparable since the 8 A is the maximum allowable current through the programmable load.

The simulated battery is designed with the same setup and parameters as the physical prototype, and the same load test is performed. The current step shown in fig. 4.8c displays an instant response compared to the physical model. Similarly, the voltage from the simulated battery shows a rapid decrease, which decreases significantly less than the physical battery. This comparison between the physical battery and the Simulink model showcase the limitations of the simulated battery model. This model employs the charge and discharge characteristic described in section 2.3.1, where the voltage variation is low in the nominal area and increases quickly in the exponential area and depleted area. However, the model struggles with realistic current and voltage responses.

A battery simulation with a realistic response characteristic would benefit the bidirectional dc-dc converter in validating the converter simulations to a higher degree. The battery response is critical when an unstable load is required to be kept at a steady level. A practical application for this requirement is vehicle-to-grid applications, as mentioned in section 1.1. For other applications where the battery response will not be quick enough, a supercapacitor is commonly applied together with the battery. The difference in transient response time between a supercapacitor and battery for stabilization application in a micro-grid is the primary aspiration for the paper submitted for review for the IEEE ICECCME 2021 conference and the abstract approved for the IEEE SEST 2021 conference.

6 Conclusion

This thesis presents the functionality and operation of an isolated bidirectional dc-dc converter for use with electric vehicle applications. By utilizing Matlab®/Simulink®a simulated converter model with dual active bridge topology is implemented between the grid and battery model. A control system is implemented, and phase shift modulation is applied for controlling the bidirectional power flow between the grid and battery. The battery prototype pack is designed and built, while a battery management system for cell balancing is implemented. The battery prototype system is compared to the simulated battery model from Matlab®/Simulink®.

The results from the converter simulation show a fast and controlled power flow between the battery and grid as the battery model charges and discharges accordingly to the lithium-ion battery characteristics. The battery prototype and the simulated battery model results showcase the limitations of the simulated battery model as the transient response increases as an immediate step compared to the physical battery.

Future Work

The simulated control system is functional but can be improved with more advanced controllers, furthermore the practical aspects of the converter can be increased.

- Include model predictive control in the control section for the converter simulation.
- Implement SOC calculations with self regulation.
- Implement DPS to the phase modulation.
- Model verification through a physical design of a DAB converter.
- Increase battery voltage by coupling extra battery packs.
- Design a battery simulation model with realistic response characteristics.

References

[1] (2021). "Norwegian EV market," [Online]. Available: https://elbil.no/english/norwegian-ev-market/ (visited on 01/14/2021).

[2] S. Inoue and H. Akagi, "A Bidirectional DC–DC Converter for an Energy Storage System With Galvanic Isolation," *IEEE Transactions on Power Electronics*, vol. 22, no. 6, pp. 2299–2306, Nov. 2007, ISSN: 0885-8993. DOI: 10.1109/TPEL.2007.909248. [Online]. Available: http://ieeexplore.ieee.org/document/4371545/ (visited on 03/03/2021).

[3] F. Peng, H. Li, G.-J. Su, and J. Lawler, "A New ZVS Bidirectional DC–DC Converter for Fuel Cell and Battery Application," *IEEE Transactions on Power Electronics*, vol. 19, no. 1, pp. 54–65, Jan. 2004, ISSN: 0885-8993. DOI: 10.1109/TPEL.2003.820550. [Online]. Available: http://ieeexplore.ieee.org/document/1262053/ (visited on 05/11/2021).

[4] VNR VJIET, V. Dinesh, and E. Prasad, "Simulation of Dual Active Bridge Converter for Energy Storage System," *International Journal of Engineering Trends and Technology*, vol. 27, no. 2, pp. 79–83, Sep. 25, 2015, ISSN: 22315381. DOI: 10.14445/22315381/IJETT-V27P213. [Online]. Available: http://www.ijettjournal.org/archive/ijett-v27p213 (visited on 05/11/2021).

[5] B. Zhao, Q. Song, W. Liu, and Y. Sun, "Overview of Dual-Active-Bridge Isolated Bidirectional DC–DC Converter for High-Frequency-Link Power-Conversion System," *IEEE Transactions on Power Electronics*, vol. 29, no. 8, pp. 4091–4106, Aug. 2014, ISSN: 0885-8993, 1941-0107. DOI: 10.1109/TPEL.2013.2289913. [Online]. Available: http://ieeexplore.ieee.org/document/6658916/ (visited on 12/01/2020).

[6] S. Inoue and H. Akagi, "A Bidirectional Isolated DC–DC Converter as a Core Circuit of the Next-Generation Medium-Voltage Power Conversion System," *IEEE Transactions on Power Electronics*, vol. 22, no. 2, pp. 535–542, Mar. 2007, ISSN: 0885-8993. DOI: 10.1109/TPEL.2006.889939. [Online]. Available: http://ieeexplore.ieee.org/document/4118307/ (visited on 05/11/2021).

[7] B. Zhao, Q. Yu, and W. Sun, "Extended-Phase-Shift Control of Isolated Bidirectional DC–DC Converter for Power Distribution in Microgrid," *IEEE Transactions on Power*

Electronics, vol. 27, no. 11, pp. 4667–4680, Nov. 2012, ISSN: 0885-8993, 1941-0107. DOI: 10.1109/TPEL.2011.2180928. [Online]. Available: http://ieeexplore.ieee.org/document/6111310/ (visited on 03/03/2021).

[8] F. L. F. Marcelino, H. H. Sathler, T. R. de Oliveira, and P. F. Donoso-Garcia, "Modeling and control of a Dual Active Bridge for energy storage in DC microgrid applications," in *2017 IEEE 8th International Symposium on Power Electronics for Distributed Generation Systems (PEDG)*, Florianopolis, Brazil: IEEE, Apr. 2017, pp. 1–8, ISBN: 978-1-5090-5339-1. DOI: 10.1109/PEDG.2017.7972461. [Online]. Available: http://ieeexplore.ieee.org/document/7972461/ (visited on 02/08/2021).

[9] Hua Bai, C. Mi, and S. Gargies, "The Short-Time-Scale Transient Processes in High-Voltage and High-Power Isolated Bidirectional DC–DC Converters," *IEEE Transactions on Power Electronics*, vol. 23, no. 6, pp. 2648–2656, Nov. 2008, ISSN: 0885-8993, 1941-0107. DOI: 10.1109/TPEL.2008.2005106. [Online]. Available: http://ieeexplore.ieee.org/document/4682718/ (visited on 03/03/2021).

[10] W. Ye, S. Shao, Q. Guo, J. Zhang, and K. Sheng, "A Phase Shift Control of Minimal Circulating Current and ZVS Turn-On for DAB Converter," in *2018 IEEE 2nd International Electrical and Energy Conference (CIEEC)*, Beijing, China: IEEE, Nov. 2018, pp. 682–686, ISBN: 978-1-5386-5392-0. DOI: 10.1109/CIEEC.2018.8745797. [Online]. Available: https://ieeexplore.ieee.org/document/8745797/ (visited on 09/16/2020).

[11] J. Huang, Y. Wang, Z. Li, and W. Lei, "Unified Triple-Phase-Shift Control to Minimize Current Stress and Achieve Full Soft-Switching of Isolated Bidirectional DC–DC Converter," *IEEE TRANSACTIONS ON INDUSTRIAL ELECTRONICS*, vol. 63, no. 7, p. 11, 2016, ISSN: 1557-9948. DOI: 10.1109/TIE.2016.2543182.

[12] R. Barlik, M. Nowak, and P. Grzejszczak, "Power transfer analysis in a single phase dual active bridge," *Bulletin of the Polish Academy of Sciences: Technical Sciences*, vol. 61, no. 4, pp. 809–828, Dec. 1, 2013, ISSN: 0239-7528. DOI: 10.2478/bpasts-2013-0088. [Online]. Available: http://journals.pan.pl/dlibra/publication/97223/edition/83813/content (visited on 05/11/2021).

[13] Y. H. Abraham, H. Wen, W. Xiao, and V. Khadkikar, "Estimating power losses in Dual Active Bridge DC-DC converter," in *2011 2nd International Conference on Electric Power and Energy Conversion Systems (EPECS)*, Sharjah, United Arab Emirates: IEEE, Nov. 2011, pp. 1–5, ISBN: 978-1-4577-0806-0 978-1-4577-0804-6 978-1-4577-0805-3. DOI: 10.1109/EPECS.2011.6126790. [Online]. Available: http://ieeexplore.ieee.org/document/6126790/ (visited on 03/22/2021).

[14] K. Zhang, Z. Shan, and J. Jatskevich, "Estimating switching loss and core loss in dual active bridge DC-DC converters," in *2015 IEEE 16th Workshop on Control and Modeling for Power Electronics (COMPEL)*, Vancouver, BC, Canada: IEEE, Jul. 2015, pp. 1–6,

ISBN: 978-1-4673-6847-6. DOI: 10.1109/COMPEL.2015.7236501. [Online]. Available: http://ieeexplore.ieee.org/document/7236501/ (visited on 04/07/2021).

[15] Hua Bai and C. Mi, "Eliminate Reactive Power and Increase System Efficiency of Isolated Bidirectional Dual-Active-Bridge DC–DC Converters Using Novel Dual-Phase-Shift Control," *IEEE Transactions on Power Electronics*, vol. 23, no. 6, pp. 2905–2914, Nov. 2008, ISSN: 0885-8993, 1941-0107. DOI: 10.1109/TPEL.2008.2005103. [Online]. Available: http://ieeexplore.ieee.org/document/4700286/ (visited on 03/04/2021).

[16] D. Linden and T. B. Reddy, Eds., *Handbook of Batteries*, 3rd ed, ser. McGraw-Hill Handbooks. New York: McGraw-Hill, 2002, 1 p., ISBN: 978-0-07-135978-8.

[17] X. Hu, C. Zou, C. Zhang, and Y. Li, "Technological Developments in Batteries: A Survey of Principal Roles, Types, and Management Needs," *IEEE Power and Energy Magazine*, vol. 15, no. 5, pp. 20–31, Sep. 2017, ISSN: 1540-7977. DOI: 10.1109/MPE.2017.2708812. [Online]. Available: http://ieeexplore.ieee.org/document/8011541/ (visited on 03/08/2021).

[18] D. Ali, S. Mukhopadhyay, and H. Rehman, "A novel adaptive technique for Li-ion battery model parameters estimation," in *2016 IEEE National Aerospace and Electronics Conference (NAECON) and Ohio Innovation Summit (OIS)*, Dayton, OH, USA: IEEE, Jul. 2016, pp. 23–26, ISBN: 978-1-5090-3441-3. DOI: 10.1109/NAECON.2016.7856769. [Online]. Available: http://ieeexplore.ieee.org/document/7856769/ (visited on 11/09/2020).

[19] S. Ebrahimi, M. Taghavi, F. Tahami, and H. Oraee, "A single-phase integrated bidirectional plug-in hybrid electric vehicle battery charger," in *IECON 2014 - 40th Annual Conference of the IEEE Industrial Electronics Society*, Dallas, TX: IEEE, Oct. 2014, pp. 1137–1142, ISBN: 978-1-4799-4032-5. DOI: 10.1109/IECON.2014.7048645. [Online]. Available: https://ieeexplore.ieee.org/document/7048645/ (visited on 01/11/2021).

[20] S. A. Gorji, H. G. Sahebi, M. Ektesabi, and A. B. Rad, "Topologies and Control Schemes of Bidirectional DC–DC Power Converters: An Overview," *IEEE Access*, vol. 7, pp. 117 997–118 019, 2019, ISSN: 2169-3536. DOI: 10.1109/ACCESS.2019.2937239. [Online]. Available: https://ieeexplore.ieee.org/document/8811451/ (visited on 07/21/2020).

[21] H. Matsuo and F. Kurokawa, "New Solar Cell Power Supply System Using a Boost Type Bidirectinal DC-DC Converter," *IEEE Transactions on Industrial Electronics*, vol. IE-31, no. 1, pp. 51–55, Feb. 1984, ISSN: 0278-0046. DOI: 10.1109/TIE.1984.350020. [Online]. Available: https://ieeexplore.ieee.org/document/4158492 (visited on 03/17/2021).

[22] I.-D. Kim, S.-H. Paeng, J.-W. Ahn, E.-C. Nho, and J.-S. Ko, "New Bidirectional ZVS PWM Sepic/Zeta DC-DC Converter," in *2007 IEEE International Symposium on Industrial Electronics*, Vigo, Spain: IEEE, Jun. 2007, pp. 555–560, ISBN: 978-1-4244-0754-5 978-1-4244-0755-2. DOI: 10.1109/ISIE.2007.4374656. [Online]. Available: http://ieeexplore.ieee.org/document/4374656/ (visited on 03/17/2021).

[23] M. N. M. Haque, M. Naeem-Ur-Rahman, S. C. Sarkar, M. S. Miah, I. Ahammad, and M. A. Islam, "Design and simulation of a forcible buck-boost controlling solar powered DC motor," in *2017 IEEE International Conference on Power, Control, Signals and Instrumentation Engineering (ICPCSI)*, Chennai: IEEE, Sep. 2017, pp. 131–136, ISBN: 978-1-5386-0813-5 978-1-5386-0814-2. DOI: 10.1109/ICPCSI.2017.8391958. [Online]. Available: https://ieeexplore.ieee.org/document/8391958/ (visited on 05/11/2021).

[24] K. A. Chinmaya and G. K. Singh, "A Plug - in Electric Vehicle (PEV) with Compact Bidirectional CuK Converter and Sturdier Induction Motor Drive," in *IECON 2018 - 44th Annual Conference of the IEEE Industrial Electronics Society*, Washington, DC: IEEE, Oct. 2018, pp. 937–942, ISBN: 978-1-5090-6684-1. DOI: 10.1109/IECON.2018.8595405. [Online]. Available: https://ieeexplore.ieee.org/document/8595405/ (visited on 03/18/2021).

[25] I. I. Rahman, D. C. Riawan, and M. Ashari, "Design and Implementation of DC-DC Bidirectional Cuk Converter with Average Current Mode Control for Lead Acid Battery Testing," in *2019 International Seminar on Intelligent Technology and Its Applications (ISITIA)*, Surabaya, Indonesia: IEEE, Aug. 2019, pp. 183–188, ISBN: 978-1-72813-749-0. DOI: 10.1109/ISITIA.2019.8937200. [Online]. Available: https://ieeexplore.ieee.org/document/8937200/ (visited on 03/18/2021).

[26] O. Garcia, P. Zumel, A. de Castro, and A. Cobos, "Automotive DC-DC bidirectional converter made with many interleaved buck stages," *IEEE Transactions on Power Electronics*, vol. 21, no. 3, pp. 578–586, May 2006, ISSN: 0885-8993. DOI: 10.1109/TPEL.2006.872379. [Online]. Available: http://ieeexplore.ieee.org/document/1628997/ (visited on 01/15/2021).

[27] F. Caricchi, F. Crescimbini, G. Noia, and D. Pirolo, "Experimental study of a bidirectional DC-DC converter for the DC link voltage control and the regenerative braking in PM motor drives devoted to electrical vehicles," in *Proceedings of 1994 IEEE Applied Power Electronics Conference and Exposition - ASPEC'94*, Orlando, FL, USA: IEEE, 1994, pp. 381–386, ISBN: 978-0-7803-1456-6. DOI: 10.1109/APEC.1994.316373. [Online]. Available: http://ieeexplore.ieee.org/document/316373/ (visited on 11/27/2020).

[28] M. C. Taneri, N. Genc, and A. Mamizadeh, "Analyzing and Comparing of Variable and Constant Switching Frequency Flyback DC-DC Converter," in *2019 4th International Conference on Power Electronics and Their Applications (ICPEA)*, Elazig, Turkey: IEEE, Sep. 2019, pp. 1–5, ISBN: 978-1-72812-726-2. DOI: 10.1109/ICPEA1.2019.8911196. [Online]. Available: https://ieeexplore.ieee.org/document/8911196/ (visited on 01/18/2021).

[29] A. Aboulnaga and A. Emadi, "Performance evaluation of the isolated bidirectional Cuk converter with integrated magnetics," in *2004 IEEE 35th Annual Power Electronics Specialists Conference (IEEE Cat. No.04CH37551)*, Aachen, Germany: IEEE, 2004, pp. 1557–1562, ISBN: 978-0-7803-8399-9. DOI: 10.1109/PESC.2004.1355657. [Online]. Available: http://ieeexplore.ieee.org/document/1355657/ (visited on 01/18/2021).

[30] E. Hiraki, K. Hirao, T. Tanaka, and T. Mishima, "A push-pull converter based bidirectional DC-DC interface for energy storage systems," *IEEE Transactions on Transportation Electrification*, vol. 1, no. 1, p. 10, Mar. 2017. [Online]. Available: https://ieeexplore.ieee.org/document/5279041 (visited on 01/19/2021).

[31] P. He and A. Khaligh, "Comprehensive Analyses and Comparison of 1 kW Isolated DC–DC Converters for Bidirectional EV Charging Systems," *IEEE Transactions on Transportation Electrification*, vol. 3, no. 1, pp. 147–156, Mar. 2017, ISSN: 2332-7782. DOI: 10.1109/TTE.2016.2630927. [Online]. Available: http://ieeexplore.ieee.org/document/7748600/ (visited on 01/19/2021).

[32] M. Tissieres, I. Askarian, M. Pahlevani, A. Rotzetta, A. Knight, and I. Preda, "A digital robust control scheme for dual Half-Bridge DC-DC converters," in *2018 IEEE Applied Power Electronics Conference and Exposition (APEC)*, San Antonio, TX, USA: IEEE, Mar. 2018, pp. 311–315, ISBN: 978-1-5386-1180-7. DOI: 10.1109/APEC.2018.8341028. [Online]. Available: http://ieeexplore.ieee.org/document/8341028/ (visited on 01/19/2021).

[33] R. De Doncker, D. Divan, and M. Kheraluwala, "A three-phase soft-switched high power density DC/DC converter for high power applications," in *Conference Record of the 1988 IEEE Industry Applications Society Annual Meeting*, Pittsburgh, PA, USA: IEEE, 1988, pp. 796–805. DOI: 10.1109/IAS.1988.25153. [Online]. Available: http://ieeexplore.ieee.org/document/25153/ (visited on 11/26/2020).

[34] K. George, "Design and Control of a Bidirectional Dual Active Bridge DC-DC Converter to Interface Solar, Battery Storage, and Grid-Tied Inverters," Dec. 2015. [Online]. Available: https://scholarworks.uark.edu/cgi/viewcontent.cgi?article=1043&context=eleguht (visited on 01/19/2021).

[35] F. Krismer and J. Kolar, "Accurate Power Loss Model Derivation of a High-Current Dual Active Bridge Converter for an Automotive Application," *IEEE Transactions on Indus-*

trial Electronics, vol. 57, no. 3, pp. 881–891, Mar. 2010, ISSN: 0278-0046. DOI: 10.1109/TIE.2009.2025284. [Online]. Available: http://ieeexplore.ieee.org/document/5075552/ (visited on 09/10/2020).

[36] S. Inoue and H. Akagi, "A Bidirectional Isolated DC–DC Converter as a Core Circuit of the Next-Generation Medium-Voltage Power Conversion System," *IEEE Transactions on Power Electronics*, vol. 22, no. 2, pp. 535–542, Mar. 2007, ISSN: 0885-8993. DOI: 10.1109/TPEL.2006.889939. [Online]. Available: http://ieeexplore.ieee.org/document/4118307/ (visited on 03/03/2021).

[37] D. Costinett, D. Maksimovic, and R. Zane, "Design and Control for High Efficiency in High Step-Down Dual Active Bridge Converters Operating at High Switching Frequency," *IEEE Transactions on Power Electronics*, vol. 28, no. 8, pp. 3931–3940, Aug. 2013, ISSN: 0885-8993, 1941-0107. DOI: 10.1109/TPEL.2012.2228237. [Online]. Available: http://ieeexplore.ieee.org/document/6357323/ (visited on 03/03/2021).

[38] G. D. Demetriades and H.-P. Nee, "Characterization of the Dual-Active Bridge topology for high-power applications employing a duty-cycle modulation," in *2008 IEEE Power Electronics Specialists Conference*, Rhodes, Greece: IEEE, Jun. 2008, pp. 2791–2798, ISBN: 978-1-4244-1667-7. DOI: 10.1109/PESC.2008.4592368. [Online]. Available: http://ieeexplore.ieee.org/document/4592368/ (visited on 03/03/2021).

[39] G. G. Oggier, G. O. Garcia, and A. R. Oliva, "Modulation strategy to operate the dual active bridge DC-DC converter under soft switching in the whole operating range," *IEEE Transactions on Power Electronics*, vol. 26, no. 4, pp. 1228–1236, Apr. 2011, ISSN: 0885-8993, 1941-0107. DOI: 10.1109/TPEL.2010.2072966. [Online]. Available: http://ieeexplore.ieee.org/document/5580124/ (visited on 03/03/2021).

[40] G. G. Oggier, G. O. GarcÍa, and A. R. Oliva, "Switching Control Strategy to Minimize Dual Active Bridge Converter Losses," *IEEE Transactions on Power Electronics*, vol. 24, no. 7, pp. 1826–1838, Jul. 2009, ISSN: 0885-8993. DOI: 10.1109/TPEL.2009.2020902. [Online]. Available: http://ieeexplore.ieee.org/document/5185352/ (visited on 03/03/2021).

[41] B. Zhao, Q. Song, and W. Liu, "Power Characterization of Isolated Bidirectional Dual-Active-Bridge DC–DC Converter With Dual-Phase-Shift Control," *IEEE Transactions on Power Electronics*, vol. 27, no. 9, pp. 4172–4176, Sep. 2012, ISSN: 0885-8993, 1941-0107. DOI: 10.1109/TPEL.2012.2189586. [Online]. Available: http://ieeexplore.ieee.org/document/6161654/ (visited on 03/03/2021).

[42] B. Zhao and Q. Song, "Efficiency Characterization and Optimization of Isolated Bidirectional DC–DC Converter Based on Dual-Phase-Shift Control for DC Distribution Application," *IEEE Transactions on Power Electronics*, vol. 28, no. 4, pp. 1711–1727, Apr.

2013, ISSN: 0885-8993, 1941-0107. DOI: 10.1109/TPEL.2012.2210563. [Online]. Available: http://ieeexplore.ieee.org/document/6252062/ (visited on 03/04/2021).

[43] D. Qin, Q. Sun, D. Ma, and J. Sun, "Model Predictive control of dual-active-bridge based fast battery charger for plug-in hybrid electric vehicle in the future grid," in *2019 IEEE Innovative Smart Grid Technologies - Asia (ISGT Asia)*, Chengdu, China: IEEE, May 2019, pp. 2162–2166, ISBN: 978-1-72813-520-5. DOI: 10.1109/ISGT-Asia.2019.8881457. [Online]. Available: https://ieeexplore.ieee.org/document/8881457/ (visited on 03/04/2021).

[44] F. Krismer, "Closed Form Solution for Minimum Conduction Loss Modulation of DAB Converters," *IEEE TRANSACTIONS ON POWER ELECTRONICS*, vol. 27, no. 1, p. 15, 2012, ISSN: 1941-0107. DOI: 10.1109/TPEL.2011.2157976.

[45] F. Krismer and J. W. Kolar, "Efficiency-Optimized High-Current Dual Active Bridge Converter for Automotive Applications," *IEEE Transactions on Industrial Electronics*, vol. 59, no. 7, pp. 2745–2760, Jul. 2012, ISSN: 0278-0046, 1557-9948. DOI: 10.1109/TIE.2011.2112312. [Online]. Available: http://ieeexplore.ieee.org/document/5710417/ (visited on 03/04/2021).

[46] Y. Du and A. Q. Huang, "Modulation Technique to Reverse Power Flow for the Isolated Series Resonant DC–DC Converter With Clamped Capacitor Voltage," *IEEE TRANSACTIONS ON INDUSTRIAL ELECTRONICS*, vol. 59, no. 12, p. 12, 2012, ISSN: 1557-9948. DOI: 10.1109/TIE.2011.2175669.

[47] T. Instruments, "Bi-Directional, Dual Active Bridge Reference Design for Level 3 Electric Vehicle," Jan. 2019.

[48] T. Al, "Electric Vehicle Charger For Future DC Grids," M.S. thesis, TU DELFT, Jul. 2020. [Online]. Available: http://resolver.tudelft.nl/uuid:a8ba9621-ee53-42ca-bb7c-b148eddf078c (visited on 03/04/2021).

[49] S. Helland, "Evaluation of a Medium-Voltage High-Power Bidirectional Dual Active Bridge DC/DC Converter for Marine Applications," *NTNU*, vol. 1, no. 1, p. 91, Dec. 2017. DOI: http://hdl.handle.net/11250/2446945.

[50] S. Shao, H. Chen, X. Wu, J. Zhang, and K. Sheng, "Circulating Current and ZVS-on of a Dual Active Bridge DC-DC Converter: A Review," *IEEE Access*, vol. 7, pp. 50 561–50 572, 2019, ISSN: 2169-3536. DOI: 10.1109/ACCESS.2019.2911009. [Online]. Available: https://ieeexplore.ieee.org/document/8691441/ (visited on 03/08/2021).

[51] M. Kim, M. Rosekeit, and S.-K. Sul, "A dual-phase-shift control strategy for dual-active-bridge DC-DC converter in wide voltage range," *8th International Conference on Power Electronics - ECCE Asia*, vol. 1, no. 1, p. 8, Jul. 11, ISSN: 2150-6078. DOI: 10.1109/ICPE.2011.5944548.

[52] J. Zhang, F. Zhang, X. Xie, D. Jiao, and Zhaoming Qian, "A novel ZVS DC/DC converter for high power applications," in *APEC. Seventeenth Annual IEEE Applied Power Electronics Conference and Exposition (Cat. No.02CH37335)*, vol. 2, Dallas, TX, USA: IEEE, 2002, pp. 635–640, ISBN: 978-0-7803-7404-1. DOI: 10.1109/APEC.2002.989312. [Online]. Available: http://ieeexplore.ieee.org/document/989312/ (visited on 03/08/2021).

[53] D. Sha, J. Zhang, and Y. Xu, "Improved Boundary Operation for Voltage-Fed Semi-DAB With ZVS Achievement and Nonactive Power Reduction," *IEEE Transactions on Industrial Electronics*, vol. 64, no. 8, pp. 6179–6189, Aug. 2017, ISSN: 0278-0046, 1557-9948. DOI: 10.1109/TIE.2017.2682026. [Online]. Available: http://ieeexplore.ieee.org/document/7878533/ (visited on 03/08/2021).

[54] A. Rodriguez, A. Vazquez, D. G. Lamar, M. M. Hernando, and J. Sebastian, "Different Purpose Design Strategies and Techniques to Improve the Performance of a Dual Active Bridge With Phase-Shift Control," *IEEE Transactions on Power Electronics*, vol. 30, no. 2, pp. 790–804, Feb. 2015, ISSN: 0885-8993, 1941-0107. DOI: 10.1109/TPEL.2014.2309853. [Online]. Available: https://ieeexplore.ieee.org/document/6756995 (visited on 03/08/2021).

[55] F. Krismer, S. Round, and J. Kolar, "Performance Optimization of a High Current Dual Active Bridge with a Wide Operating Voltage Range," in *37th IEEE Power Electronics Specialists Conference*, Jeju, Korea: IEEE, 2006, pp. 1–7, ISBN: 978-0-7803-9716-3. DOI: 10.1109/PESC.2006.1712096. [Online]. Available: http://ieeexplore.ieee.org/document/1712096/ (visited on 03/08/2021).

[56] K. Wu, C. W. de Silva, and W. G. Dunford, "Stability Analysis of Isolated Bidirectional Dual Active Full-Bridge DC–DC Converter With Triple Phase-Shift Control," *IEEE Transactions on Power Electronics*, vol. 27, no. 4, pp. 2007–2017, Apr. 2012, ISSN: 0885-8993, 1941-0107. DOI: 10.1109/TPEL.2011.2167243. [Online]. Available: http://ieeexplore.ieee.org/document/6012531/ (visited on 03/08/2021).

[57] N. Hou, W. Song, and m. wu, "Minimum-Current-Stress Scheme of Dual Active Bridge DC-DC Converter With Unified-phase-shift Control," *IEEE Transactions on Power Electronics*, pp. 1–1, 2016, ISSN: 0885-8993, 1941-0107. DOI: 10.1109/TPEL.2016.2521410. [Online]. Available: http://ieeexplore.ieee.org/document/7390302/ (visited on 03/08/2021).

[58] K. Qian, C. Zhou, M. Allan, and Y. Yuan, "Modeling of Load Demand Due to EV Battery Charging in Distribution Systems," *IEEE Transactions on Power Systems*, vol. 26, no. 2, pp. 802–810, May 2011, ISSN: 0885-8950, 1558-0679. DOI: 10.1109/TPWRS.2010.2057456. [Online]. Available: http://ieeexplore.ieee.org/document/5535237/ (visited on 03/09/2021).

[59] B. Schweighofer, K. Raab, and G. Brasseur, "Modeling of high power automotive batteries by the use of an automated test system," *IEEE Transactions on Instrumentation and Measurement*, vol. 52, no. 4, pp. 1087–1091, Aug. 2003, ISSN: 0018-9456. DOI: 10.1109/TIM.2003.814827. [Online]. Available: http://ieeexplore.ieee.org/document/1232350/ (visited on 03/09/2021).

[60] S. Tewari and N. Mohan, "Value of NAS Energy Storage Toward Integrating Wind: Results From the Wind to Battery Project," *IEEE Transactions on Power Systems*, vol. 28, no. 1, pp. 532–541, Feb. 2013, ISSN: 0885-8950, 1558-0679. DOI: 10.1109/TPWRS.2012.2205278. [Online]. Available: http://ieeexplore.ieee.org/document/6247490/ (visited on 03/09/2021).

[61] T. A. Nguyen, M. L. Crow, and A. C. Elmore, "Optimal Sizing of a Vanadium Redox Battery System for Microgrid Systems," *IEEE Transactions on Sustainable Energy*, vol. 6, no. 3, pp. 729–737, Jul. 2015, ISSN: 1949-3029, 1949-3037. DOI: 10.1109/TSTE.2015.2404780. [Online]. Available: http://ieeexplore.ieee.org/document/7079529/ (visited on 03/09/2021).

[62] A. F. Burke, "Batteries and Ultracapacitors for Electric, Hybrid, and Fuel Cell Vehicles," *Proceedings of the IEEE*, vol. 95, no. 4, pp. 806–820, Apr. 2007, ISSN: 0018-9219. DOI: 10.1109/JPROC.2007.892490. [Online]. Available: http://ieeexplore.ieee.org/document/4168012/ (visited on 03/09/2021).

[63] M. Alhanouti, M. Gießler, T. Blank, and F. Gauterin, "New Electro-Thermal Battery Pack Model of an Electric Vehicle," *Energies*, vol. 9, no. 7, p. 563, Jul. 20, 2016, ISSN: 1996-1073. DOI: 10.3390/en9070563. [Online]. Available: http://www.mdpi.com/1996-1073/9/7/563 (visited on 09/28/2020).

[64] L.-R. Dung, C.-E. Chen, and H.-F. Yuan, "A robust, intelligent CC-CV fast charger for aging lithium batteries," *2016 IEEE 25th International Symposium on Industrial Electronics (ISIE)*, vol. 1, no. 1, p. 6, Jun. 2016, ISSN: 2163-5145. DOI: 10.1109/ISIE.2016.7744901.

[65] K. Murashko, D. Li, D. L. Danilov, P. H. L. Notten, J. Pyrhonen, and J. Jokiniemi, "Determination of Li-Ion Battery Degradation Mechanisms at High C-Rate Charging," in *2019 IEEE Vehicle Power and Propulsion Conference (VPPC)*, Hanoi, Vietnam: IEEE, Oct. 2019, pp. 1–6, ISBN: 978-1-72811-249-7. DOI: 10.1109/VPPC46532.2019.8952302. [Online]. Available: https://ieeexplore.ieee.org/document/8952302/ (visited on 05/12/2021).

[66] J. Rivera-Barrera, N. Muñoz-Galeano, and H. Sarmiento-Maldonado, "SoC Estimation for Lithium-ion Batteries: Review and Future Challenges," *Electronics*, vol. 6, no. 4, p. 102, Nov. 23, 2017, ISSN: 2079-9292. DOI: 10.3390/electronics6040102. [Online]. Available: http://www.mdpi.com/2079-9292/6/4/102 (visited on 11/09/2020).

[67] D. N. T. How, M. A. Hannan, M. S. Hossain Lipu, and P. J. Ker, "State of Charge Estimation for Lithium-Ion Batteries Using Model-Based and Data-Driven Methods: A Review," *IEEE Access*, vol. 7, pp. 136 116–136 136, 2019, ISSN: 2169-3536. DOI: 10.1109/ACCESS.2019.2942213. [Online]. Available: https://ieeexplore.ieee.org/document/8843918/ (visited on 11/09/2020).

[68] B. Liu, M. Liu, X. Jiang, X. Tuo, H. Zhou, and J. Ren, "Design of Battery Management System Based on DSP for BEV," *2017 9th International Conference on Modelling, Identification and Control (ICMIC)*, vol. 1, no. 1, p. 6, 2017, ISSN: 978-1-5090-6575-2. DOI: 10.1109/ICMIC.2017.8321574. [Online]. Available: https://ieeexplore-ieee-org.galanga.hvl.no/document/8321574.

[69] H. Rahimi-Eichi, U. Ojha, F. Baronti, and M.-Y. Chow, "Battery Management System: An Overview of Its Application in the Smart Grid and Electric Vehicles," *IEEE Industrial Electronics Magazine*, vol. 7, no. 2, pp. 4–16, Jun. 2013, ISSN: 1932-4529. DOI: 10.1109/MIE.2013.2250351. [Online]. Available: http://ieeexplore.ieee.org/document/6532486/ (visited on 05/19/2021).

[70] J. Liu, L. Sheng, J. Shi, Z. Zhang, and X. He, "Design of High Voltage, High Power and High Frequency Transformer in LCC Resonant Converter," *2009 Twenty-Fourth Annual IEEE Applied Power Electronics Conference and Exposition*, vol. 1, no. 1, p. 5, Feb. 2009, ISSN: 1048-2334. DOI: 10.1109/APEC.2009.4802790.

[71] S. Sabri, E. Van Brunt, A. Barkley, B. Hull, M. O'Loughlin, A. Burk, S. Allen, and J. Palmour, "New generation 6.5 kV SiC power MOSFET," in *2017 IEEE 5th Workshop on Wide Bandgap Power Devices and Applications (WiPDA)*, Albuquerque, NM: IEEE, Oct. 2017, pp. 246–250, ISBN: 978-1-5386-3117-1. DOI: 10.1109/WiPDA.2017.8170555. [Online]. Available: http://ieeexplore.ieee.org/document/8170555/ (visited on 05/06/2021).

[72] J. McBryde, A. Kadavelugu, B. Compton, S. Bhattacharya, M. Das, and A. Agarwal, "Performance comparison of 1200V Silicon and SiC devices for UPS application," in *IECON 2010 - 36th Annual Conference on IEEE Industrial Electronics Society*, Glendale, AZ, USA: IEEE, Nov. 2010, pp. 2657–2662, ISBN: 978-1-4244-5225-5. DOI: 10.1109/IECON.2010.5675125. [Online]. Available: http://ieeexplore.ieee.org/document/5675125/ (visited on 02/08/2021).

[73] B. Callanan, "Application Considerations for Silicon Carbide MOSFETs," CREE, 2011. [Online]. Available: https://www.richardsonrfpd.com/docs/rfpd/Wlf_App_SiC_MOSFET.pdf.

[74] M. Liang, T. Q. Zheng, and Y. Li, "Performance evaluation of SiC MOSFET, Si CoolMOS and IGBT," in *2014 International Power Electronics and Application Conference and Exposition*, Shanghai, China: IEEE, Nov. 2014, pp. 1369–1373, ISBN: 978-1-4799-6768-

1. DOI: 10.1109/PEAC.2014.7038063. [Online]. Available: http://ieeexplore.ieee.org/document/7038063/ (visited on 02/08/2021).

[75] R. Callanan, A. Agarwal, A. Burk, M. Das, B. Hull, F. Husna, A. Powell, J. Richmond, Sei-Hyung Ryu, and Qingchun Zhang, "Recent progress in SiC DMOSFETs and JBS diodes at Cree," in *2008 34th Annual Conference of IEEE Industrial Electronics*, Orlando, FL: IEEE, Nov. 2008, pp. 2885–2890, ISBN: 978-1-4244-1767-4. DOI: 10.1109/IECON.2008.4758417. [Online]. Available: http://ieeexplore.ieee.org/document/4758417/ (visited on 10/05/2020).

[76] N. Vijaya Kumar and N. Lakshminarasamma, "Comparison of Planar Transformer Architectures and Estimation of Parasitics for High Voltage Low Power DC-DC Converter," in *2018 IEEE International Conference on Power Electronics, Drives and Energy Systems (PEDES)*, Chennai, India: IEEE, Dec. 2018, pp. 1–6, ISBN: 978-1-5386-9316-2. DOI: 10.1109/PEDES.2018.8707537. [Online]. Available: https://ieeexplore.ieee.org/document/8707537/ (visited on 02/09/2021).

[77] fredrikstorebo, *Fredrikstorebo/IBDC-Dual-Active-Bridge-Sim*, May 30, 2021. [Online]. Available: https://github.com/fredrikstorebo/IBDC-Dual-Active-Bridge-Sim (visited on 05/30/2021).

[78] S. Pittaway. (). "Stuartpittaway - Overview," GitHub, [Online]. Available: https://github.com/stuartpittaway (visited on 05/12/2021).

[79] *Stuartpittaway/diyBMSv4*, in collab. with S. Pittaway, version 4.0, May 11, 2021. [Online]. Available: https://github.com/stuartpittaway/diyBMSv4 (visited on 05/12/2021).

[80] fredrikstorebo, *Fredrikstorebo/Measurement-Card*, May 30, 2021. [Online]. Available: https://github.com/fredrikstorebo/Measurement-Card (visited on 05/30/2021).

[81] *Stuartpittaway/diyBMSv4Code*, in collab. with S. Pittaway, version 4.0, 3: 4, May 10, 2021. [Online]. Available: https://github.com/stuartpittaway/diyBMSv4Code (visited on 05/12/2021).

A IEEE ICECCME 2021 Conference Paper Submitted For Review

The battery prototype system and battery simulation developed in this thesis are together with the supercapacitor model designed by Marius Reigstad utilized for a paper submitted for review to the IEEE ICECCME 2021 conference.

Comparison of Supercapacitor and Battery Transient Response for DC-bus

Marius Reigstad, Fredrik Storebø and Vegard Steinsland*
Department of Computer science, Electrical engineering and Mathematical sciences
Western Norway University of Applied Sciences
Bergen, Norway
vegard.steinsland@hvl.no

***Abstract*—A comparison of different transient responses by a supercapacitor and battery reacting to a load is presented in this paper. The main focus is improving energy storage systems designed to support a DC-microgrid. This is done by introducing the two storage devices to act as stabilization elements. Through simulations in Matlab®/Simulink®and physical models, a comparison is achieved. Transient characteristics from the simulations tend to give a faster response than the physical. Verification on the error between ideal and physical are analyzed based on the results.**

***Index Terms*—Renewables, DC-bus, DC-microgrid, energy storage, battery, supercapacitor, isolated bidirectional DC/DC converter(IBDC),**

I. Introduction

This paper presents a comparison between the transient response of a battery and a supercapacitor connected to various loads. Energy storage and renewable energy production [1] connected with a DC-microgrid prove necessary for many applications [2]–[4], due to the unpredictability of renewables, as they often are dependent on irregular energy sources. In addition, the transient response in a DC system is more critical than in a comparable AC system.

The growing trend with wind- [5], [6] and solar-energy [7] is increasing the demand for energy storage with a low response time [8]. Combining energy storages with varying response times may respond faster to DC-microgrid energy demand. Storage devices as supercapacitors are assumed to react more rapidly to change in demand than devices like batteries. Thereby, combining the supercapacitor and the battery in a system, a faster response time can be achieved when required.

The use of batteries and supercapacitors in combination has been studied and researched; a paper on energy management of fuel cell, battery, and supercapacitor is described in [9], where the systems response time measurements are included. Similarly, [10] presents batteries and supercapacitors for use in electric/hybrid vehicles. Each storage device can deliver power to the DC-bus in a typical energy storage system through an isolated bidirectional DC/DC converter. A potential model configuration is shown in Fig. 1 which exhibits a simplified configuration. With a slightly faster storage device, the overall response time of the storage system can be significantly decreased.

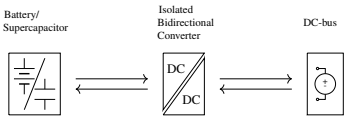

Figure 1: Model configuration for energy system

One of the principal differences between a battery and supercapacitor is power density versus energy density [11]–[13]. While a supercapacitor can release large amounts of energy in a short period, a battery can store significantly greater amounts of energy [14]. Therefore the supercapacitor possesses high power density while a battery has a high energy density compared to each other. Combining and compromising the sources provides a high-performance system with fast transient response.

The battery stores energy as an electrochemical reaction as opposed to the supercapacitor, which utilizes static charge [15], [16]. This difference in energy storage is the primary cause of the unique response times. This paper will showcase the difference in energy ability and response of the two sources while responding to a programmable load.

The paper is organized as follows: Section II presents the model description and laboratory test setup and the design of the batter and supercapacitor system. Section III presents the test cases with results. Section IV presents the conclusions.

II. Model Description

When comparing the transient response of the storage devices, they must have a common factor. In this paper, a requirement of a nominal voltage of close to 30 V is applied. However, the battery and supercapacitor capacity will vary, as this was not feasible to match.

Each supercapacitor cell has a maximum voltage of 2.7 V, thereby 12 single cells must be connected in series to reach a maximum voltage of 32.4 V and a nominal voltage of 30 V. The supercapacitor parameters are displayed in table I [18], while the maximum stored energy and usable specific power is calculated in (1) and (2), respectively. Compared to the supercapacitor, the battery has a higher cell voltage of 4.2 V,

Table I: Supercapacitor Module Specifications

Type	Value
Cells in Series	12
Capacitance	30 F
Nominal Voltage	30 V
Maximum Current	20 A
Maximum Power	600 W
DC ESR	38.4 mΩ
Maximum Stored Energy	3.75 W h
Usable Specific Power	3282.56 W/kg
Total SC Weight	0.8568 kg

Table II: Li-ion Battery Specifications

Type	Value
Cells in Series	8
Cells in Parallel	2
Nominal Voltage	29.6 V
Maximum Current	10.4 A
Maximum Power	305.76 W
DC ESR	38.4 mΩ
Maximum Stored Energy	159.92 W h
Usable Specific Power	409.36 W/kg
Total Battery Weight	0.752 kg

with a nominal voltage of 3.7 V; therefore, only eight cells connected in series are required. The battery parameters are collected from the datasheet [19] and presented in table II.

The supercapacitor and battery parameters showcase the difference between the storage devices. The maximum stored energy is significantly higher in the battery, while the usable specific power in the supercapacitor considerably exceeds the battery; this corresponds with the assumptions made in the introduction.

As the voltage requirement is set to 30 V, the supercapacitor is designed with 12 cells in series. These cells are soldered directly to a PCB, with built-in balancing and measurement [20]. The passive balancing system is designed with a constantly discharging current. As a cell charges to a higher voltage level than the rest, the discharging current increases, causing the pack to balance. Included in the PCB design is both current and voltage measurement over the supercapacitor bank.

The supercapacitor is charged up to the required 30 V with an EA-PS 2032-050 30V laboratory power supply. A passive cell balancing circuit is designed, to prevent un-even cell charging. This system balances the cells so that the cells with higher voltage discharge faster than the other. The PCB requires a 15 V DC supply to power the circuitry. For this supply, the mascot 719 DC power supply is utilized.

The battery is design as two 4S2P packs connected in series, equaling an 8S2P pack. The eight cells in series produce a nominal voltage of 29.6 V, while the parallel cells increase the capacity from 2.6 A h to 5.2 A h. Contrary to the supercapacitor, each cell pair of the battery pack is connected to a sensor PCB connected to a central controller PCB. These cards are based on an open-source project designed by Stuart Pittaway [20]. The sensor cards interact through standard UART serial communication with a single control card. The external sensor cards have implemented passive balancing. Instead of constantly discharging the cells, they are only discharged when the voltage level is too high. This action is achieved by redirecting the current through a MOSFET when required.

$$E_{max} = \frac{0.5 \cdot C \cdot {V_R}^2}{3600} \tag{1}$$

$$P_{usable} = \frac{0.12 \cdot {V_R}^2}{ESR_{DC} \cdot Weight} \tag{2}$$

The measured cell voltage is presented to the controller PCB and can be displayed on a local network. This system requires a 5 V DC supply via a USB charger to power the wifi controller. However, the balancing circuit will work without this supply. Due to the unique charging characteristic of the lithium-ion battery, a constant-current constant-voltage charger is obliged to charge the battery. For this purpose, a SkyRc E680 smart charger is applied to charge the voltage to 30 V.

Equipment used during testing is found in table III. The setup displayed in Fig. 2 consists of a programmable load, the sources, and an oscilloscope. The load is an EL 9500-08 T electronic DC load. With a maximum input voltage of 500 V and a maximum input current of 8 A, it is thereby not limited by the battery or supercapacitor at 30 V. The load features a touchscreen and simple control settings, allowing for fast and easy tests and use. The current mode is set to rectangular function for the tests, which produces a square wave signal for the input current.

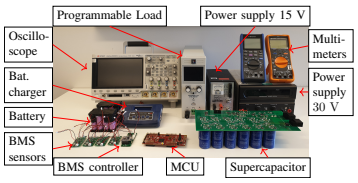

Figure 2: Laboratory test equipment

Table III: Laboratory test equipment

Type	Manufacturer	Type
Programmable Load	Elektro-Automatik	9500-08 T
Oscilloscope	Keysight	MSOX3014A
Diff. Probe	Micsig	DP10013
Current Probe	Micsig	CP2100A
Power Supply	Elektro-Automatik	EA-PS 2032-050
Power Supply	Mascot	719
Battery Charger	SkyRc	E680
Supercapacitor	Maxwell Technologies	BCAP0360 P270 S18
Battery	Samsung	18650

The controller can adjust the amplitude to reach the required

current level and change the upper and lower pulse width. For the test performed, both pulse width is 1 ms, and the current amplitude increases to 2 A, 4 A, 6 A, and 8 A between each test. The frequency of the pulse will therefore be 500 Hz, with a duty cycle of 50%. This square wave signal is measured with a CP2100A current probe connected to an MSOX3014A oscilloscope from Keysight. For the voltage measurement, a DP10013 differential probe is utilized. These probes have an accuracy of 3% and 2%, respectively.

III. Results

The current and voltage response by the supercapacitor from the laboratory tests are plotted in Fig. 3. From Fig. 3a, the current rises steadily from zero to each load current reference of 2 A, 4 A, 6 A, and 8 A. The plot characteristic from the currents are displayed in table IV, and are obtained from Matlab®by utilizing the "stepinfo" command. The rise time is the period between 10% and 90% of the steady-state value and shows the rate of current increase.

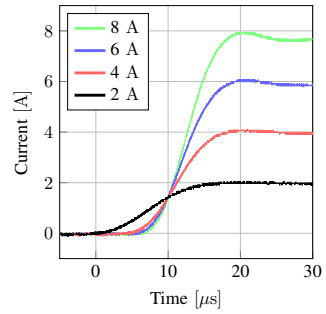

(a) Currents

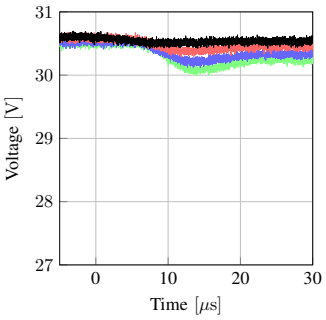

(b) Voltage transients

Figure 3: Supercapacitor current and voltage during load scenarios from physical model

However, it is essential to note the complete response from time zero when the load is initially connected. The settling time is the period between the initial step response and a value within 2% of the steady-state value. The overshoot represent the maximum percentage the response touches compared to the steady-state value. The response of the supercapacitor voltage presented in Fig. 3b shows the decreasing voltage in response to the current increase. The voltage-drop has a magnitude of 0.06 V, 0.16 V, 0.2 V, 0.26 V in response to the load currents. The results from the battery test are plotted in Fig. 4. The currents are stepped up from zero to 2 A, 4 A, 6 A, and 8 A, similar to the supercapacitor test. The current transient response is shown in Fig. 4a, while the voltage transient is shown in Fig. 4b. The plot characteristics for the current response is listed in table. V. The voltage-drop is 0.5 V, 1 V, 1.5 V, and 1.93 V, respectively to the load currents. A comparison between the physical setup and the modeled simulation in Matlab®/Simulink® is made. The simulated battery and supercapacitor models utilized are part of the Simscape electrical library.

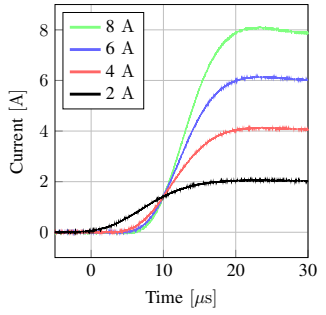

(a) Currents

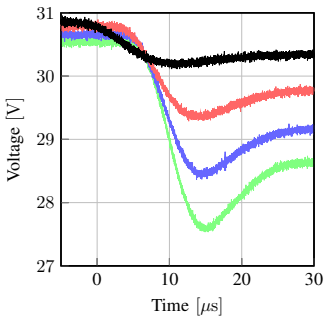

(b) Voltage transients

Figure 4: Battery current and voltage during load scenarios from physical model

Table IV: Plotinfo for supercapacitor current Fig. 3a

Type	2 A	4 A	6 A	8 A
RiseTime (µs)	10.086	8.2610	7.8208	7.6040
SettlingTime (µs)	52.172	14.547	33.007	24.746
Overshoot (%)	4.0666	4.0535	1.3407	0.7588

Table V: Plotinfo for battery current Fig. 4a

Type	2 A	4 A	6 A	8 A
RiseTime (µs)	11.313	9.5400	8.8175	8.4550
SettlingTime (µs)	21.345	17.980	17.820	24.640
Overshoot (%)	4.0330	4.0164	3.3649	1.7572

The simulated test models are designed to replicate the physical laboratory tests. The current and voltage responses from the simulated supercapacitor model are shown in Fig. 5a, and from the physical battery model are visualized in Fig. 6a. The supercapacitor and battery simulations in Figs. 5 and 6 show an almost instant current response. The voltage response shows an instant voltage-drop for the supercapacitor in Fig. 5b and decreases with 0.08 V, 0.16 V, 0.23 V and 0.31 V, respective to the load currents. The battery voltages indicate a steady decreasing curve when the current increases, visualized in Fig. 5b. The battery voltages decrease with 0.13 V, 0.26 V, 0.39 V and 0.53 V respective to the increasing load currents. The load step is initiated at time zero for every test and simulation.

IV. Discussion

The physical supercapacitor and battery currents are fairly similar at first glance, displayed in Fig. 3a and 4a. The battery currents start to rise slightly before the supercapacitor currents with an inconsiderably less steep curve. This results in a faster rise time for the supercapacitor, visualized in table IV and V. The supercapacitor 8 A load current show a sag after reaching the reference value at 20 µs. This dip is neutralized shortly outside the included time plot and indicates increasing times for larger load. The same behavior is visualized for the battery current with a slower response. This results in a small overshoot and a smaller sag. The characteristic of both the current and voltage response displays an anomaly for the 2 A.

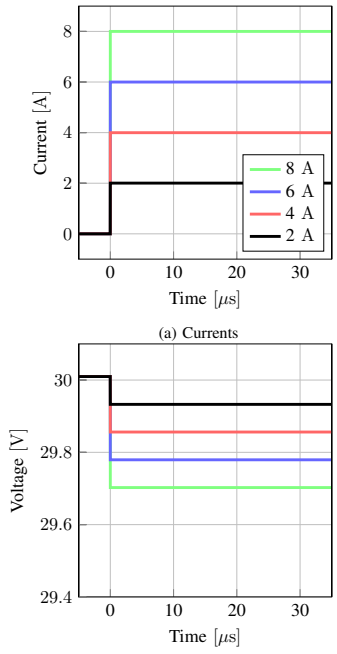

(a) Currents

(b) Voltage transients

Figure 5: Supercapacitor current and voltage during load scenarios from simulation model

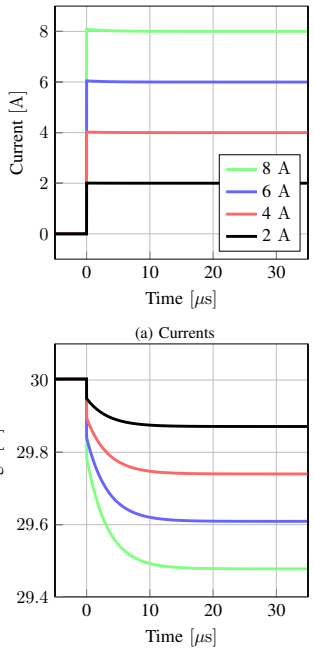

(a) Currents

(b) Voltage transient

Figure 6: Battery current and voltage during load scenarios from simulation model

As the load connects, the current rises almost immediately from the initial pulse at time zero. This characteristic visualizes a delayed response for larger currents. This delay is explained by the load not responding fast enough. Contrary to the currents, the difference in voltage response of the battery and the supercapacitor is more visually noticeable when comparing Fig. 3b and 4b. The large difference in voltage-drop explains this visual difference. For the $8\ \mathrm{A}$ load, the supercapacitor stabilize at $300\ \mathrm{mV}$ lower and the battery closer to $1.8\ \mathrm{V}$. This is a significant contrast and originates from the large power density difference. It will also depend on the strength of the storage device. Moreover, the supercapacitor is built with physically larger cells, and another improvement to this experiment is to make the battery pack larger, with more cells in parallel, thereby increasing the capacity. This improvement will make the battery pack more robust and able to withstand the load better. Both display the same transient voltage-drop curve with an under-shoot and stabilize when the current reaches the reference value. The shape of the curve seemingly originates from the programmable DC-load.

Both physical storage devices are compared with simulated results of matching parameters. The supercapacitor displays the largest difference with the simulated supercapacitor's instant transient response during the same time window. This will have a significant impact when taking a simulation into a physical design. The voltage-drop is surprisingly similar with $300\ \mathrm{mV}$. The simulated battery, however, indicates a less ideal transient voltage response. Compared to the physical battery, the voltage transients show no under-shoot and a significantly smaller voltage-drop of $520\ \mathrm{mV}$ for the $8\ \mathrm{A}$ load. This indicates a limitation of the simulated battery because of the large contrast compared to the physical.

V. Conclusion

This paper compares the transient responses of both physical and simulated supercapacitor and battery storage devices. The contrasts are displayed through physical tests with a programmable DC-load, and simulations in Matlab®/Simulink®.

The results indicate a slightly faster electric response for the physical supercapacitor compared to the battery. The physical battery shows a significant voltage-drop compared to the supercapacitor, originating from the supercapacitor's bigger power density. A significant difference in voltage transient is visualized between both physical storage devices and their respective simulations. The simulated storage devices show a more consistent voltage-drop curve for all loads. Considerations need to be made when taking simulations into physical prototypes designed for DC-microgrids.

References

[1] J. M. Carrasco et al., "Power-Electronic Systems for the Grid Integration of Renewable Energy Sources: A Survey," IEEE Transactions on Industrial Electronics, vol. 53, no. 4, pp. 1002–1016, Jun. 2006, doi: 10.1109/TIE.2006.878356.

[2] D. E. Olivares et al., "Trends in Microgrid Control," IEEE Transactions on Smart Grid, vol. 5, no. 4, pp. 1905–1919, Jul. 2014, doi: 10.1109/TSG.2013.2295514.

[3] H. Kanchev, D. Lu, F. Colas, V. Lazarov, and B. Francois, "Energy Management and Operational Planning of a Microgrid With a PV-Based Active Generator for Smart Grid Applications," IEEE Transactions on Industrial Electronics, vol. 58, no. 10, pp. 4583–4592, Oct. 2011, doi: 10.1109/TIE.2011.2119451.

[4] H. Zhou, T. Bhattacharya, D. Tran, T. S. T. Siew, and A. M. Khambadkone, "Composite Energy Storage System Involving Battery and Ultracapacitor With Dynamic Energy Management in Microgrid Applications," IEEE Transactions on Power Electronics, vol. 26, no. 3, pp. 923–930, Mar. 2011, doi: 10.1109/TPEL.2010.2095040.

[5] Y. Liu, W. Du, L. Xiao, H. Wang, and J. Cao, "A Method for Sizing Energy Storage System to Increase Wind Penetration as Limited by Grid Frequency Deviations," IEEE Transactions on Power Systems, vol. 31, no. 1, pp. 729–737, Jan. 2016, doi: 10.1109/TPWRS.2015.2396528.

[6] C. Abbey and G. Joos, "Supercapacitor Energy Storage for Wind Energy Applications," IEEE Transactions on Industry Applications, vol. 43, no. 3, pp. 769–776, May 2007, doi: 10.1109/TIA.2007.895768.

[7] M. Nassereddine, A. Hellany, M. Nagrial, J. Rizk, and D. D. Micu, "Utilities investments into residential properties: PV solar system with energy storage," in 2016 51st International Universities Power Engineering Conference (UPEC), Sep. 2016, pp. 1–4, doi: 10.1109/UPEC.2016.8114083.

[8] J. P. Barton and D. G. Infield, "Energy storage and its use with intermittent renewable energy," IEEE Transactions on Energy Conversion, vol. 19, no. 2, pp. 441–448, Jun. 2004, doi: 10.1109/TEC.2003.822305.

[9] R. Bambang, A. Syaichu-Rohman, C. Dronkers, R. Ortega, and A. Sasongko, "Energy Management of Fuel Cell/Battery/Supercapacitor Hybrid Power Sources Using Model Predictive Control," IEEE Transactions on Industrial Informatics, vol. 10, Nov. 2014, doi: 10.1109/TII.2014.2333873.

[10] A. F. Burke, "Batteries and Ultracapacitors for Electric, Hybrid, and Fuel Cell Vehicles," Proceedings of the IEEE, vol. 95, no. 4, pp. 806–820, Apr. 2007, doi: 10.1109/JPROC.2007.892490.

[11] T. Ming, W. Deng, J. Wu, and Q. Zhang, "A hierarchical energy management strategy for battery-supercapacitor hybrid energy storage system of electric vehicle," in 2014 IEEE Conference and Expo Transportation Electrification Asia-Pacific (ITEC Asia-Pacific), Aug. 2014, pp. 1–5, doi: 10.1109/ITEC-AP.2014.6941167.

[12] A. Khaligh and Z. Li, "Battery, Ultracapacitor, Fuel Cell, and Hybrid Energy Storage Systems for Electric, Hybrid Electric, Fuel Cell, and Plug-In Hybrid Electric Vehicles: State of the Art," IEEE Transactions on Vehicular Technology, vol. 59, no. 6, pp. 2806–2814, Jul. 2010, doi: 10.1109/TVT.2010.2047877.

[13] J. Bauman and M. Kazerani, "A Comparative Study of Fuel-Cell–Battery, Fuel-Cell–Ultracapacitor, and Fuel-Cell–Battery–Ultracapacitor Vehicles," IEEE Transactions on Vehicular Technology, vol. 57, no. 2, pp. 760–769, Mar. 2008, doi: 10.1109/TVT.2007.906379.

[14] E. Schaltz, A. Khaligh, and P. O. Rasmussen, "Influence of Battery/Ultracapacitor Energy-Storage Sizing on Battery Lifetime in a Fuel Cell Hybrid Electric Vehicle," IEEE Transactions on Vehicular Technology, vol. 58, no. 8, pp. 3882–3891, Oct. 2009, doi: 10.1109/TVT.2009.2027909.

[15] M. Chen and G. A. Rincon-Mora, "Accurate electrical battery model capable of predicting runtime and I-V performance," IEEE Transactions on Energy Conversion, vol. 21, no. 2, pp. 504–511, Jun. 2006, doi: 10.1109/TEC.2006.874229.

[16] S. Buller, M. Thele, R. W. A. A. De Doncker, and E. Karden, "Impedance-based simulation models of supercapacitors and Li-ion batteries for power electronic applications," IEEE Transactions on Industry Applications, vol. 41, no. 3, pp. 742–747, May 2005, doi: 10.1109/TIA.2005.847280.

[17] C. Shuaixun, H. Gooi, and M. Wang, "Sizing of Energy Storage for Microgrids," IEEE Trans. Smart Grid, vol. 3, pp. 142–151, Mar. 2012, doi: 10.1109/TSG.2011.2160745.

[18] NESSCAP/Maxwell, "BCAP0360 P270 S18 Datasheet," 2020. https://pdf.component-en.com/BCAP0360-P270-S18-2437562.pdf (accessed Mar. 25, 2021).

[19] S. Lee, "SPECIFICATION OF PRODUCT for Lithium-ion Rechargeable Cell," no. 1, p. 18, 2009.

[20] D. Linzen, S. Buller, E. Karden, and R. W. D. Doncker, "Analysis and evaluation of charge-balancing circuits on performance, reliability, and lifetime of supercapacitor systems," IEEE Transactions on Industry Applications, vol. 41, no. 5, pp. 1135–1141, Sep. 2005, doi: 10.1109/TIA.2005.853375.

B IEEE SEST 2021 Conference Approved Abstract

The approved abstract for the IEEE SEST 2021 conference. The full paper was not submitted to this conference before the deadline due to delay cause by covid-19.

Comparison of Supercapacitor and Battery Transient Response for DC-bus

Marius Reigstad, Fredrik Storebø and Vegard Steinsland*
Department of Computer science, Electrical engineering and Mathematical sciences
Western Norway University of Applied Sciences
Bergen, Norway
vegard.steinsland@hvl.no

***Abstract*—A comparison of the different transient responses of a supercapacitor and a battery supporting a DC-bus is presented in this paper. The main focus is to improve energy storage systems designed to support DC-bus in a microgrid. This is done by introducing a battery or a supercapacitor to act as a stabilization element. The two elements will be compared through simulations in Matlab/Simulink and physical components. Transient characteristics from the simulations tends to give a faster response then the physical components. A verification on the error between ideal and physical are analysed based on both simulations and measurements. The results will be presented in the full text paper.**

***Index Terms*—Renewables, DC-bus, DC-microgrid, energy storage, battery, supercapacitor, isolated bidirectional DC/DC converter(IBDC),**

I. Relevant Conference Scope

This paper fits well into the conference scopes of SEST2021 and the authors agree that the scope prioritization for this paper is:

1) Energy Storage Systems and Technologies
2) Microgrids, Virtual Power Plants, and Aggregators
3) Renewable Energy and Distributed Generation

II. Introduction

This paper presents a comparison between battery and supercapacitor transient response when supporting a DC-bus. Energy storage together with renewable energy [1] production and DC-microgrid is proving to be a necessity for many applications [2]. A growing trend with wind [3] and solar [4] is increasing the demand for energy storage with a low response time [5] [6]. By combining different storage devices the system will be able to respond faster to the DC-microgrids demand. The faster storage can initially react before the main storage responds. A paper on energy management of fuel-cell, battery and supercapacitor is described in [7], where measurements of the systems response time is included. Both of the energy storage devices will deliver power to the DC-bus through a isolated bidirectional DC/DC converter(IBDC). The model configuration is shown in Fig. 1 and shows how the two sources are connected. The main difference between a battery and a supercapacitor is power density versus energy density [8]. While a supercapacitor can release large amounts of energy in a short period of time, a battery can store larger amounts of energy [8]. This is why a supercapacitor has high power density while a battery has high energy density compared to each other. This paper will showcase the difference in energy ability of the two sources through the response of a dropping DC-bus by supporting the transient period [8] [9].

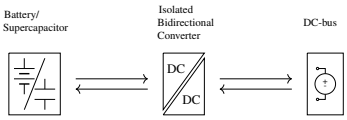

Figure 1: Model configuration for energy system

III. Results

Simulation results for both the supercapacitor and the battery can be seen in Fig. 2. Both the voltage and current response is shown. The voltage level on the DC-bus is set to $400\,\mathrm{V}$ and the current load is $1.2\,\mathrm{kW}$. The voltage drops as a load increase is forced on the DC-bus. When it reaches roughly $360\,\mathrm{V}$ the energy system responds. The load current decreases as the external energy storage takes time to respond. Simulink simulation shows a small difference in the transient response from a battery compared to supercapacitor. A voltage overshoot can also be seen from the battery simulation. As these are ideal components, a slightly different behavior from physical components is expected. These will be analysed and simulated in full paper. From the simulation it is expected that the supercapacitor will have a faster response than the battery with physical components [7]. A method based on the cost benefit for optimal sizing is presented in [10]. The size of a storage device is dependent on the required power and amount of time the DC-bus has to be supported [10].

IV. Conclusion

With the responses from the Matlab/Simulink simulations, the supercapacitor and battery shows signs of a different transient response then the physical measurements. The error between the physical and simulated model is shown through this paper. More results from simulations and physical model will be included in full paper.

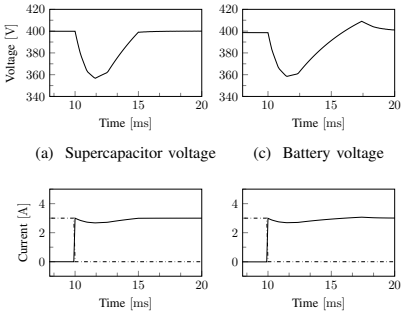

(a) Supercapacitor voltage (c) Battery voltage

(b) Supercapacitor current (d) Battery current

Figure 2: Transient response of battery and supercapacitor

REFERENCES

[1] J. M. Carrasco et al., "Power-Electronic Systems for the Grid Integration of Renewable Energy Sources: A Survey," IEEE Transactions on Industrial Electronics, vol. 53, no. 4, pp. 1002–1016, Jun. 2006, doi: 10.1109/TIE.2006.878356.

[2] D. E. Olivares et al., "Trends in Microgrid Control," IEEE Transactions on Smart Grid, vol. 5, no. 4, pp. 1905–1919, Jul. 2014, doi: 10.1109/TSG.2013.2295514.

[3] Y. Liu, W. Du, L. Xiao, H. Wang, and J. Cao, "A Method for Sizing Energy Storage System to Increase Wind Penetration as Limited by Grid Frequency Deviations," IEEE Transactions on Power Systems, vol. 31, no. 1, pp. 729–737, Jan. 2016, doi: 10.1109/TPWRS.2015.2396528.

[4] M. Nassereddine, A. Hellany, M. Nagrial, J. Rizk, and D. D. Micu, "Utilities investments into residential properties: PV solar system with energy storage," in 2016 51st International Universities Power Engineering Conference (UPEC), Sep. 2016, pp. 1–4, doi: 10.1109/UPEC.2016.8114083.

[5] J. P. Barton and D. G. Infield, "Energy storage and its use with intermittent renewable energy," IEEE Transactions on Energy Conversion, vol. 19, no. 2, pp. 441–448, Jun. 2004, doi: 10.1109/TEC.2003.822305.

[6] C. Abbey and G. Joos, "Supercapacitor Energy Storage for Wind Energy Applications," IEEE Transactions on Industry Applications, vol. 43, no. 3, pp. 769–776, May 2007, doi: 10.1109/TIA.2007.895768.

[7] R. Bambang, A. Syaichu-Rohman, C. Dronkers, R. Ortega, and A. Sasongko, "Energy Management of Fuel Cell/Battery/Supercapacitor Hybrid Power Sources Using Model Predictive Control," IEEE Transactions on Industrial Informatics, vol. 10, Nov. 2014, doi: 10.1109/TII.2014.2333873.

[8] T. Ming, W. Deng, J. Wu, and Q. Zhang, "A hierarchical energy management strategy for battery-supercapacitor hybrid energy storage system of electric vehicle," in 2014 IEEE Conference and Expo Transportation Electrification Asia-Pacific (ITEC Asia-Pacific), Aug. 2014, pp. 1–5, doi: 10.1109/ITEC-AP.2014.6941167.

[9] D. Linzen, S. Buller, E. Karden, and R. W. D. Doncker, "Analysis and evaluation of charge-balancing circuits on performance, reliability, and lifetime of supercapacitor systems," IEEE Transactions on Industry Applications, vol. 41, no. 5, pp. 1135–1141, Sep. 2005, doi: 10.1109/TIA.2005.853375.

[10] C. Shuaixun, H. Gooi, and M. Wang, "Sizing of Energy Storage for Microgrids," IEEE Trans. Smart Grid, vol. 3, pp. 142–151, Mar. 2012, doi: 10.1109/TSG.2011.2160745.

C DAB Converter Simulation Model

Full simulation model and source code of the isolated bidirectional dc-dc converter designed in Matlab®/Simulink®. The source files are published to a public repository in [77] and includes the initalizing file, main simulation file and calculations for the inductor.The files can be copied and redistributed in any medium or format. The pages in this appendix should be printed in A3 format to increase readability.

C.1 Converter Model

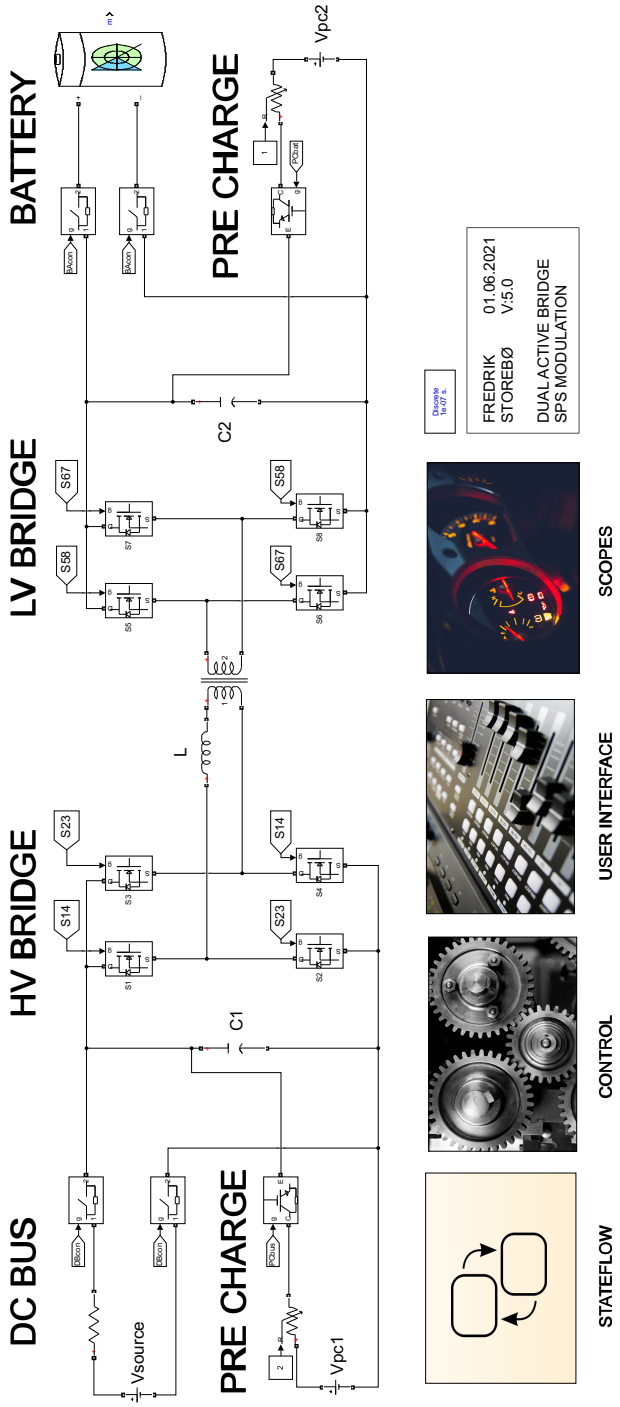

C.2 Stateflow subsystem

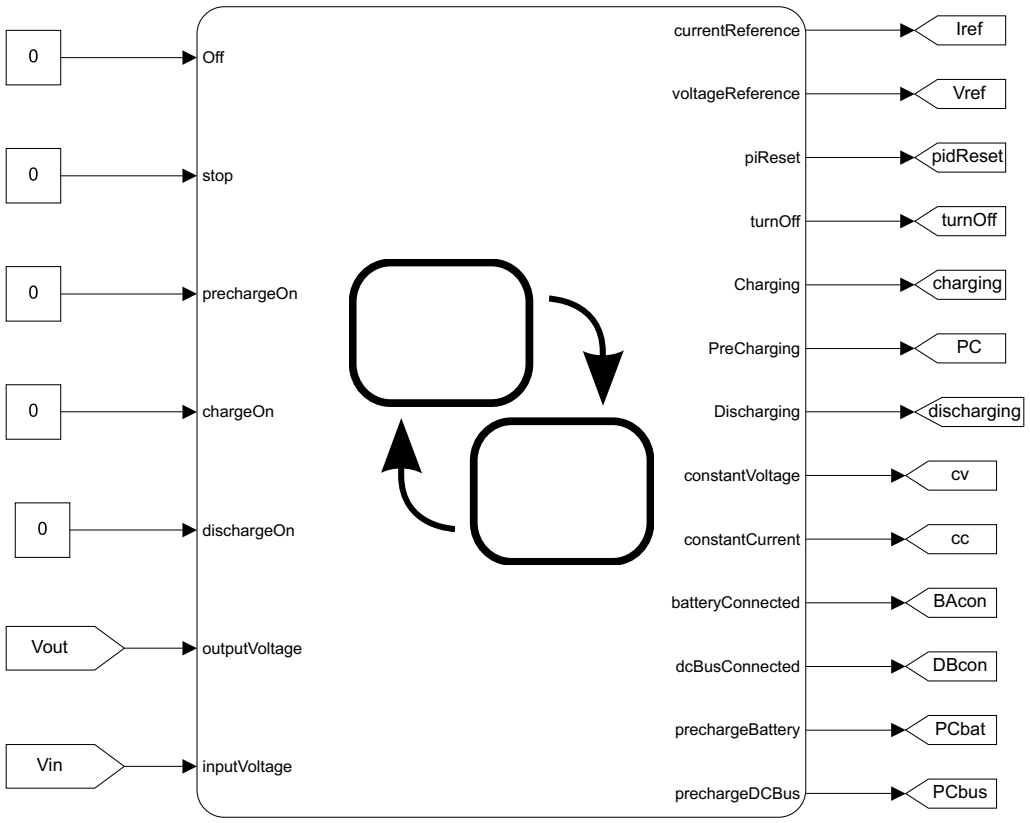

C.2.1 Stateflow subsystem

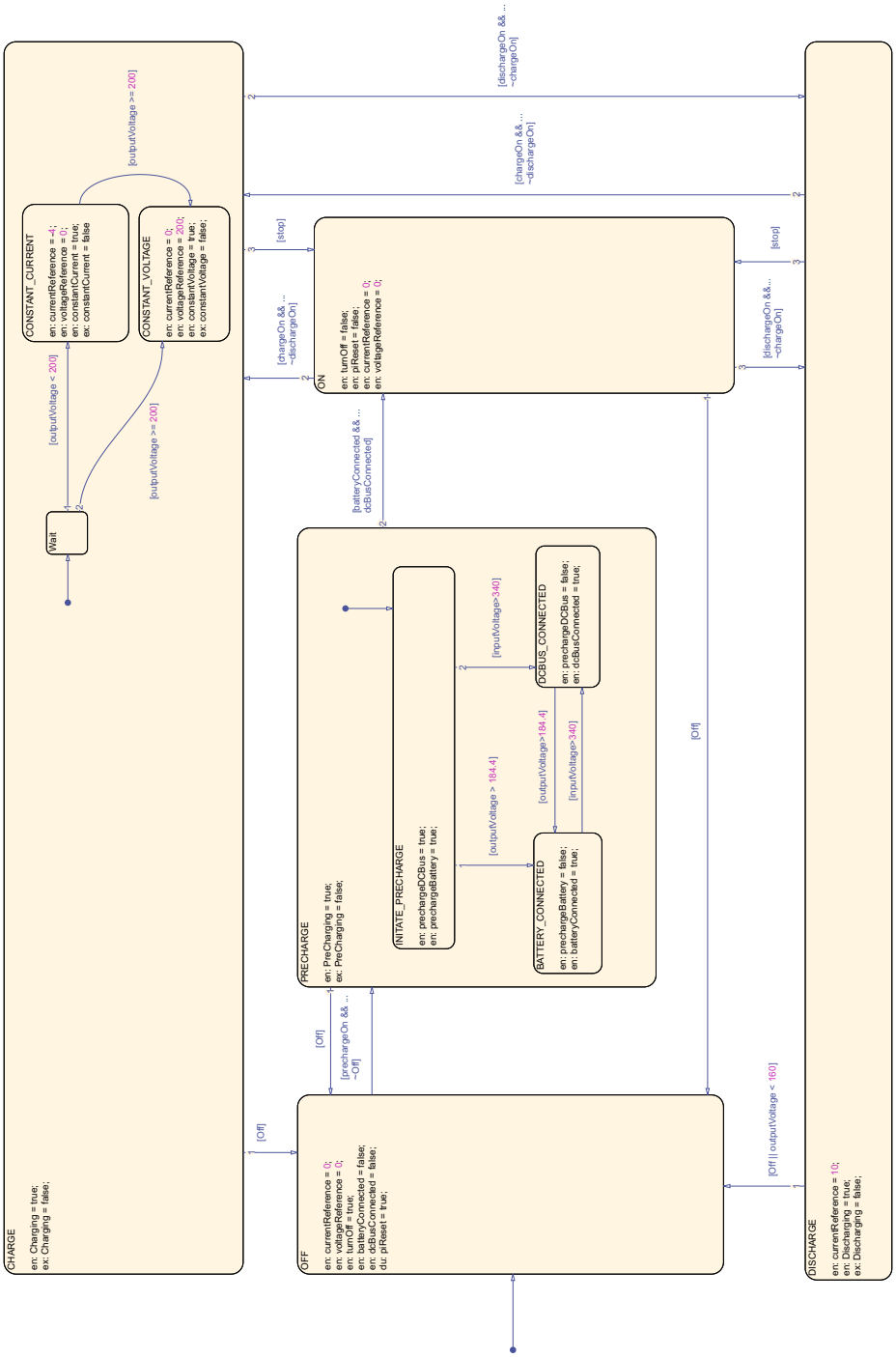

C.3 Control subsystem

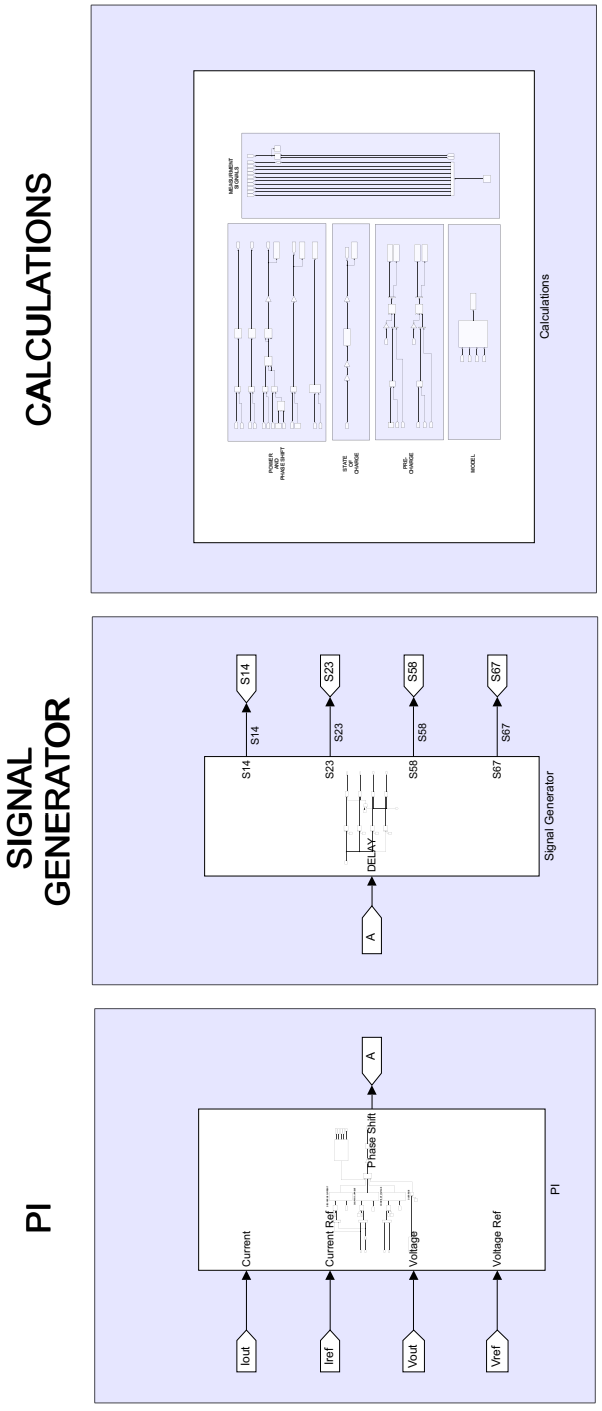

C.3.1 PI subsystem

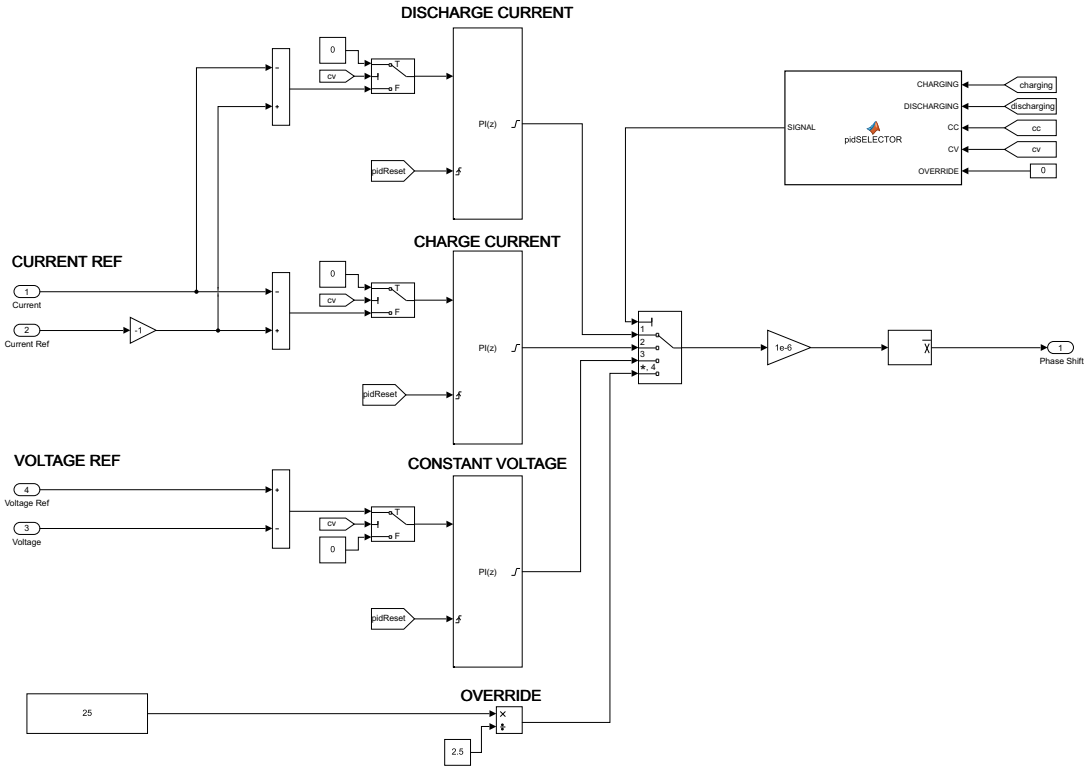

C.3.2 Signal generator subsystem

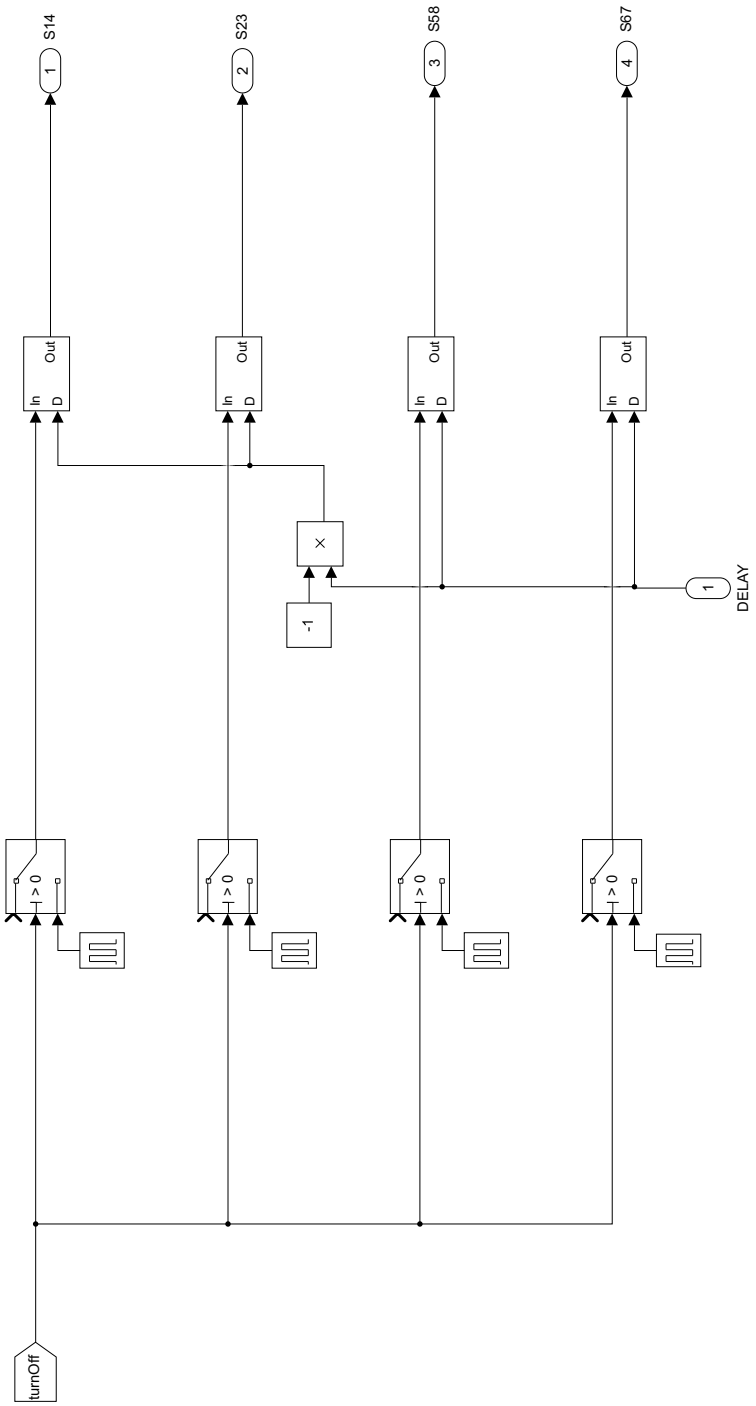

C.3.3 Calculation subsystem

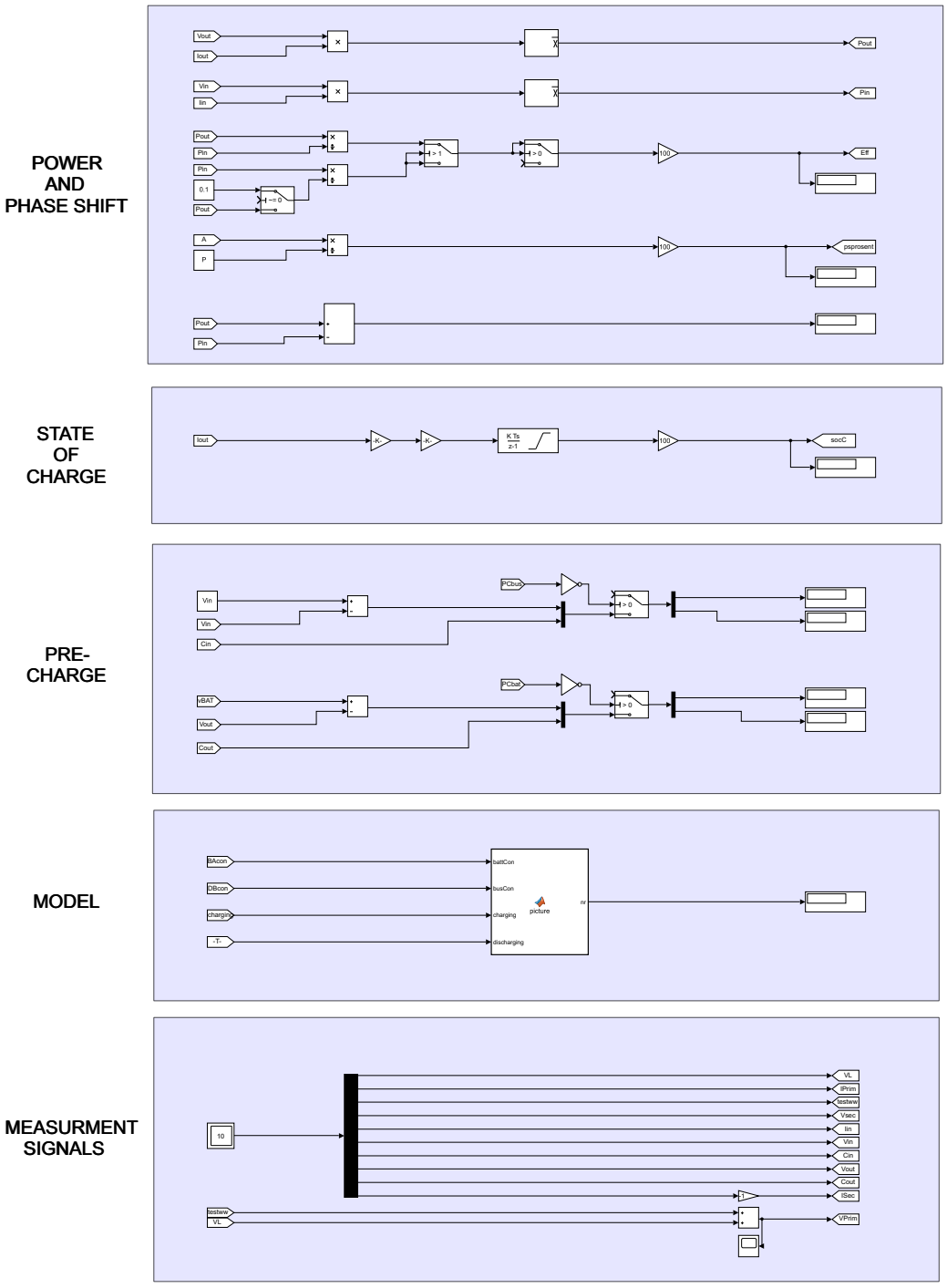

C.4 User Interface subsystem

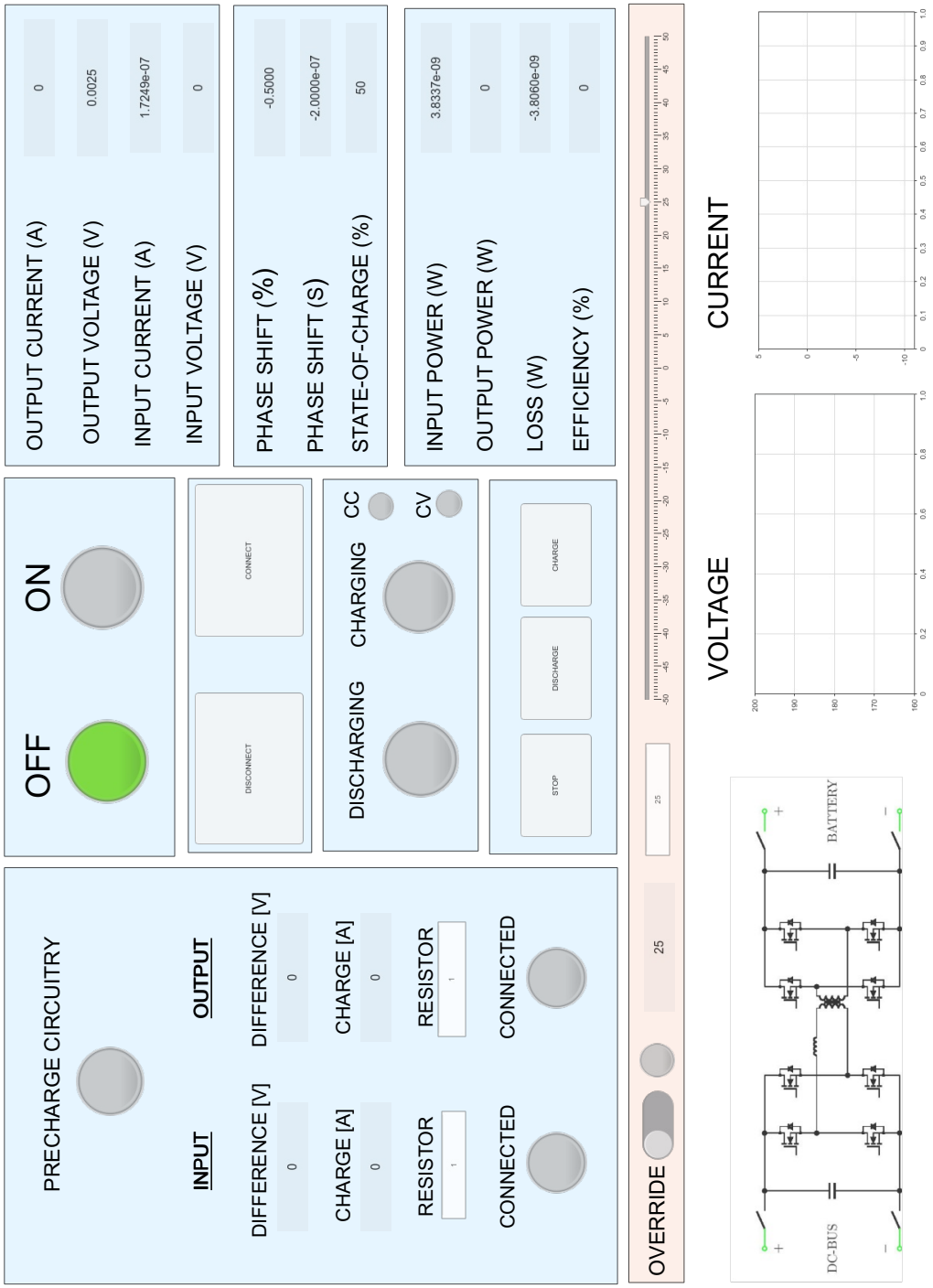

C.5 Scopes subsystem

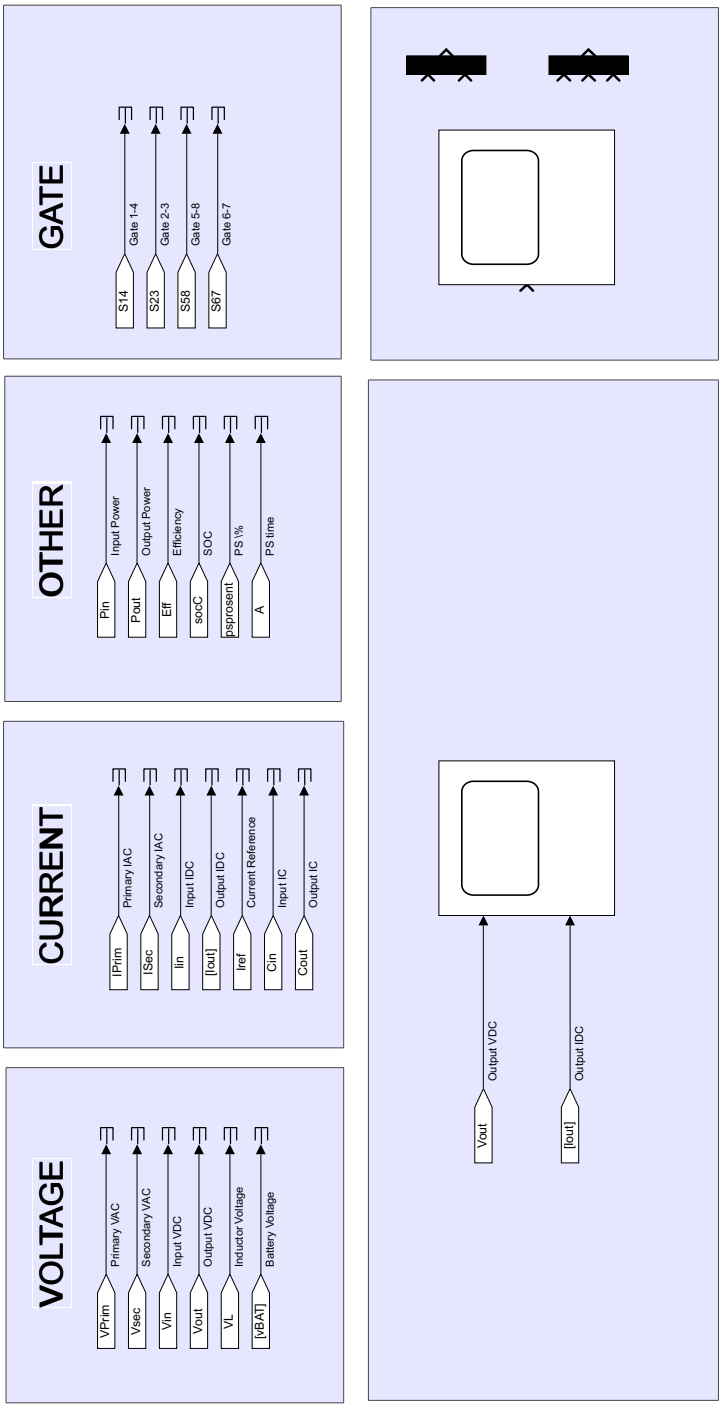

C.6 Matlab Script

C.6.1 Initialize file

```
clear
clc
% Standard**********************
Vin = 345;% V
Vref = 200;% V
f = 25e3;% Hz
P = 1/f;% s
Sample = 1e-7;% s
Power = 2000;% W
% MOSFET parameter***************
ron_mosfet_pri = 0.027;% Ohm
ron_mosfet_sec = 0.027;% Ohm
ron_body_diode_pri = 0.005;% Ohm
ron_body_diode_sec = 0.005;% Ohm
vf_body_diode_pri = 4;% V
vf_body_diode_sec = 4;% V
% Batteri parameter**************
SOCInit = 0.5;%
Vnominal = 171.2% V
Irated = 4.2;% Ah
% Komponenter********************
Lk = 2.04e-4;% H
C1 = 0.5e-3;% F
C2 = 0.5e-3;% F
% PreCharge**********************
pcBUS = 400;% V
pcBAT = 200;% V
% Transformer********************
NomPower = 2000;% VA
MagInductance = 720e-6;% H
LkInductance = 17e-6;% H
PrimDCr = 43e-3;% Ohm
SecDCr = 16e-3;% Ohm
PrimRMS = 248;% V
SecRMS = 132;% V
```

C.6.2 PI selector

```
function SIGNAL  = pidSELECTOR(CHARGING,DISCHARGING,CC,CV,OVERRIDE)


if (OVERRIDE==1)
    SIGNAL = 4;

elseif (CV==1)
     SIGNAL = 3;

elseif (CHARGING==1)
    SIGNAL = 2;

else
             SIGNAL = 1;
end
```

C.6.3 Figure selector

```
function nr = picture(battCon,busCon,charging,discharging)


if (charging)
    nr = 1;
elseif (discharging)
    nr = 2;
elseif (battCon && busCon)
    nr = 3;
elseif (battCon && ¬busCon)
    nr = 4;
elseif (¬battCon && busCon)
    nr = 5;
else
    nr = 6;
end
```

D Battery Simulation Model

Full simulation model of the simulated battery model designed in Matlab®/Simulink®. The pages in this appendix should be printed in A3 format to increase readability.

D.1 Battery simulation Model

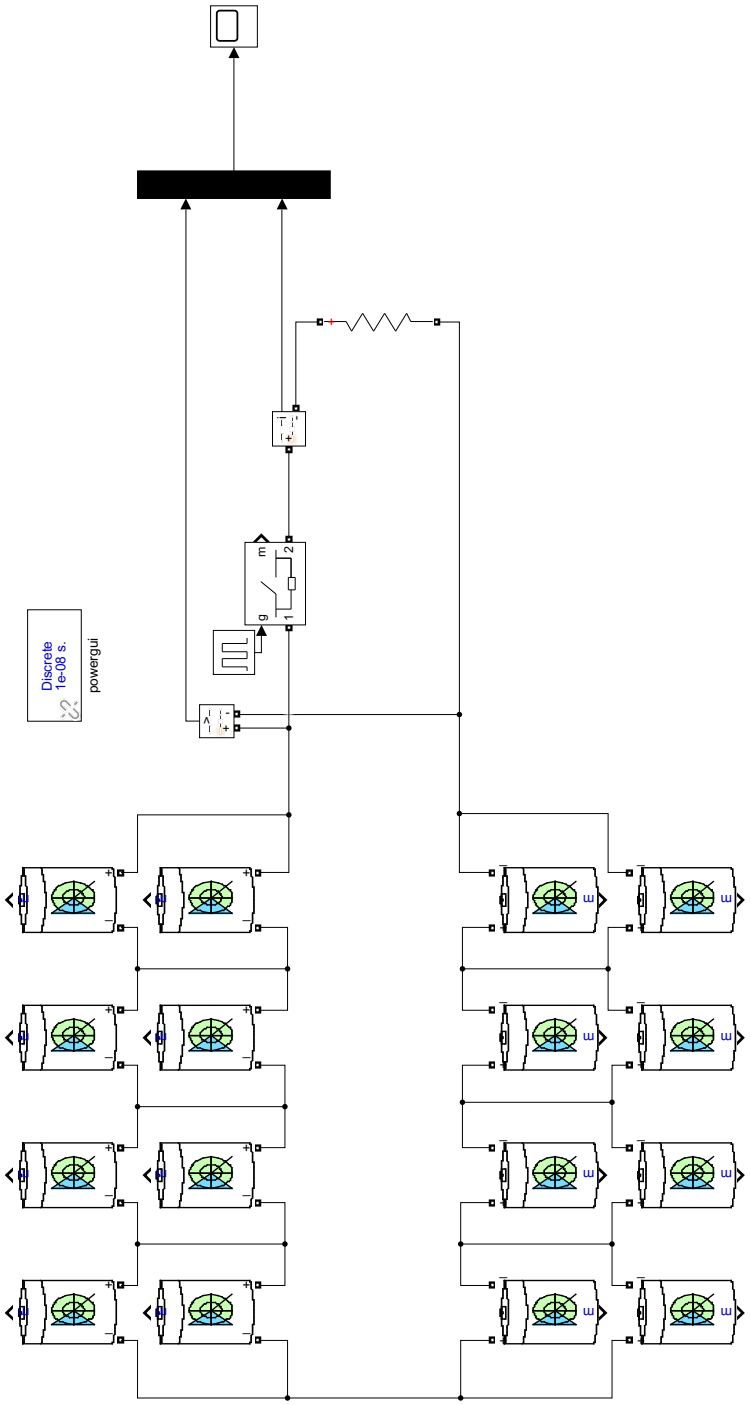

E Prototype Design With PCB

The schematic and copper layouts for the measurements and battery management system PCBs.The measurement card is designed in this thesis and published in repository [80]. This repository includes all the designs files from KiCad, and can be copied and redistributed in any medium or format. The BMS cards are pulled from the open source project on GitHub designed by Stuart Pittaway[78]. The pages in this appendix should be printed in A3 format to increase readability.

E.1 Measurement Card

The measurement card files are designed in this thesis and the entire KiCad project is published in GitHub [80].

E.1.1 Sensor Schematic

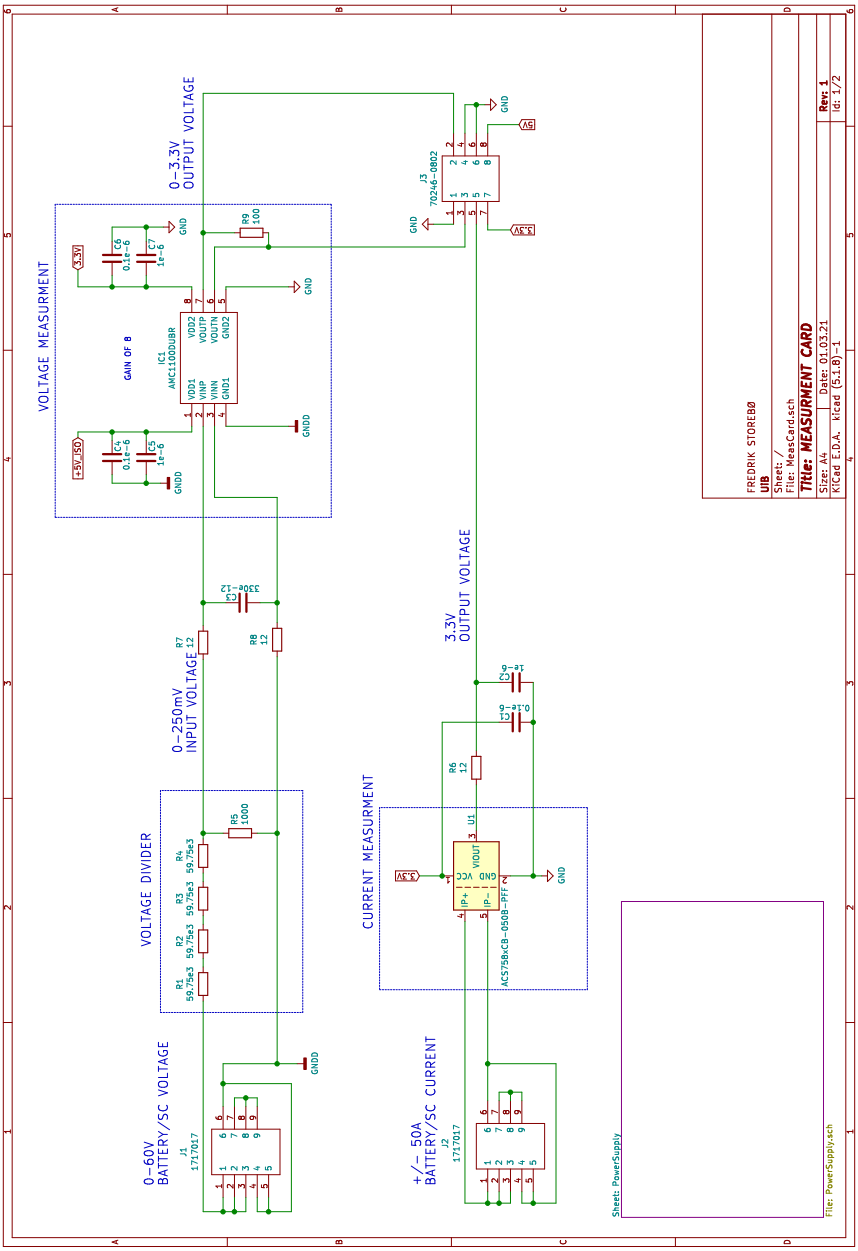

E.1.2 Supply schematic

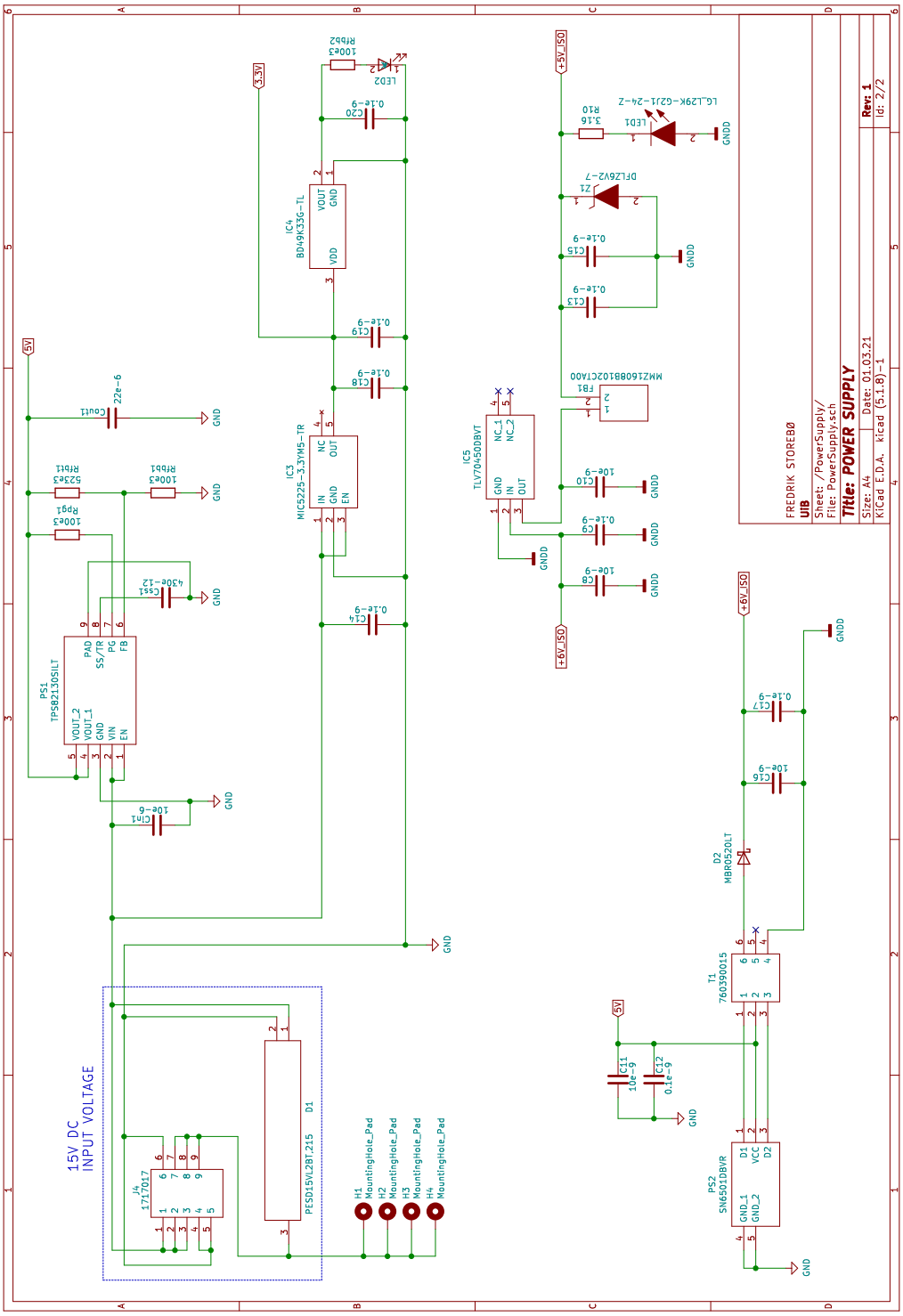

E.1.3 Copper Layout Front

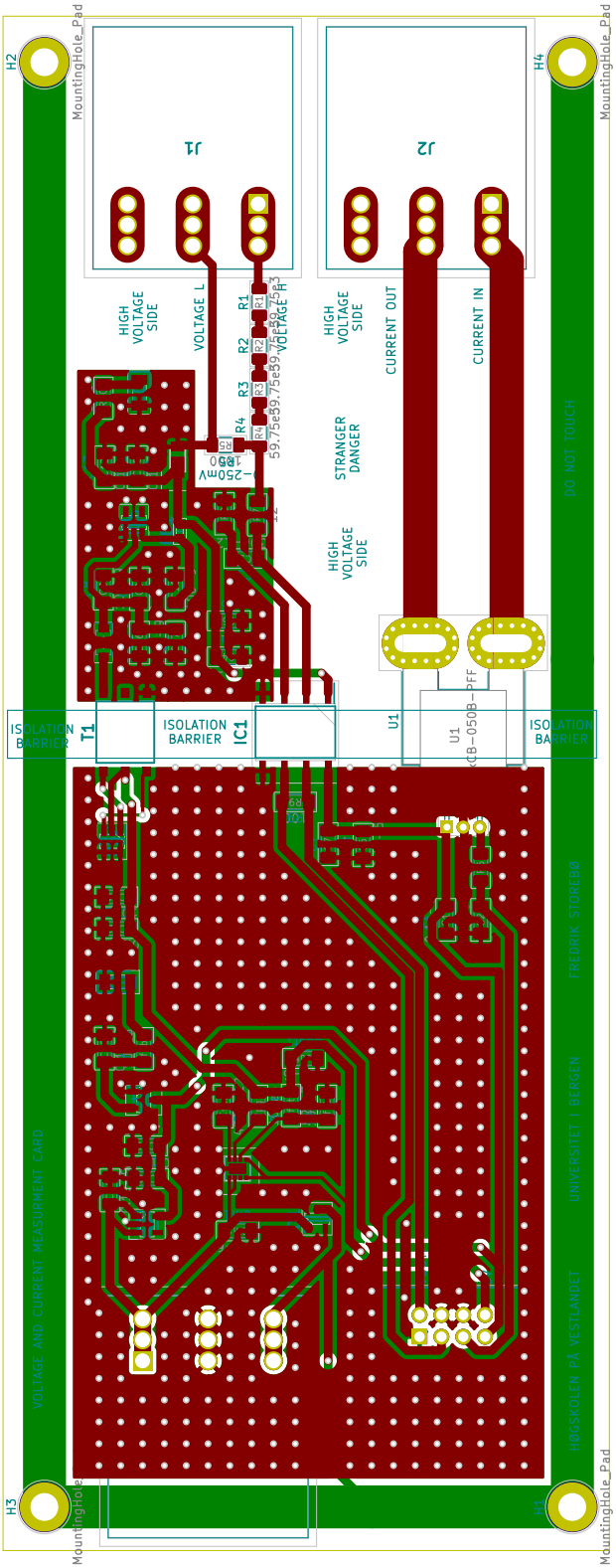

E.1.4 Copper Layout Back

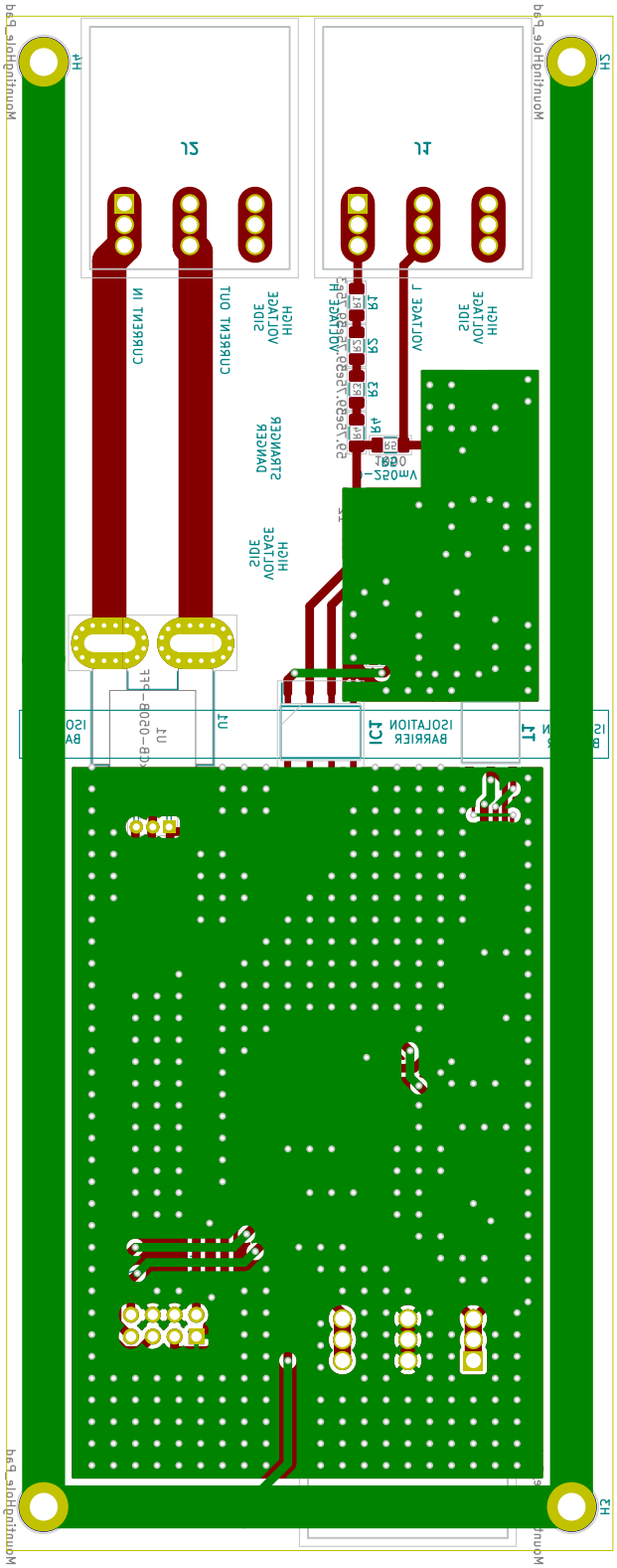

E.2 BMS Control Card

The PCB design is pulled from the open-source project on GitHub designed by Stuart Pittaway[79].

E.2.1 Electric Schematic

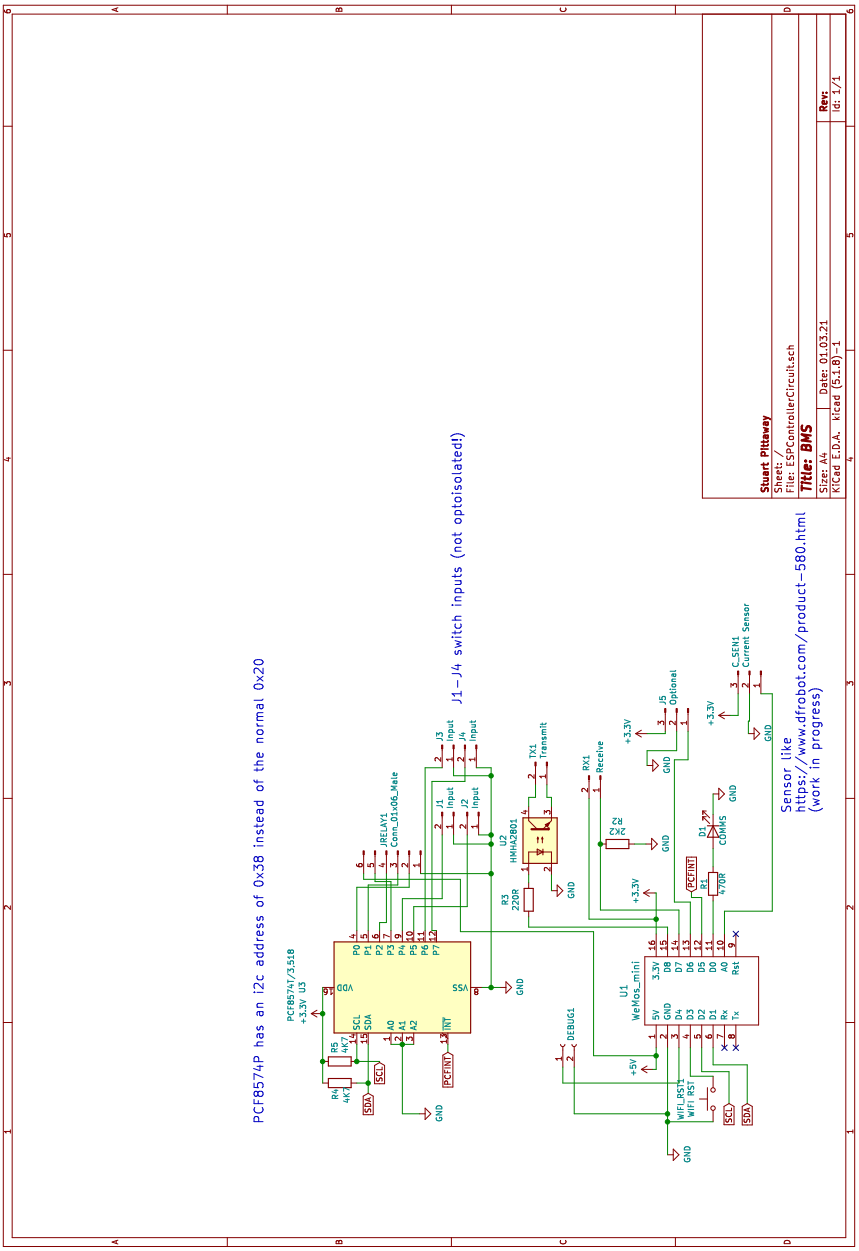

E.2.2 Copper Layout Front

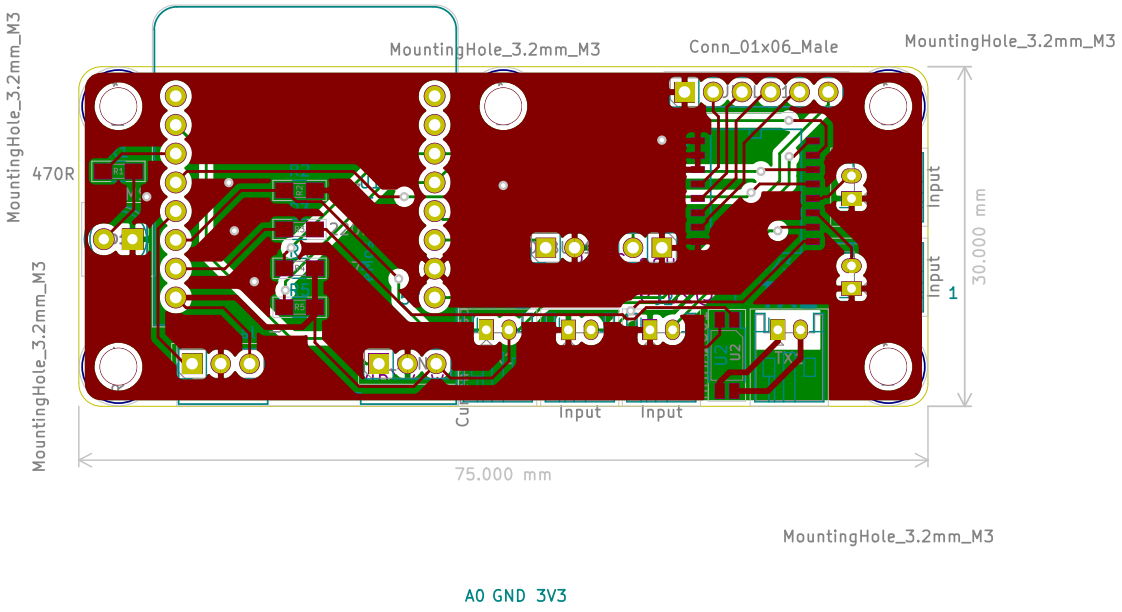

E.2.3 Copper Layout Back

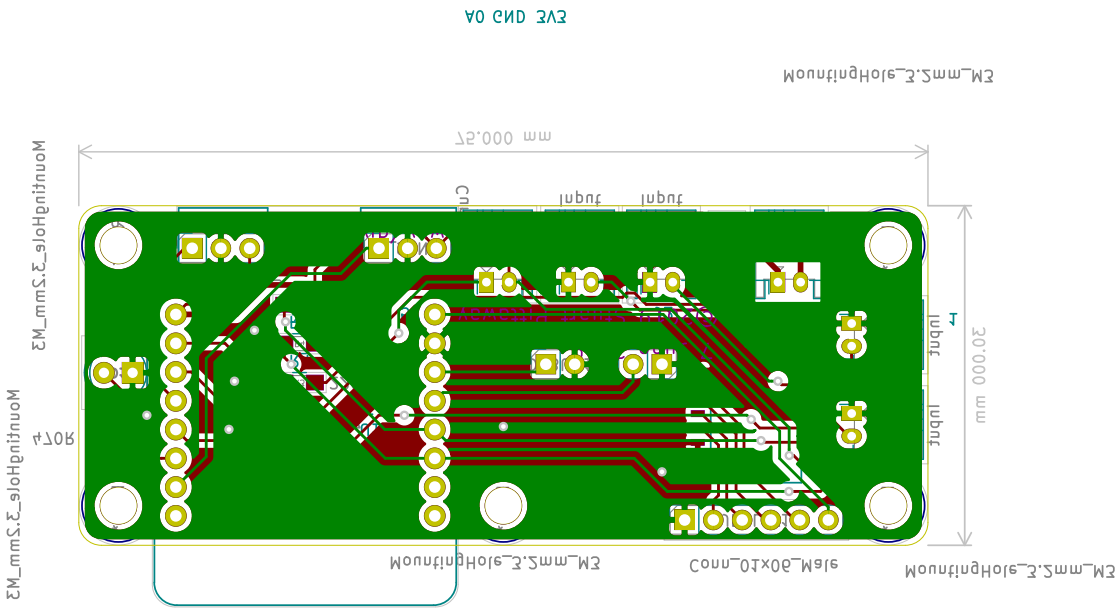

E.3 BMS Sensor Card

The PCB design is pulled from the open-source project on GitHub designed by Stuart Pittaway[79].

E.3.1 Electric Schematic

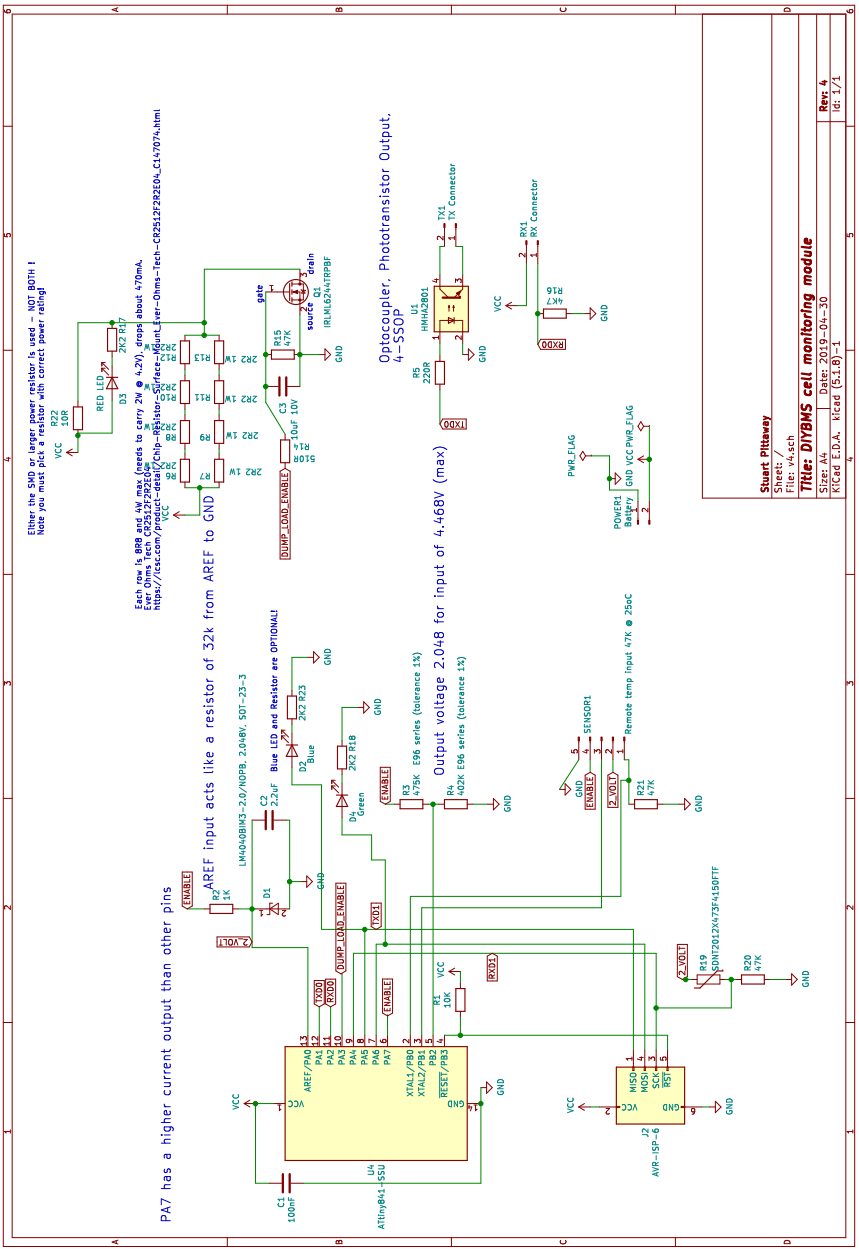

E.3.2 Copper Layout Front

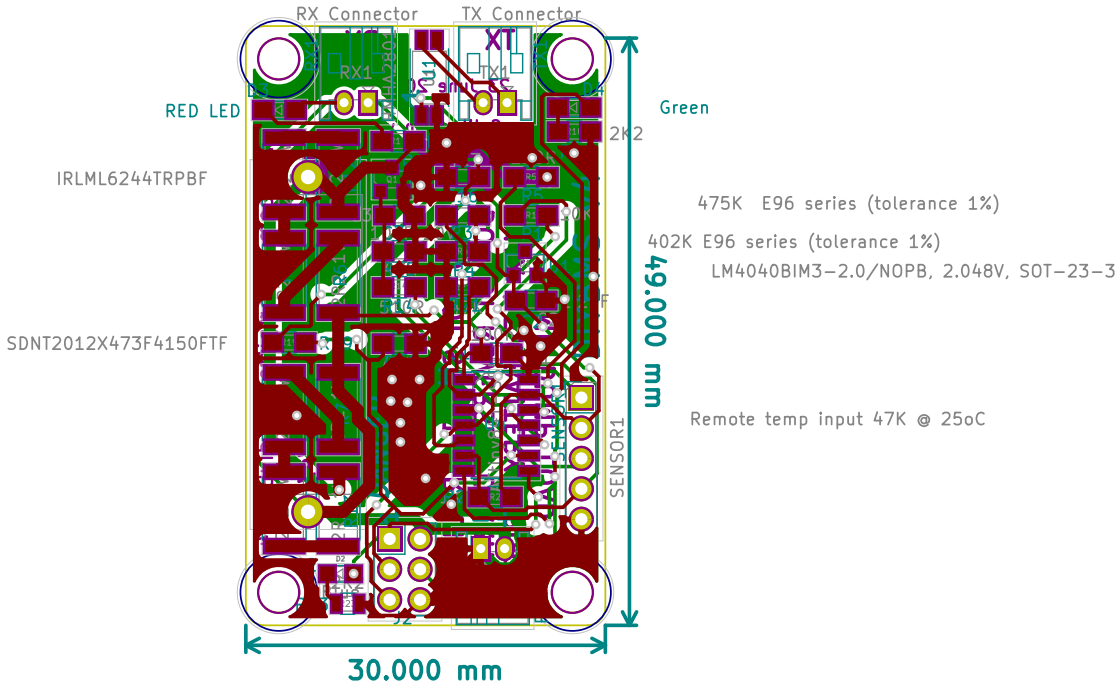

E.3.3 Copper Layout Back

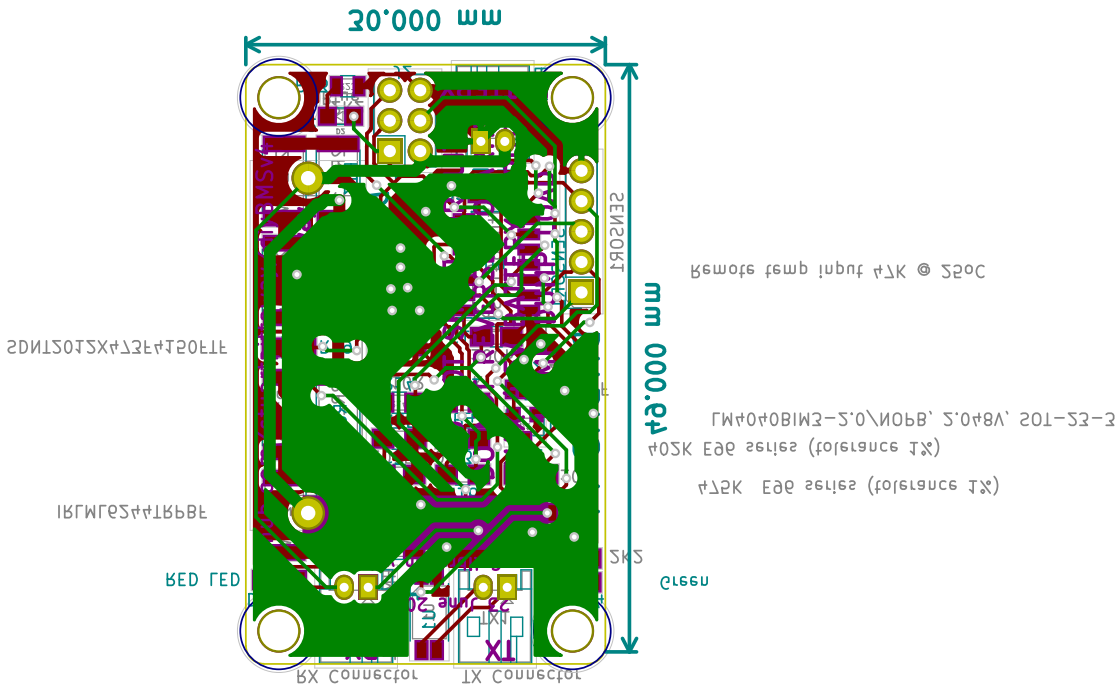

F Laboratory test equipment

Complete prototype battery system and laboratory test equipment. The connection between the components are not shown in.

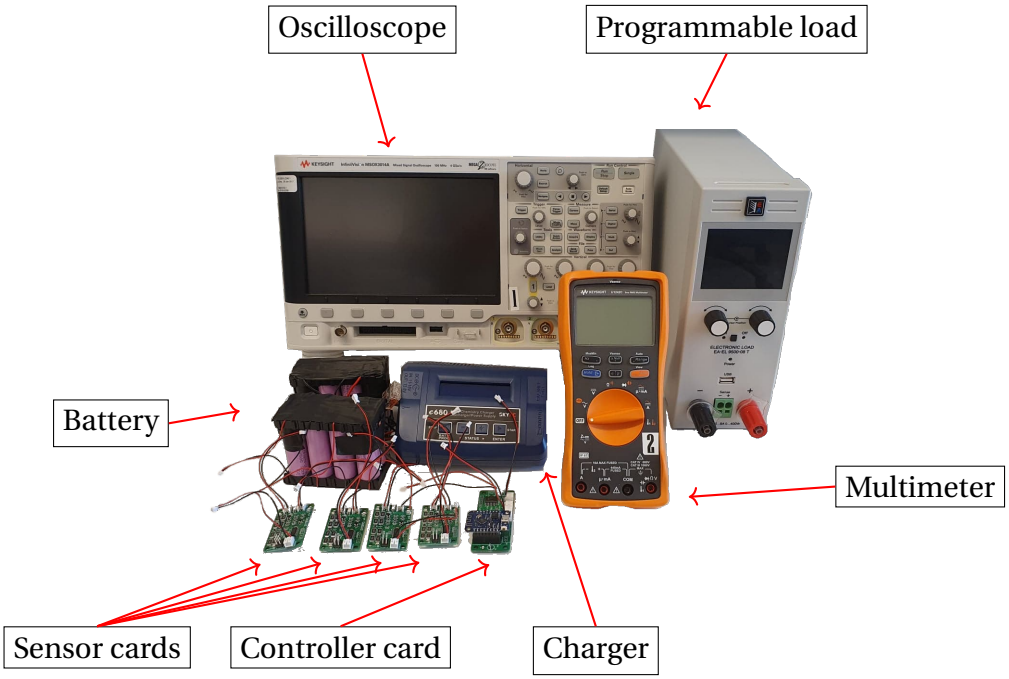

Figure F.1: Laboratory components and test setup

Index